

UNCLASSIFIED

AD NUMBER

AD819543

LIMITATION CHANGES

TO:

Approved for public release; distribution is unlimited.

FROM:

Distribution authorized to U.S. Gov't. agencies and their contractors; Critical Technology; AUG 1967. Other requests shall be referred to Air Force Aer Propulsion Laborotory, Wright-Patterson AFB, OH 45433. This document contains export-controlled technical data.

AUTHORITY

AFAPL ltr, 4 may 1973

THIS PAGE IS UNCLASSIFIED

AD81 9543

Li-Cl₂ Primary Battery Investigation

**E. H. Hietbrink, J. J. Petraitis, D. A. J. Swinkels,
and G. M. Craig**

**Research Laboratories
General Motors Corporation
Electric Powerplants Department—Indianapolis**

Technical Report AFAPL-TR-67-89

August 1967

This document is subject to special export controls
and each transmittal to foreign governments or foreign
nationals may be made only with prior approval of
the Air Force Aero Propulsion Laboratory.

**Air Force Aero Propulsion Laboratory
Directorate of Laboratories
Air Force Systems Command
Wright-Patterson Air Force Base, Ohio**

Allison

NOTICES

When Government drawings, specifications, or other data are used for any purpose other than in connection with a definitely related Government procurement operation, the United States Government thereby incurs no responsibility nor any obligation whatsoever; and the fact that the Government may have formulated, furnished, or in any way supplied the said drawings, specifications, or other data, is not to be regarded by implication or otherwise as in any manner licensing the holder or any other person or corporation, or conveying any rights or permission to manufacture, use, or sell any patented invention that may in any way be related thereto.

Copies of this report should not be returned unless return is required by security considerations, contractual obligations, or notice on a specific document.

Li-Cl₂ Primary Battery Investigation

**E. H. Hietbrink, J. J. Petraitis, D. A. J. Swinkels,
and G. M. Craig**

**This document is subject to special export controls
and each transmittal to foreign governments or foreign
nationals may be made only with prior approval of
the Air Force Aero Propulsion Laboratory.**

FOREWORD

This final report, designated as Contractor Report EI-17 (Allison EDR 5291), was prepared by the Electrochemical Laboratories, Indianapolis Department of the Research Laboratories of General Motors in fulfillment of Air Force Contract AF33(615)-5343, Project 3145, Task 314522. Air Force Aero Propulsion Laboratory technical direction was provided by Mr. W. S. Bishop, APIP-3, Wright-Patterson Air Force Base, Ohio.

Work on the basic contract began on 1 July 1966 and was completed on 30 June 1967 to perform the following:

- Define and eliminate those problems at the Cl_2 electrode which prevent the $\text{Li}-\text{Cl}_2$ battery from operating as a practical and reliable missile energy source
- Experimentally verify performance predictions for these batteries
- Determine analytically the range of operating times and power levels most applicable to primary versions of the $\text{Li}-\text{Cl}_2$ battery. The goal of the laboratory exploratory cells was to experimentally demonstrate a high power density of 20 w/cm^2 based on apparent Cl_2 electrode area for discharge rates to 20 min.

The program was directed at the Research Laboratories by E. H. Hietbrink, Supervisory Research Engineer. Dr. D. A. J. Swinkels, R. N. Seefurth, G. M. Craig, and J. J. Petraits were responsible for the technical effort. Dr. B. Agruss, Electrochemical Technology, was consultant. Management direction at the Research Laboratories included Dr. J. L. Hartman, Head of Electrochemical Laboratories, Indianapolis Department, and Dr. H. A. Wilcox, Director of Advanced Power Systems Directorate.

During the contract period, technical assistance, through periodic reviews and discussions, was obtained from the Aero Propulsion Laboratory.

This technical report was submitted on 29 June 1967 and has been reviewed and is approved.

Abstract

The higher energy and power density potentials of the Li-Cl₂ were investigated to determine its applicability to advanced weapon requirements. This program was conducted under Air Force Contract AF33(615)-5343 between 1 July 1966 and 30 June 1967.

Concentration polarization tests of the Cl₂ electrode at 1/16- and 1/8-in. thickness, pressures to 5 atm, and Cl₂ purity levels to 99.9% resulted in data that permits prediction of polarization levels over this range of variables. Current densities to 12 amp/cm² were demonstrated with polarization of 0.4 v.

Eleven high power density laboratory cells were tested at pressures to 3 atm. Power densities above 27 w/cm² were obtained for periods exceeding 30 min, demonstrating a peak power density of 43 w/cm².

The analytical work encompassed batteries operating at zero g, in a gravity environment, with waste heat either rejected via radiation (high battery case temperature) or an insulated self-contained heat sink (low battery case temperatures). Other variables included discharge time (10 to 30 min), power (5 to 30 kw), and power density (10 to 30 w/cm²). Battery energy densities to 300 w-hr/lb and 13.5 w-hr/in.³ were obtained with power densities near 20 w/cm² found to be most satisfactory. Limited work on 100-hr discharge batteries resulted in a projected energy density of 440 w-hr/lb.

The results of this program showed that the polarization at the Cl₂ electrode can be predicted and that the resulting performance is sufficient to permit the design and operation of Li-Cl₂ cells with power densities above 25 w/cm². The analytical studies also provide comparative data to illustrate the potentials of the Li-Cl₂ system and that 25 w/cm² will be adequate cell power density to attain such battery designs.

TABLE OF CONTENTS

<u>Section</u>	<u>Title</u>	<u>Page</u>
I	Introduction	1
II	Conclusions and Recommendations	3
	Conclusions	3
	Chlorine Electrode Performance	3
	Laboratory High Power Density Cell	3
	Analytical Systems Studies	4
	Recommendations	5
III	Chlorine Electrode Performance	7
	Objective	7
	Concentration Polarization	7
	Theory	7
	Test Cell	17
	Gas Analysis System	17
	Gas Control System	20
	Electrical Instrumentation	21
	Testing Procedure	26
	Results	28
	Discussion	28
	Activation Polarization	41
	Theory	41
	Test Cell	42
	Instrumentation	42
	Results	42
	Discussion	45
IV	Laboratory High Power Density Cell	51
	Objectives	51
	Basic Design Considerations	51
	Power Density Cell No. 1	52
	Description	52
	Preparation	55
	Operation and Test Results	55
	Postoperational Analysis	57

<u>Section</u>	<u>Title</u>	<u>Page</u>
	Power Density Cell No. 2	57
	Description	57
	Test Facility Rework	61
	Preparation	61
	Operation and Test Results.	61
	Postoperational Analysis	61
	Power Density Cell No. 3	61
	Description	61
	Operation and Test Results.	63
	Postoperational Analysis	65
	Power Density Cell No. 4	65
	Description	65
	Operation and Test Results.	65
	Postoperational Analysis	66
	Power Density Cell No. 5	66
	Description	66
	Operation and Test Results.	67
	Power Density Cell No. 6	67
	Description	67
	Operation and Test Results.	67
	Postoperational Analysis	71
	Power Density Cell No. 7	71
	Description	71
	Operation and Test Results.	71
	Postoperational Analysis	72
	Power Density Cell No. 8	73
	Description	73
	Operation and Test Results.	73
	Postoperational Analysis	74
	Power Density Cell No. 9	74
	Description	74
	Operation and Test Results.	74
	Power Density Cell No. 10	74
	Description	74
	Operation and Test Results.	74
	Postoperational Analysis	75
	Stray Current Cell	75
	Power Density Cell No. 11	78

<u>Section</u>	<u>Title</u>	<u>Page</u>
	Description	78
	Operation and Test Results	79
V	Analytical Systems Studies.	81
	Design A-1.	82
	Cell Design	82
	System Design	84
	Parametric Scaling of the A-1 Design	98
	Design A-2.	103
	Cell Design	104
	System Design	108
	Parametric Scaling of the A-2 Design	111
	Design B-1.	116
	Cell Design	116
	System Design	117
	Parametric Scaling of the B-1 Design	118
	Design B-2.	119
	Cell Design	124
	System Design	124
	Parametric Scaling of the B-2 Design	125
	Design C.	126
	Design of 10-hr Battery	132
	Design of 100-hr Battery.	134

LIST OF ILLUSTRATIONS

<u>Figure</u>	<u>Title</u>	<u>Page</u>
1	Electrode thickness and operating pressure effects on cell performance	4
2	Summary of Li-Cl ₂ primary battery characteristics (20-w/cm ² power density)	5
3	Calculated limiting current density as a function of pore radius	11
4	Pore size distribution for Poco-AX graphite	15
5	Pressure test cell	18
6	Gas analysis system	19
7	Typical gas chromatogram	21
8	Gas control system	22
9	Overall electrical circuit	23
10	Electrical instrumentation for concentration polarization tests	23
11	Simplified diagram of the 150-amp current controller	24
12	150-amp current controller	25
13	Typical traces obtained during the concentration polarization study . .	27
14	Concentration polarization versus current density for a 1/8-in. electrode at 1 atm	30
15	Concentration polarization versus current density for a 1/8-in. electrode at 2 atm	31
16	Concentration polarization versus current density for a 1/8-in. electrode at 5 atm	32
17	Concentration polarization versus current density for a 1/16-in. electrode at 1 atm	33
18	Concentration polarization versus current density for a 1/16-in. electrode at 2 atm	34
19	Concentration polarization versus current density for a 1/16-in. electrode at 5 atm	35
20	Concentration polarization versus current density for 1/8- and 1/16-in. electrodes using pure Cl ₂	36
21	Limiting current densities for 1/8-in. thick Poco-AX electrode	38
22	Limiting current density at an impurity level of 0.1% for Poco-AX porous graphite	39
23	Limiting current density for Poco-AX at 5 atm	40
24	Typical current and anodic polarization traces for 1.39-cm ² Poco-AX electrode at 1 atm (20 μ sec/cm)	43
25	Polarization data for Poco-AX at 1 atm	44

<u>Figure</u>	<u>Title</u>	<u>Page</u>
26	Data from Table IV plotted to evaluate a and i_0	46
27	Plot of $\log i_0$ versus $\log P$	47
28	Polarization data for Poco-AX at 1 atm.	48
29	Activation polarization versus current density for Poco-AX	49
30	Sketch of test cell No. 1	53
31	Assembled cylindrical cell	54
32	Assembled cylindrical cell shown inside the clam shell heater	54
33	Pressure can, containing cylindrical cell, attached to high pressure gas facility	55
34	High pressure test facility used with cell No. 1.	56
35	Test cell No. 1 after test	57
36	Test cell No. 2.	58
37	Detailed cutaway of test cell No. 2	58
38	Test cell No. 2.	59
39	Details of chlorine electrode.	60
40	Schematic of modified pressure test facility	62
41	Test cell No. 3.	63
42	Test cell No. 3 components	64
43	Twenty-minute discharge test results for test cell No. 3.	64
44	Effect of Cl_2 flow on cell voltage	66
45	Minimum Cl_2 flow rate versus cell current.	67
46	Power density cell No. 5.	68
47	Test cell No. 5.	69
48	High power density discharge for power density cell No. 6	69
49	Voltage-current density plot at 3 atm for cell No. 6	70
50	Voltage-current density plot at 1.5 atm for cell No. 6	70
51	Apparent resistance versus time for the first discharge of power density cell No. 7	72
52	Discharge performance curve illustrating 43 w/cm^2	73
53	Discharge of high power density cell No. 10 at 3 atm	75
54	Stray current cell cutaway.	76
55	Performance of stray current cells	77
56	Cross-section view of cell No. 11.	78
57	Sketch of A-1 cell cross section.	82
58	A-1 battery configuration	84
59	Pressure-enthalpy diagram for Cl_2 during discharge.	85
60	Sketch of heat storage unit conceptual design	86

<u>Figure</u>	<u>Title</u>	<u>Page</u>
61	Effect of mission time on Cl_2 heating rate	87
62	Reference for view factor equations	97
63	Energy density versus mission time at a 10-kw _e power level for the A-1 battery design	100
64	Volume energy density versus mission time for the 10-kw _e power level of the A-1 battery design	100
65	Energy density versus power density at a 10-kw _e power level and 30 v for the A-1 battery design	101
66	System characteristics of the A-1 battery design at 10 kw _e	101
67	Energy density versus mission time at 20-w/cm ² power density for the A-1 battery design	102
68	Battery power density versus mission time at a 20-w/cm ² power density for the A-1 battery design.	102
69	Battery power density versus mission time at a 10-kw _e power level for the A-1 battery design.	103
70	Effect of battery voltage on 10-kw _e A-1 battery energy density	104
71	Model of LiH melting system	105
72	Heat sink design for the A-2 battery system	107
73	Li-Cl ₂ cell concept for the A-2 battery design	108
74	Design for A-2 battery system	109
75	Sketch of the alternate heat sink design for the A-2 battery design. . .	111
76	Weight-energy density versus mission time at a 10-kw _e power level for the A-2 battery design.	112
77	Volume energy density versus mission time at a 10-kw _e power level for the A-2 battery design.	113
78	Weight energy density versus power density at a 10-kw _e power level for the A-2 battery design.	113
79	Weight energy density versus power density at a 10-kw _e power level for the A-2 battery design.	113
80	Volume energy density versus power density at a 10-kw _e power level for the A-2 battery design.	114
81	System characteristics of A-2 battery design at 10-kw _e power level. .	114
82	System characteristics of A-2 battery design at 10-kw _e power level. .	114
83	System characteristics of A-2 battery design at 20 w/cm ² power density.	115
84	System characteristics of A-2 battery design at 20 w/cm ² power density.	115

<u>Figure</u>	<u>Title</u>	<u>Page</u>
85	Effect of case temperature on energy density at 10-kw power level	116
86	Sketch of the B-1 cell cross section.	117
87	Sketch of the B-1 battery design.	118
88	Weight energy density versus power density for the 10-kw _e B-1 battery design	120
89	Weight energy density versus discharge time for the 10-kw _e B-1 battery design	120
90	Volume energy density versus power density for the 10-kw _e B-1 battery design.	121
91	Volume energy density versus discharge time for the 10-kw _e B-1 battery design.	121
92	Volume energy density versus weight energy density for the 10-kw _e B-1 battery design	122
93	Effect of power level on the B-1 weight energy density.	122
94	Effect of power level on the B-1 volume energy density	123
95	B-1 battery power density versus discharge time	123
96	Battery power density versus energy storage for the B-1 battery design	124
97	Sketch of the B-2 battery design.	125
98	Weight energy density versus power density for the 10-kw _e B-1 battery design	126
99	Volume energy density versus power density for the 10-kw _e B-2 battery design	127
100	Weight energy density versus power density for the 10-kw _e B-2 battery design (temperature effects).	127
101	Weight energy density versus discharge time for the 10-kw _e B-2 battery design (temperature effects).	128
102	Volume energy density versus power density for the 10-kw _e B-2 battery design (temperature effects).	128
103	Volume energy density versus discharge time for the 10-kw _e B-2 battery design (temperature effects).	129
104	Volume energy density versus weight energy density for the 10-kw _e B-2 battery design.	129
105	Volume energy density versus weight energy density for the 10-kw _e B-2 battery design.	130
106	Power level effect on the B-2 energy densities	130
107	Battery power density for the B-1 battery design.	131

<u>Figure</u>	<u>Title</u>	<u>Page</u>
108	Battery power density versus skin temperature for the B-2 battery design	131
109	Section view of cell for 10-hr battery	132
110	Section view of 10-hr Li-Cl ₂ primary battery.	133
111	Energy density of 1-kw Li-Cl ₂ 10-hr battery	133
112	Sketch of the 100-hr Li-Cl ₂ battery system.	135
113	Cell details for the 100-hr battery design.	136
114	Energy density of 1-kw Li-Cl ₂ 100-hr battery	136

LIST OF TABLES

<u>Table</u>	<u>Title</u>	<u>Page</u>
I	Porosity—pore size steps used in computer calculations.	16
II	Electrode performance data in amp/cm ²	29
III	Comparison between calculated and experimental limiting current densities (i _L)	37
IV	Average anodic polarization data (2 Cl ⁻ → Cl ₂ + 2 e ⁻) for 1.39 cm ² electrodes	45
V	Li-Cl ₂ primary battery systems	81
VI	B-1 battery design performance values	119

SECTION I**INTRODUCTION**

As the state of the art advances in weaponry, there is an increasing need for more compact power sources which provide high power and energy capabilities. Since the projected characteristics of current electrochemical systems for short discharge times (< 30 min) are generally in the order of 75 w-hr/lb, the Li-Cl₂ couple has been under investigation because of its potential to provide at least a twofold increase in energy density for such applications. Essential to these improved energy densities is the higher current densities that appear possible with this couple.

The specific system being considered consists of a Li anode and a Cl₂ cathode, utilizing the reaction product LiCl as the electrolyte. The electrochemistry of the system is well known, electrode reactions are simple and extremely rapid with little or no polarization, a high voltage is produced, and the conductivity of the fused salt electrolyte is at least an order of magnitude greater than aqueous systems. These characteristics give promise of yielding a compact power system with both high power density and high energy density capability.

The biggest obstacle to obtaining high power density from the cells is the polarization caused by electroinactive impurities in the Cl₂. Therefore, one of the major tasks in the contractual program was the laboratory investigation of the polarization due to such impurities as a function of electrode thickness, operating pressure, and impurity levels in the Cl₂.

A second task was the incorporation of improved electrode designs in the operation of high power density laboratory Li-Cl₂ cells. The contractual goal was to demonstrate a power density of 20 w/cm² for a period of 20 min.

The last task of the contract to examine the feasibility of the Li-Cl₂ primary battery was an analytical systems study to outline Li-Cl₂ battery systems that were designed for a range of operational and design parameters. The majority of effort was on batteries for short discharge times (<30 min), although the characteristics of batteries with up to 100-hr discharge times were to be reviewed. The results of this investigation are presented herein.

SECTION II

CONCLUSIONS AND RECOMMENDATIONS

CONCLUSIONS

Chlorine Electrode Performance

A successful model has been developed for the mass transport processes at the Cl_2 electrode. This model allows for the calculation of the maximum current density which can be obtained from Poco-AX porous graphite electrodes as a function of electrode thickness, Cl_2 purity, and total pressure. Experimental results were obtained for 1/16- and 1/8-in. thick electrodes for Cl_2 purity levels to 99.9% and pressures up to 5 atm. Data obtained on 1/8-in. electrodes resulted in current densities of approximately 12 amp/cm^2 . The exchange current density for the electron transfer process was also determined at 1, 2 and 5 atm pressure.

Laboratory High Power Density Cell

Electrodes were fabricated and tested that produced power densities in excess of the 20 w/cm^2 goal of the contract. Power densities to 43 w/cm^2 were demonstrated at cell operating pressures of 3 atm. Cl_2 excess flows required to control impurity buildup in the cathode were 3 to 5% of the required flow.

Typical comparative performance of laboratory cells is shown in Figure 1, illustrating the effects of pressure level and cathode thickness in laboratory cells that operated above the required 20 w/cm^2 . These results, showing improved performance from thicker electrodes, are contrary to that expected based on the theories of Cl_2 diffusion and the effects of impurities in Cl_2 . However, this performance can possibly be explained on the basis of cathode pressure differential effects on the graphite/LiCl interface.

Since the wetting quality of LiCl on porous graphite is poor, increases in the ΔP across the electrode will tend to draw the LiCl in closer contact with the graphite thus reducing cell resistance. Such increases in ΔP would be present in thicker electrodes at the same pressure and current density or at the lower pressure for the same electrode operating at a constant current density, explaining the characteristics of the curves in Figure 1. A better understanding of this phenomenon is required to permit the design of cells with more predictable performance characteristics.

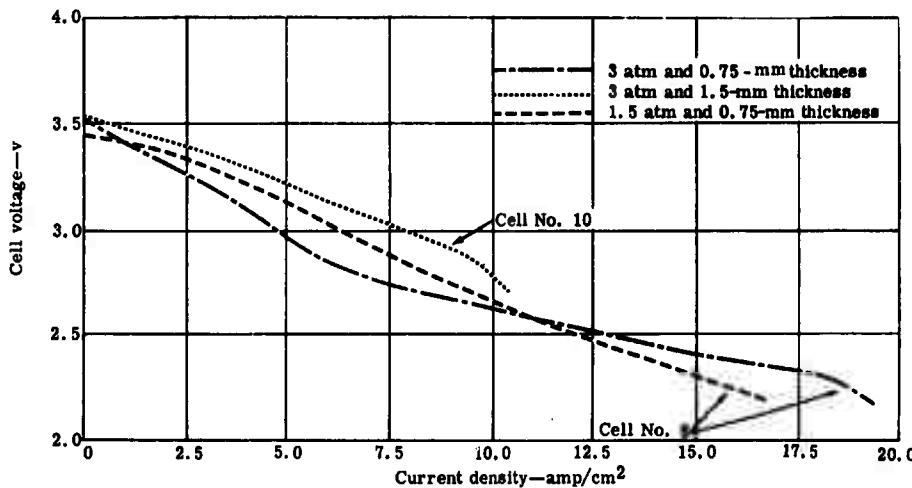


Figure 1. Electrode thickness and operating pressure effects on cell performance.

Analytical Systems Studies

The results of this systems study have indicated the effects of various design and operational parameters on the characteristics of four short duration and two extended discharge Li-Cl₂ primary battery concepts. The following points can be summarized from this analytical work.

- Weight energy densities up to 300 w-hr/lb appear feasible for 10 kw_e designs operating in a cavity field and rejecting waste heat via radiation with 30-min discharge times. Corresponding volume densities are 13.5 w-hr/in.³.
- Rejecting waste heat to a contained heat sink reduces weight and volume energy densities by approximately 55%.
- The effect of zero g design requirements is to reduce weight density by 35 to 40% and volume density by 35%.
- Battery case temperature has less effect on the volume of the heat sink batteries (<25%); however, an increase in battery skin temperature from 300 to 600°F increases the weight energy density to 55%.

- Cell power densities of 10 to 25 w/cm² are required to obtain optimum battery performance over the range of design conditions evaluated.
- Extended discharge times up to 100 hr results in system energy densities of 440 w-hr/lb.

The characteristics of the various designs are summarized in the plot shown in Figure 2, indicating the potential of Li-Cl₂ batteries for the operating conditions noted.

RECOMMENDATIONS

As a result of the work completed during this contract period, it is recommended that work on the Li-Cl₂ battery be continued in the areas discussed in the following paragraphs.

The understanding of the electrode processes in the Li-Cl₂ cell has reached a point where very high power densities can be routinely achieved. Coupled with these high power densities are unavoidable temperature rises due to resistance and polarization losses. These temperature rises will no doubt affect the self-discharge processes. It is, therefore, recommended that an investigation of the self-discharge processes as a function of temperature be undertaken as one of the next logical steps towards the practical realization of a Li-Cl₂ battery.

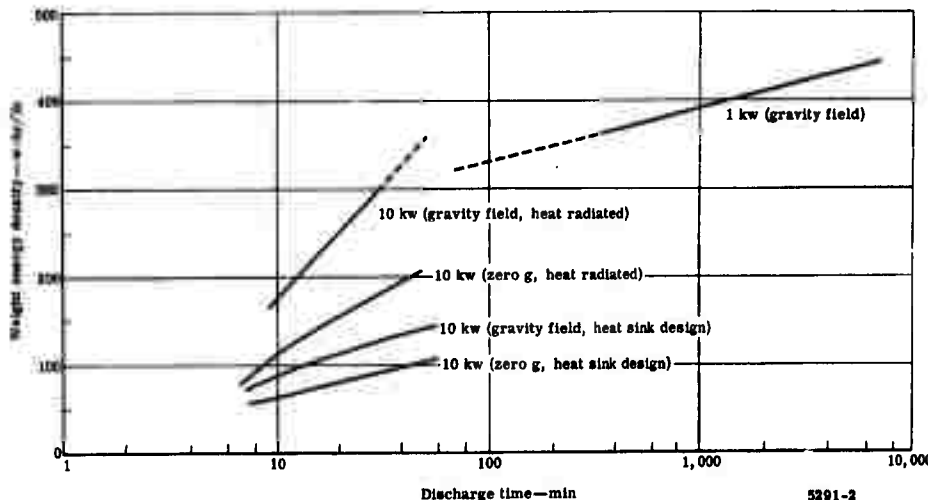


Figure 2. Summary of Li-Cl₂ primary battery characteristics
(20-w/cm² power density).

The present program demonstrated the feasibility of high power density in laboratory type cells. It is recommended that cell testing be continued with the objectives of demonstrating cell hardware more amenable to flightweight systems and the further exploration of design phenomena such as exhibited in Figure 1 and described earlier.

The analytical studies have shown the potential of Li-Cl₂ batteries over a range of design and operating conditions. It is recommended that such studies be extended to the following:

- To very short missions (i.e., as 1 to 10 min), since the steeper slope of the curves in Figure 2 indicate an eventual cross over of Li-Cl₂ systems with existing battery performance
- To long duration zero g type missions
- To conduct a more detailed design investigation of a Li-Cl₂ battery to meet an application with definite specifications to allow a comparison of alternate batteries for that application

SECTION III

CHLORINE ELECTRODE PERFORMANCE

OBJECTIVE

The Cl_2 electrode is electrochemically the most complex part of the $\text{Li}-\text{Cl}_2$ cell. The objective of this task was to obtain a better understanding of the Cl_2 electrode performance affected by the three main variables—electrode thickness, Cl_2 pressure, and Cl_2 purity. The first process studied was the mass transport of Cl_2 from the bulk gas to the electrode-electrolyte interface. The concentration polarization associated with this process was determined under various conditions. Secondly, the activation polarization associated with the electrochemical reaction $\text{Cl}_2 + 2 \text{e}^- \rightleftharpoons 2 \text{Cl}^-$ was determined under different conditions and was interpreted.

CONCENTRATION POLARIZATION

Theory

The electrochemical reaction of Li and Cl_2 has been well characterized. At the Li electrode,



and at the Cl_2 electrode



The overall reaction is



The energy capacity, based on the pure reactants, is 990 w-hr/lb. This system has the desired high open circuit voltage and energy capacity.

The Li electrode reactions are extremely rapid in fused salt electrolytes, and laboratory tests have shown negligible polarization at high current densities. Crude laboratory cells proved that the $\text{Li}-\text{Cl}_2$ system could operate at high current densities to 3 to 5 amp/cm².

Separate fundamental studies on the Li electrode showed that there was no polarization to 40 amp/cm² either on charge or discharge. The voltage-current density curve for the Li electrode was a straight line passing through the open circuit voltage from 40 amp/cm² charge to 40 amp/cm² discharge. Theoretically, there should be some point where polarization would put some curvature in the continued straight line. However, it was found that the Cl₂ electrode would limit the current density of the cell before reaching 40 amp/cm². Further studies on the Li electrode were not performed.

In a practical cell, a physically stable interface between the Li electrode and the electrolyte must be maintained. A wick electrode has been developed to stabilize this interface.*

A theoretical model has been developed describing the reaction kinetics at the porous graphite Cl₂ cathode.** Because the fused LiCl electrolyte does not wet carbon or graphite, it is postulated that the reaction takes place in the bulk interface region between the porous electrode and the electrolyte and not deep within the pores as is the case in most aqueous porous electrodes.

The overall process at the Cl₂ electrode can be divided into the following five steps:

1. Flow and diffusion of Cl₂ gas through the porous plug
2. Dissolution of Cl₂ at the gas-liquid interface
3. Diffusion of dissolved Cl₂ to the carbon-LiCl interface
4. Dissociation and charge transfer
5. Migration of Cl⁻ into the bulk electrolyte

Steps 2 and 5 are fast mass transport steps which have negligible effect on the polarization. Step 4 occurs at the actual electrode-electrolyte interface and gives rise to the activation polarization. Steps 1 and 3 give rise to the concentration polarization with the relative contribution of these two steps being determined mainly by the pore radius.

The maximum current density (i_L) which a nonwetted electrode can support is given by Equation (4).

$$i_L(r) = \frac{A n F D K P_2 \phi(r)}{r} \quad (4)$$

*Swinkels, D. A. J. and Tricklebank, S. B. "Lithium Wick Electrode." Electrochemical Technology (In press).

**Swinkels, D. A. J. "Lithium-Chlorine Battery." Journal of the Electrochemical Society. Vol 113 (1966) p 6.

where

A = constant ≈ 8
n = number of electrons, 2
F = Faraday, 96493 coul/mole
D = diffusion coefficient of Cl_2
(in LiCl at 650°C—D $\approx 4 \times 10^{-5} \text{ cm}^2 \text{ sec}^{-1}$)
K = Henry's law constant,
 $10^{-6} \text{ moles-cm}^{-3}\text{-atm}^{-1}$ at 650°C
 P_2 = Cl_2 pressure at the gas-liquid interface
 $\phi(r)$ = volume of pores of radius r/cm^3 of electrode
 r = pore radius, cm

$i_L(r)$ is the current density (amp/cm^2) due to the pores of radius r . The total current density for an electrode with a range of different pore sizes is then given by

$$i_L(\text{total}) = \sum_r i_L(r) \quad (5)$$

The partial pressure of Cl_2 at the gas-liquid interface (P_2) is equal to the total pressure (P_T) in the gas-stream feeding the electrode minus the pressure drop (ΔP) across the electrode and minus the partial pressure of impurities $P_s(i)$ in the gas at the gas-liquid interface, i.e.,

$$P_2 = P_T - \Delta P - P_s(i) \quad (6)$$

The pressure drop ΔP is determined by the flow resistance in the pores to the Poisseuille flow (viscous) and the Knudsen flow (molecular streaming).

For a single pore size, r

$$\Delta P(r) = \frac{i_L RT}{nF\phi} \left(\frac{L}{K} \right) \quad (7)$$

where

$$K = \frac{1.013 r^2 (2 P_T - \Delta P)}{16\mu} + \frac{4\pi r}{3} \sqrt{\frac{1.6634 T}{\pi M}} \quad (8)$$

R = gas constant = $82.082 \text{ cm}^3\text{-atm-deg}^{-1}\text{-mole}^{-1}$

T = temperature, °K

L = pore length, t r

t = electrode thickness in the direction of flow
 τ = tortuosity of the pores, ≈ 4
 ϕ = total porosity
 μ = gas viscosity
 δ = constant, 0.9
 M = molecular weight of Cl_2 , 70.9

The tortuosity of the pores is about 3.75 for Poco-AX porous graphite when determined by gas flow measurements through porous plugs of Poco-AX. This is a surprisingly high tortuosity for a material of such high porosity (57% porous). The high tortuosity is no doubt a result of the manufacturing methods used in making this material. It should also be noted that the tortuosity found by a flow measurement heavily favors the tortuosity of the larger pores so that the tortuosity of small pores may be quite different. However, a tortuosity of 3.75 will be used in all calculations.

The viscosity of Cl_2 gas (μ) is given in centipoise by*

$$\mu = 1.4329 \times 10^{-4} + 4.6979 \times 10^{-5} T - 3.7158 \times 10^{-9} T^2 - 4.0541 \times 10^{-12} T^3 \quad (9)$$

In the absence of any impurities, $P_s(i)$ of Equation (6), will be zero, and the limiting current density, therefore, can be found for pure Cl_2 by combining Equations (4), (8), and (9). This results in a i_L —pore radius relationship as shown in Figure 3.

For a piece of carbon with a variety of parallel flow paths of different radii, the equation is

$$\frac{1}{\Delta P} = \sum_r \frac{1}{\Delta P(r)} \quad (10)$$

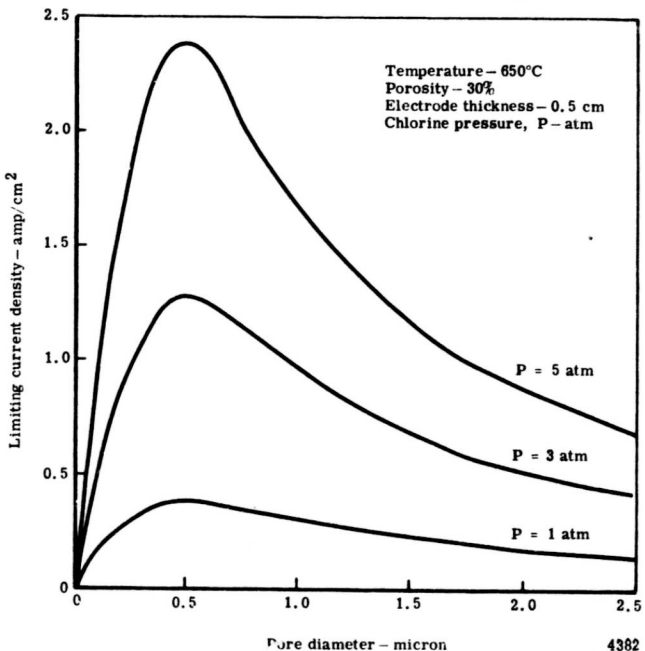
or

$$\Delta P = \frac{1}{\sum_r \frac{1}{\Delta P(r)}} \quad (11)$$

The partial pressure of impurities $P_s(i)$ at the gas-liquid interface are considered in the following paragraphs.

*Thermophysical Properties Research Center Data Book, Vol 2. Purdue University, Lafayette, Indiana. Table 2030.

Figure 3. Calculated limiting current density as a function of pore radius.



The presence of electro-inactive impurities in the gas feed to a porous gas electrode can result in the rapid buildup of considerable polarization due to the accumulation of the inactive impurities in the pores. This is particularly true for high current density systems such as the Cl₂ electrode in fused alkali halides. Commercial grades of Cl₂ typically contain 0.5% inert impurities such as N₂ and CO₂. When the rate at which Cl₂ is supplied to the electrode is exactly sufficient to maintain the electrode reaction (i.e., the electrode is dead ended), these inert impurities rapidly accumulate at the electrode-electrolyte interface. The impurities can leave the interface by dissolution in the electrolyte and diffusion into the bulk or by back diffusion against the flowing Cl₂ stream. The first of these is negligible because of the low solubility and low diffusion coefficients involved. If it is assumed that the impurity has the same solubility and diffusion coefficient as Cl₂, * then the maximum flux of impurity through the electrolyte (j) is

$$j = - D \frac{\Delta C}{\Delta x} \quad (12)$$

*Swinkels, D. A. J. "Lithium-Chlorine Battery." Journal of the Electrochemical Society. Vol 113, No. 1 (January 1966), pp 6-10.

$$= -4 \times 10^{-5} \times \frac{-10^{-6}}{1} N_i = 4 \times 10^{-11} N_i \quad (13)$$

where N_i = mole fraction of impurities at the interface.

At a current density of 3 amp/cm², the flux of Cl₂ is $i/2F \approx 1.5 \times 10^{-5}$ mole/sec. Hence, the maximum concentration of impurities in the Cl₂ feed which can be removed by this process is $4 \times 10^{-11} N_i / 1.5 \times 10^{-5} = 2.67 \times 10^{-6} N_i$. Since N_i must be less than unity, the impurity level must be less than 2.67 ppm. However, as current is drawn from a Li-Cl₂ cell, more electrolyte is generated at the electrodes which can dissolve $10^{-6} N_i P_T$ moles of impurity/cm³ of electrolyte where P_T is the total pressure. Since the transport number of Li⁺ in LiCl is 0.75,* then 0.75 of the new electrolyte is generated at the Cl₂ electrode. One mole of Cl₂ will then produce 1.5 moles of LiCl at the Cl₂ electrode which can dissolve $43 \times 10^{-6} N_i P_T$ moles of impurity. For typical values of $P_T = 5$ atm and $N_i = 0.05$, an impurity level of ≈ 11 ppm can be tolerated. Much larger quantities of impurities can be removed from the electrode by flowing excess Cl₂ either through or behind the porous electrode. A study of the latter type of electrode (a "flow-by" electrode) is reported herein.

Back diffusion of impurities in the pores against the flowing Cl₂ gas can be treated as a linear diffusion problem and is

$$\frac{\partial C}{\partial t} = D \frac{\partial^2 C}{\partial x^2} - \frac{\partial (Cv)}{\partial x} \quad (14)$$

where

C = concentration of impurity gas

v = velocity of gas flow

x = linear dimension in the direction of net flow

The transient problem described by Equation (14) has recently been treated.** Since under most conditions steady state is reached in a few seconds, all experiments were done under steady-state conditions, i.e.,

$$\frac{\partial C}{\partial t} = 0$$

*Duke, F. R. and Bowman, A. L. Journal of the Electrochemical Society, Vol 106, p 622 (1959).

**Niggemann, R. E. Effect of Oxidizer Electroinactive Impurities on the Design of Primary Battery Systems, Allison Division, General Motors Advanced Power Systems. Report No. TN 9898-83. 3 March 1966.

Equation (14) after integrating once with respect to x becomes

$$D \frac{dC}{dx} = -Cv = j_1 \quad (15)$$

where j_1 is the net flux of impurity through the pore under steady-state conditions.

It is now assumed that the impurity does not react or dissolve at the gas-liquid interface where $j_1 = 0$.

Therefore,

$$D \frac{dC}{dx} - Cv = 0 \quad (16)$$

The solution of Equation (16) is

$$\ln C(x) = \frac{vx}{D} + \text{constant} \quad (17)$$

if at $x = 0$ the impurity content is kept at a constant value (C_0) by flowing gas past the electrode, Equation (17) becomes

$$C(x) = C_0 \exp \frac{vx}{D} \quad (18)$$

The total length (L) of the diffusion path is equal to the thickness (t) of the porous electrode times the tortuosity (τ) of the pores within the porous material.

The impurity concentration at the gas-liquid interface is

$$\begin{aligned} C_s &= C_0 \exp \frac{vL}{D} \\ &= C_0 \exp \frac{v\tau t}{D} \end{aligned} \quad (19)$$

The velocity of gas flow within the pores in the x direction is

$$v = \frac{iRT}{nFP_T \phi} \quad (20)$$

where

where

i = current density per geometrical cm^2

ϕ = porosity

P_T = total pressure

Therefore,

$$C_s(i) = C_0 \exp \left(\frac{iRT\tau t}{nFP_T \phi D} \right) \quad (21)$$

or in terms of the impurity pressure

$$P_s(i) = P_0 \exp \left(\frac{iRT\tau t}{nFP_T \phi D} \right) \quad (22)$$

where

P_0 = impurity pressure in the incoming gas, $N_0 P_T$

$P_s(i)$ = impurity pressure in the gas at the gas-liquid interface at current density
 i , amp/cm^2

N_0 = impurity mole fraction in the feed gas

When the limiting current density (i_L) is drawn,

$$P_s(i_L) = N_0 P_T \exp \left(\frac{i_L RT\tau t}{nFP_T \phi D} \right) \quad (23)$$

It is clear that P_2 of Equation (4) is a complex function of i_L and no explicit equation, therefore, can be written for i_L . A computer program was written to calculate i_L by an iteration process. The results of these calculations will be compared with the experimental data in the discussion section. Inputs to the program consisted of the porosity and pore size distribution of the Poco-AX material and the various constants used in Equations (4) to (23). The porosity and pore size distribution were determined by mercury intrusion and BET adsorption methods. The results are shown in Figure 4.

The pore size distribution was approximated by an 11 step staircase function also shown in Figure 4. It was assumed that the effective surface roughness factor of the porous graphite was about five so that five times as many pore mouths see the electrolyte than is calculated from the porosity. This effective roughness is due to the fact that when current is drawn the pressure in the pores is reduced and the electrolyte is drawn some distance into the larger pores, contacting more small pores. This effective roughness is, therefore, really a variable quantity which should increase with increasing ΔP . However, this

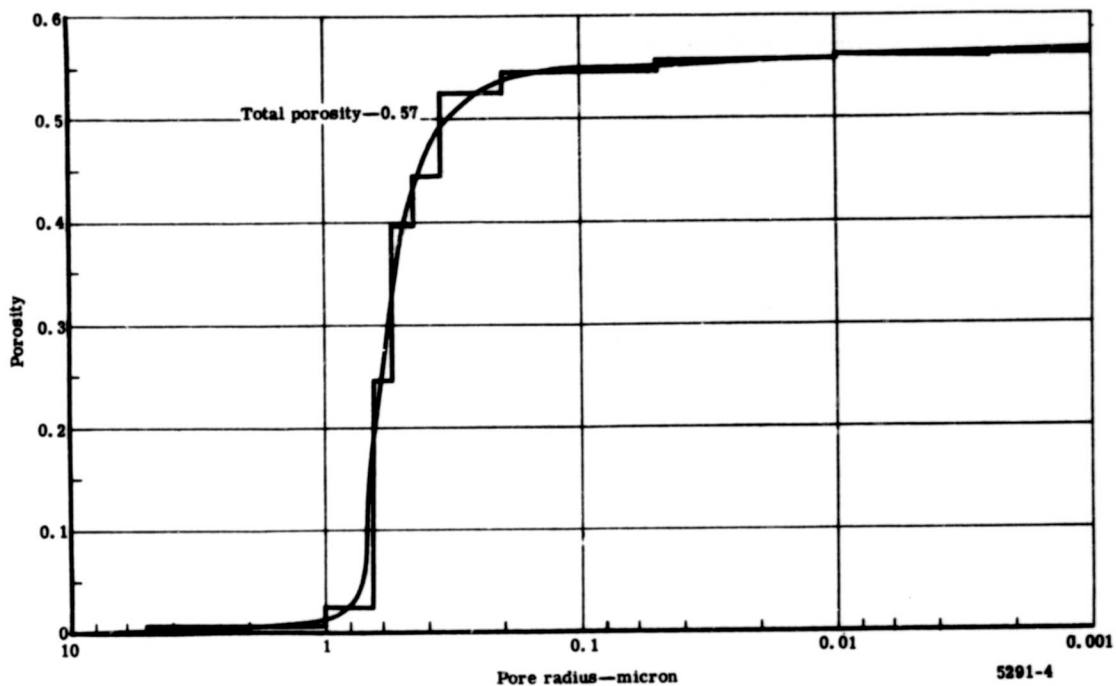


Figure 4. Pore size distribution for Poco-AX graphite.

added complexity of a variable roughness factor was not used. Table I shows the steps used in the computer program. Steps 9-11 have been multiplied by five to allow for the roughness factor and step 8 has been multiplied by two.

The diffusion coefficient D for a binary gas mixture may be calculated from*

$$D = \frac{0.00185 T^{3/2} \left[\frac{M_1 + M_2}{M_1 M_2} \right]^{1/2}}{P \sigma_{12}^2 \Omega_D} \quad (24)$$

*Reid, R. C. and Sherwood, T. K. The Properties of Gases and Liquids. New York: McGraw-Hill, 1958, pp. 268-9.

Table I.
Porosity—pore size steps used in computer calculations.

<u>Pore radius (microns)</u>	<u>Porosity</u>
5.0	0.005
1.0	0.02
0.65	0.22
0.55	0.15
0.45	0.05
0.35	0.08
0.20	0.02
0.05	0.02*
0.01	0.015**
0.0025	0.015**
0.001	0.015**

*Actual porosity \times 2 to allow for effective roughness factor.

**Actual porosity \times 5 to allow for effective roughness factor.

where

T = temperature, °K

M_1, M_2 = molecular weights of the two gases

σ_{12} = $1/2 (\sigma_1 + \sigma_2)$

σ_1, σ_2 = collision diameters

Ω_D = collision integral available from tables

For Ar and Cl_2 , $M_1 = 39.95$, $M_2 = 70.91$, $\sigma_1 = 3.418\text{A}$, $\sigma_2 = 4.115\text{A}$, $\Omega_D = 0.8652$, and $D = 0.84/P$, where P = total pressure in atmospheres. This value of D for the diffusion of impurities in the gas phase was entered in Equation (23) and used in the computer calculations of the limiting current density for the Poco-AX graphite.

*Reid, R. C., and Sherwood, T. K. The Properties of Gases and Liquids. New York; McGraw-Hill, 1958, p 268-9.

Test Cell

A schematic diagram of the working parts of the cell used for these studies is shown in Figure 5. LiCl electrolyte is contained in a Graphitite crucible with a porous graphite bottom (Poco Carbon Company Grade AX). This porous graphite, to which Cl₂ or varying mixtures of Cl₂ and Ar can be fed, is the working electrode. A Graphitite flow-by adapter below the porous graphite disk ensures uniform gas flow past the entire inner electrode surface; a quartz tube on top of the electrode exactly defines the electrode area. The reference and counter electrodes are mounted concentrically. The reference electrode is electrically isolated by means of a quartz tube and is slipped inside a hollow counter electrode which is grooved to permit maximum surface area and slotted to prevent pressure differences between the inside and outside of the electrode. The entire assembly is placed inside a Vycor tube and heated by means of clamshell heaters outside the Vycor container for most of the 1-atm tests.

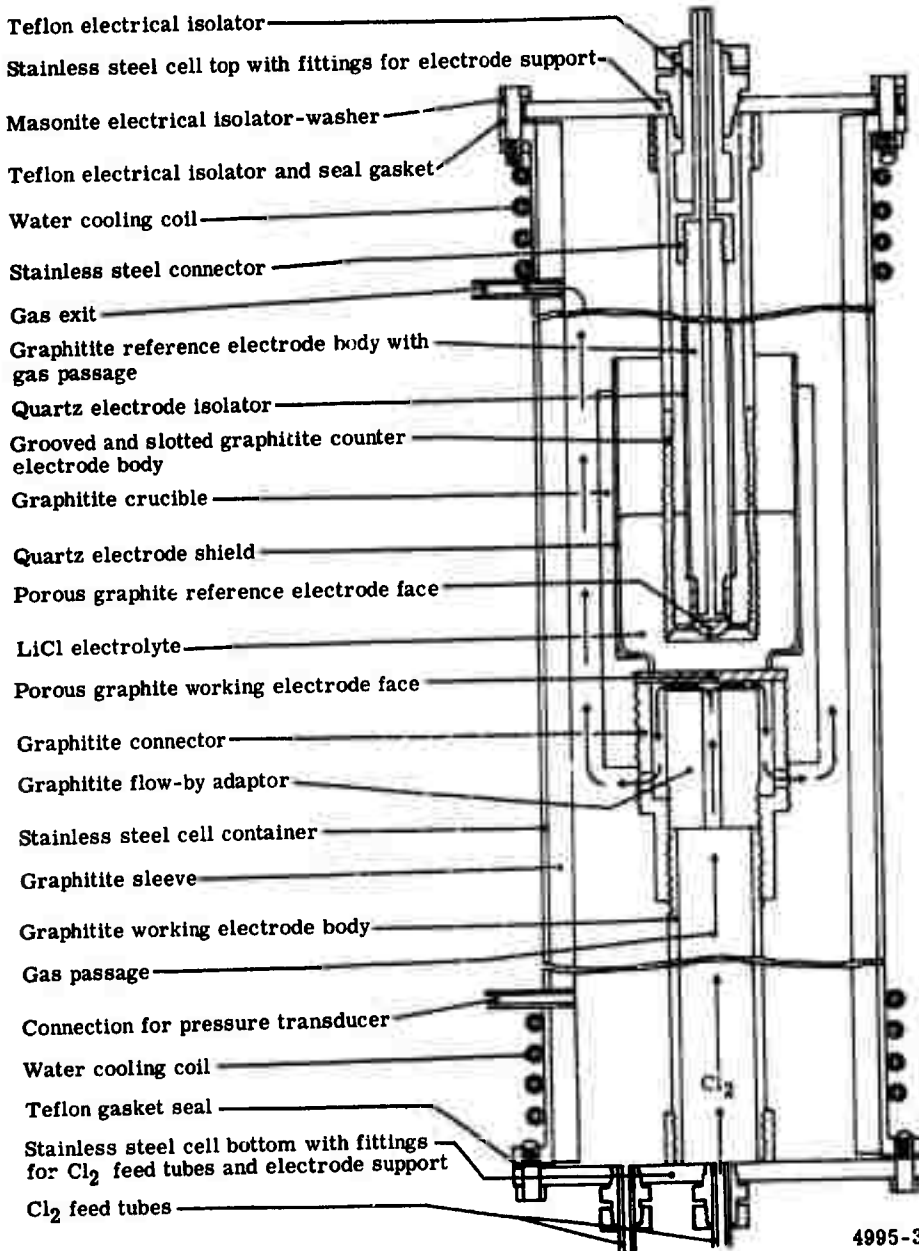
For the 2- and 5-atm tests, the Vycor tube was replaced by an outer stainless steel container with a Graph-i-tite A liner to protect the stainless steel from attack by hot Cl₂. The stainless steel container was made from a 3-ft length of 4-in. IPS X Sch 40 welded pipe of Type 316 SS. Flanges and cooling coils were welded on at both ends and the inside was bored out to a uniform circular diameter. A 0.5-in. wall Graph-i-tite A tube was machined to match the stainless steel pipe so that an average spacing of 0.010 in. existed between the graphite liner and the container. This space was filled with a suspension of Corning solder glass No. 7570 which was subsequently fused to provide an impervious coating between the graphite liner and the stainless steel.

Clamshell heaters around the center portion of the container provide the heat to raise the cell temperature to 650°C, while cooling coils near the flange cool the ends sufficiently so that Teflon gaskets and insulators can be used. All gas lines to and from the cell are stainless steel tubing with Al₂O₃ electrical isolators where necessary.

Gas Analysis System

An Allison built gas chromatograph, shown in Figure 6, was used for gas analysis. This device was built especially to handle Cl₂ and initially consisted of the following components:

- Helium carrier gas
- Milliflow flow control valve
- Barnsdale pressure valve activated by Ar pressure
- Beckman sampling valve
- AMS-5570 stainless steel tubing



4995-3

Figure 5. Pressure test cell.

- 15 w/o Fluorolube LG 160 on Deactigel 60/80 mesh column material
- F & M thermal conductivity detector
- Barber-Coleman Model 5020 power supply
- Sargent Model MR strip chart recorder

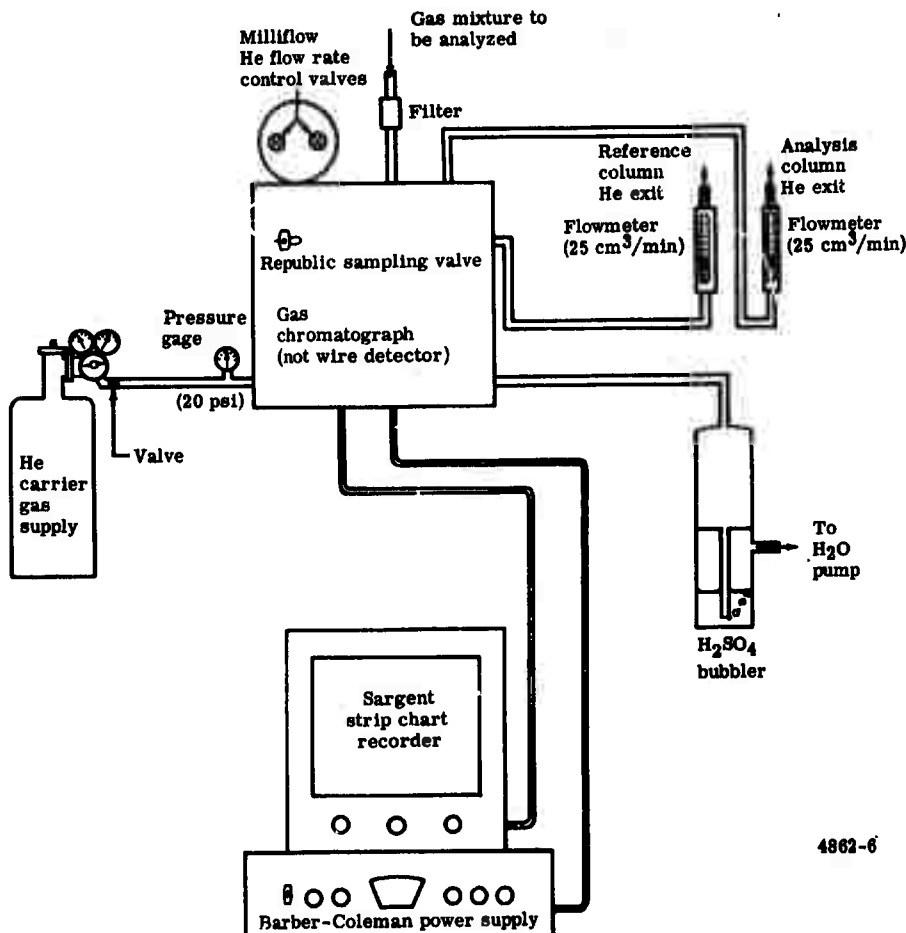


Figure 6. Gas analysis system.

After operating satisfactorily for about one month, a problem developed with the Beckman sampling valve. Particles of LiCl were carried by the gas stream and were deposited in the tubing. Some of these particles entered the valve and caused erosion. Leakage occurred between the various gas streams and part of the sample was lost. The following changes were made in the gas chromatograph to eliminate this problem. A 60-micron Nupro Model 4FR filter was placed in the gas stream to prevent clogging of the valves and tubing. The leaky sampling valve was replaced by a Republic Model A331-2SS-28 sampling valve. This new valve also eliminated the need for the pressure valve, the pressure valve was removed from the system. A final change in the operating procedure was to purge the system with Ar whenever it was not in use. This reduces the possibility of corrosion after the system has been exposed to Cl₂.

A typical chromatographic analysis is shown in Figure 7. The first peak is Ar shown at an attenuation of 200. This is followed by the CO₂ peak at an attenuation of 2 and the Cl₂ peak at an attenuation of 20. After accounting for the differences in attenuation and detector sensitivity to each gas, the peak areas obtained from the disk integrator plot yield the following composition—48.2% Ar, 0.8% CO₂, and 51.0% Cl₂.

Gas Control System

The gas control system, shown in Figure 8, consists of three parts—the vacuum unit, the pressure sensing unit, and the Cl₂ feed unit. The vacuum unit is used to outgas the cell and its components prior to a test run. It consists of a Welsh Model 1402 DUO-SEAL vacuum pump and a NRC Model 721 thermocouple vacuum gage.

The pressure sensing unit is a Teledyne Model 206SA pressure transducer. It is used to monitor cell pressure during a test run. A constant voltage input is supplied to the transducer by a Trygon Model HF-20-5A power supply; the output from the transducer (1 mv per 10 psig) is read on a TI 2 channel recorder Model No. FS02W6A.

Cl₂ and the inert impurity, Ar, are supplied to the cell from commercial cylinders. Originally, the best Cl₂ available in large quantities was 99.5% pure (Matheson). During this report period, however, 99.96% pure Cl₂ was obtained from Precision Gas Products and was subsequently used. The Ar is supplied by Airco Incorporated. In going to the cell, each gas passes through a 15-micron Nupro Model 4FR in-line filter to remove any foreign particles from the gas stream. The flow rate of each gas is monitored by Hastings Raydist Models LF-300 and LF-3K flowmeters which cover flows from 0 to 300 and 0 to 3000 cm³/min, respectively. Flow rate is controlled by a Whitey Model 22RS4 micrometering valve and a Moore Model 63SU-L flow controller.

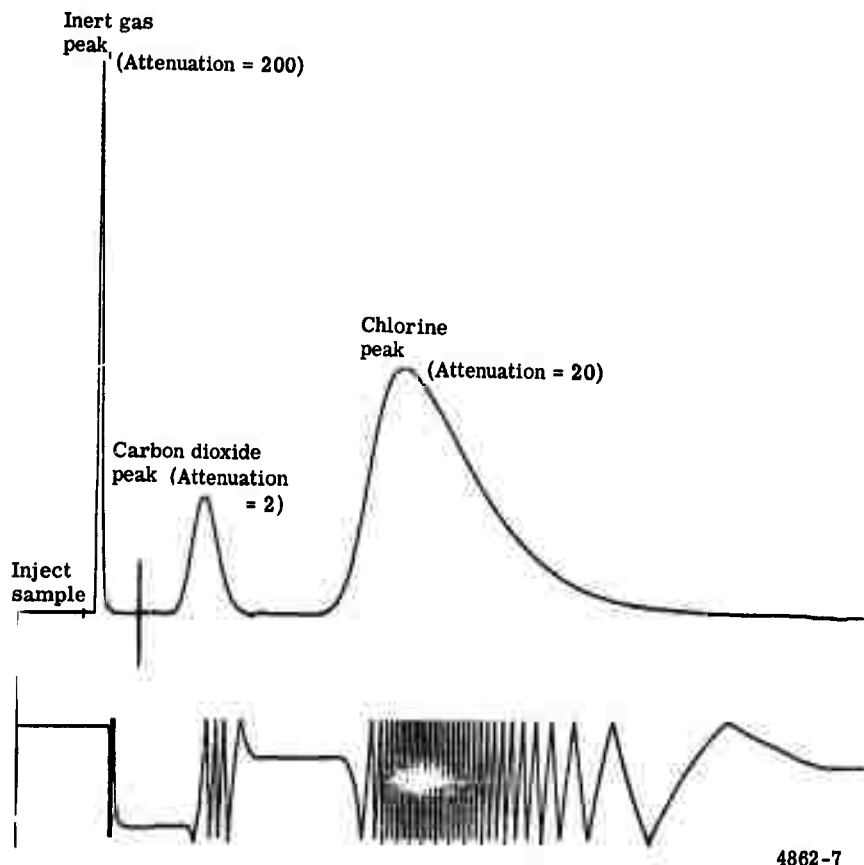
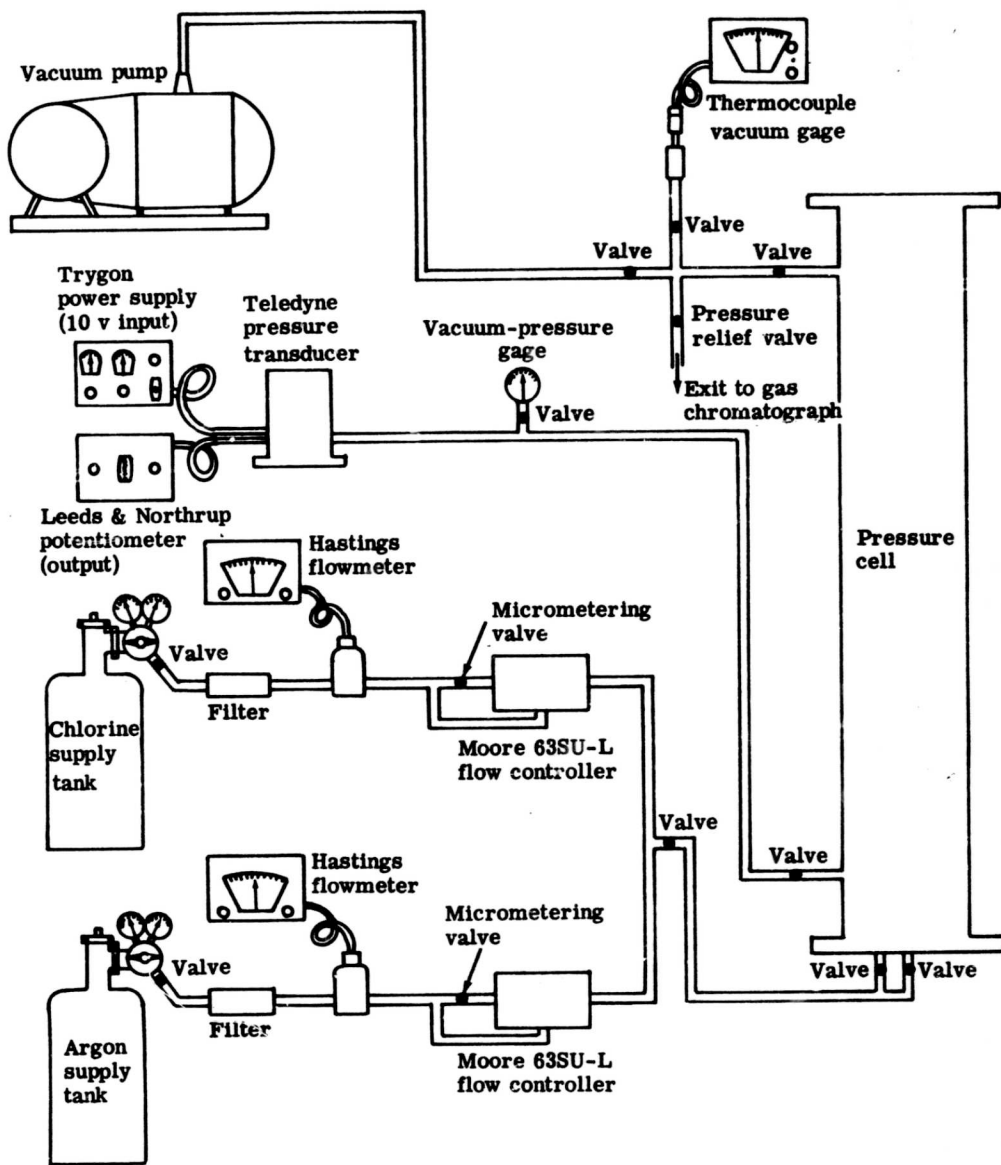


Figure 7. Typical gas chromatogram.

Electrical Instrumentation

The method used to obtain polarization data was to pass a d-c current between the working and counter electrodes. This was interrupted for less than 10^{-3} sec about 10 times per second, observing the polarization on an oscilloscope while no current flowed.

The overall electrical circuit is shown in Figure 9. The current flowing through the cell at any time is drawn from lead-acid batteries through the current controller. The working-to-reference electrode voltage and the working-to-counter electrode voltage are monitored continuously on two United Systems Corporation Digitec digital voltmeters. Most of this instrumentation is seen in Figure 10.

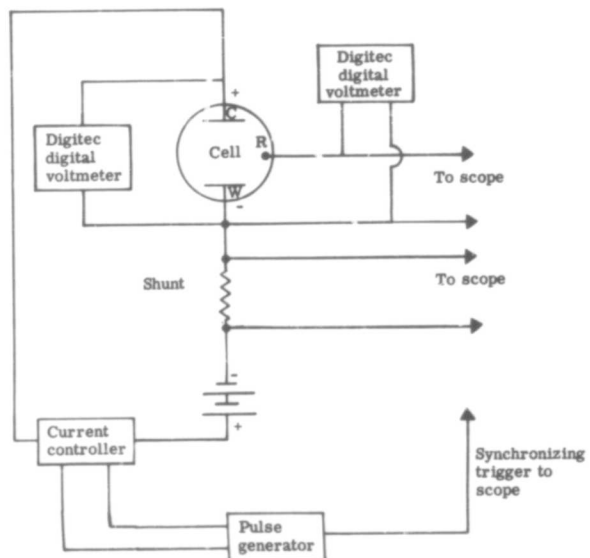


4862-8

Figure 8. Gas control system.

C = counter electrode
R = reference electrode
W = working electrode

Figure 9. Overall electrical circuit.



4862-9

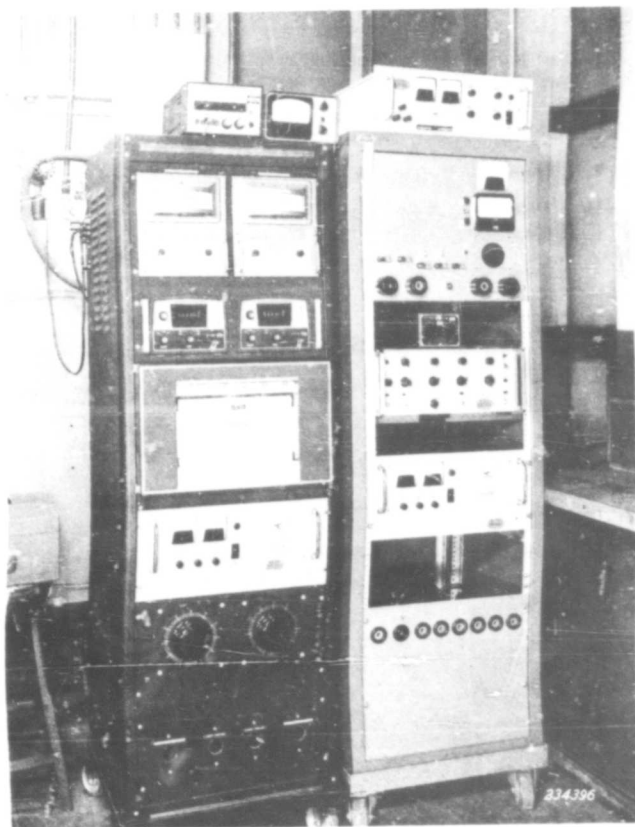


Figure 10. Electrical instrumentation for concentration polarization tests.

Allison

Two current controllers of the same general design were used. The first one was capable of controlling currents up to 70 amp which was sufficient for the early part of the work. However, as the work progressed, it became necessary to use higher currents to produce the desired polarization and a 150-amp current controller was constructed. This controller was designed to allow currents up to 150 amp to be cut off in less than 100 microsec. A simplified block diagram of the controller is shown in Figure 11.

Current in the controller is provided by either a battery or low ripple d-c supply. Control of this current is accomplished by 15 germanium power transistors in parallel to provide reasonable power dissipating capabilities. Current flow through the 150-amp shunt provides a 0- to 50-mv current signal which is connected through feedback resistor R_4 to the operational amplifier input. A d-c voltage from the current adjust potentiometer and external signals from a ramp or pulse generator are also connected to the amplifier input.

Normal operation is to set the current adjust potentiometer to obtain the required steady-state current flow through the cell. The pulse and ramp signals are zero at this time. The output of the operational amplifier goes negative just enough to make the currents in R_3 and R_4 equal. If a negative pulse of sufficient amplitude is fed into the pulse generator in-connector, the output power transistors are turned off and the current through the cell is reduced to zero. The time required for the cell current to drop to zero varies from 30 to 80 microsec depending on the initial d-c current flow.

Several protective circuits are provided in the control to minimize the possibility of damage to the cell or controller. A wattmeter-relay senses the power being dissipated in the

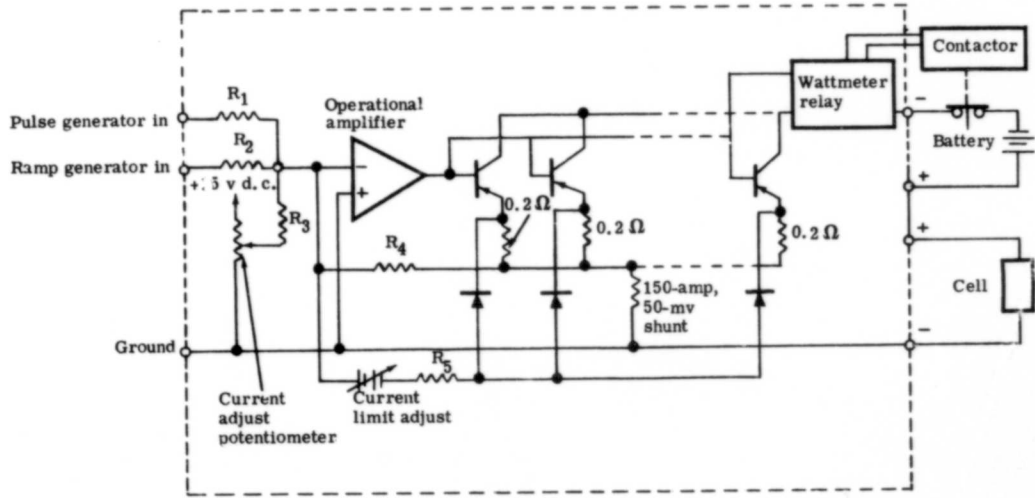


Figure 11. Simplified diagram of the 150-amp current controller.

Allison

power transistors and opens a contactor in series with the battery whenever this power exceeds the design limit of 500 w. A current limit adjust is also provided so that a maximum output current from the controller can be set at any value from 20 to 150 amp. This 150-amp current controller is shown in Figure 12.

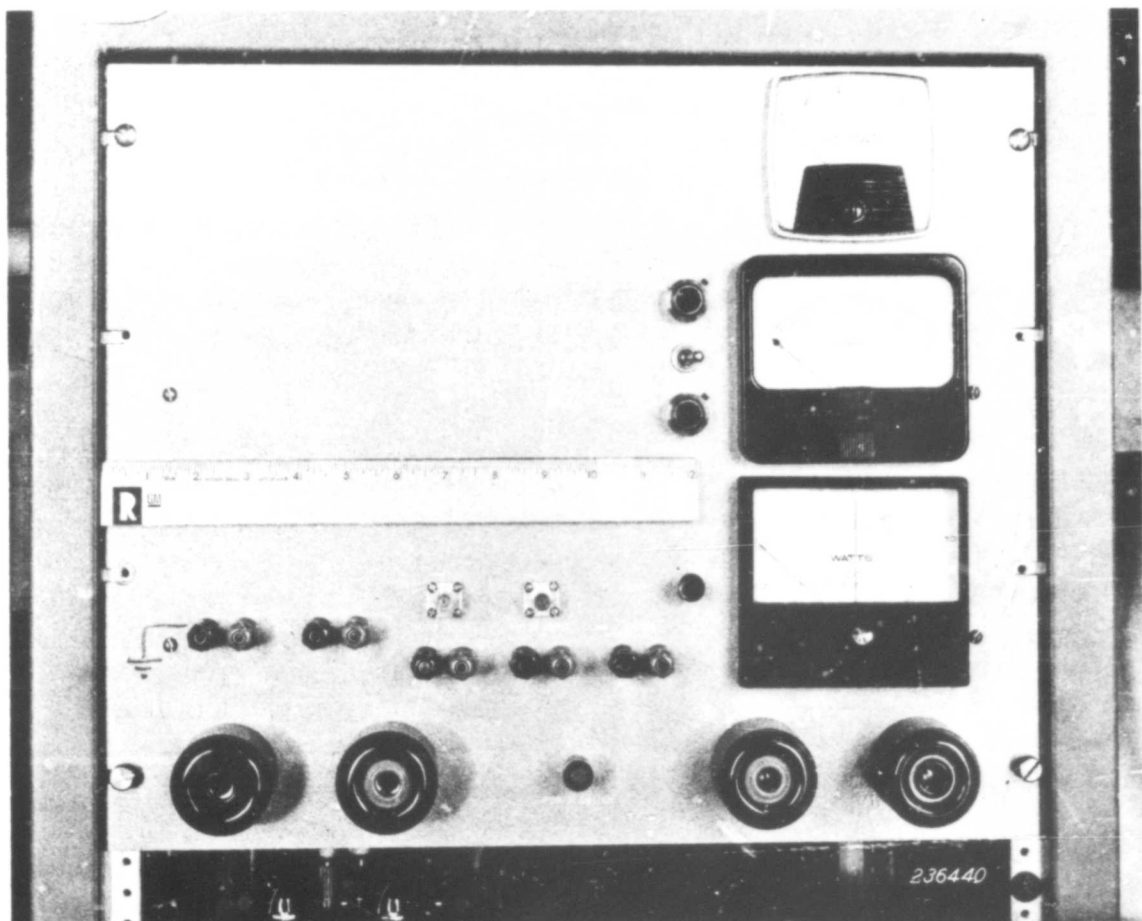


Figure 12. 150-amp current controller.

Testing Procedure

After the cell is assembled, it is placed inside the furnace and connected to the gas feed system, the gas analysis system, and the electrical system. The cell is then purged with Ar and heated gradually to 750°F to remove any water vapor. Cl₂ is then purged through the cell and the temperature is increased to 1200°F. The cell is kept at operating temperature with Cl₂ passing through it for 16 to 20 hr to treat the electrodes and purge the system. After the Cl₂ bake treatment is completed, the Cl₂ is flushed out with Ar, the reference electrode is removed, and the LiCl electrolyte is added to the cell through the hollow counter electrode. When the electrolyte has melted, the reference electrode is replaced in the cell. While the system is reaching thermal equilibrium, Cl₂ and Ar flows are started and adjusted to give the required gas composition as determined by the gas chromatograph. After all systems have reached equilibrium, sufficient current is passed to polarize the working electrode to 0.5 v. The flow rates of the gases are then adjusted to give 100% excess Cl₂ over that required to support the current being drawn at 0.5-v polarization while maintaining the gas composition. Data are taken after the new flow rates have been reached. The method used in taking data is to increase the current until the electrode shows various values of polarization between 0.1 and 1.0 v. The polarization is determined by interrupting the current for less than 10⁻³ sec and observing the working-to-reference electrode voltage on an oscilloscope.

The oscilloscope trace was photographed and the concentration polarization was determined by extrapolating the recorded polarization back to the moment the current interruption started. This usually meant an extrapolation of 10⁻⁴ sec which is the time required for the current to go to zero and for any activation polarization to decay. Some typical traces are shown in Figure 13. The time base in each case is 10⁻⁴ sec/cm. The current trace is shown in the center of each picture. The current is switched off in each case in about 40 microsec. The voltage traces are offset on the time axis with respect to the current trace by 440 microsec. The zero line for the voltage is the second line from the top. In each case, the voltage trace has been extrapolated over the initial 60 to 100 microsec to give the concentration polarization at the instant of interruption.

The transients of Figure 13 were obtained on a 9 cm² Poco-AX graphite electrode 1/16-in. thick at 650°C, 1 atm, using 95% Cl₂. The data obtained were as follows:

Trace	Current (amp)	Concentration polarization (v)
A	16.5	0.11
B	23	0.2
C	26.5	0.4
D	29	0.6
E	29.8	0.8
F	30.5	1.05

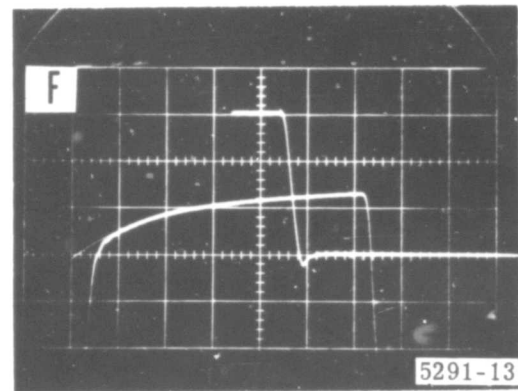
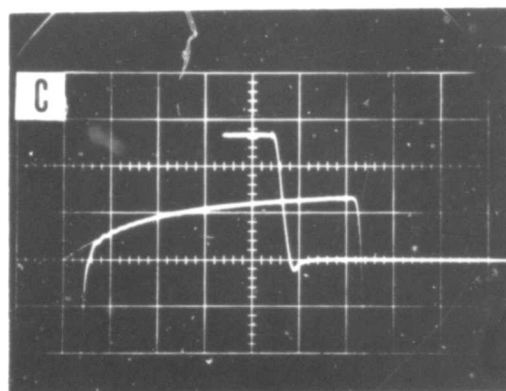
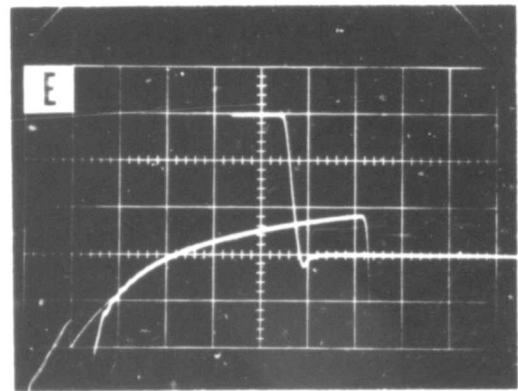
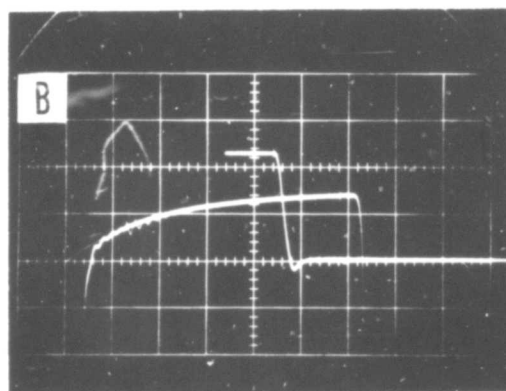
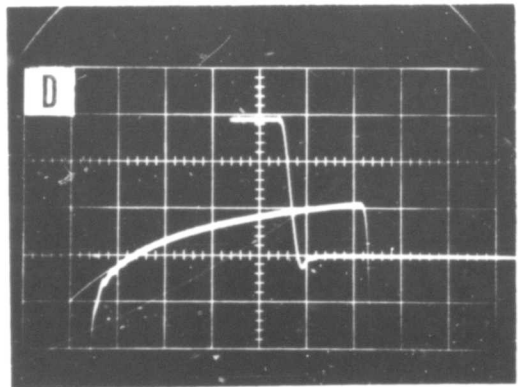
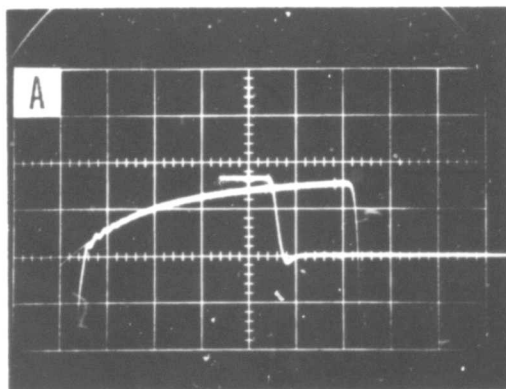


Figure 13. Typical traces obtained during the concentration polarization study.

Results

In this way, concentration polarization data were obtained for Poco-AX porous graphite electrodes 1/8- and 1/16-in. thick at total pressures of 1, 2, and 5 atm using gas mixtures containing 50, 80, 95, and 99.9% Cl₂. Table II gives a summary of all the data. Each data point is the average of at least 10 determinations taken with both increasing and decreasing currents. All the data were obtained at a nominal temperature of 650°C. However, at high current densities the temperature rose unavoidably due to I²R, T_{AS}, and I_g heating in the cell. Since the temperature affects a number of the properties which determine the Cl₂ electrode performance, these higher temperature data are not strictly comparable to the 650°C data and are shown in brackets in Table II. For the same reason, these data are plotted in Figure 20, separate from the 650°C data. At low polarizations, the 1/8-in. thick electrode performed better at 5 atm than the 1/16-in. thick electrode. Similar behavior has been observed in complete Li-Cl₂ cells. This is probably due to the greater penetration of electrolyte into the porous electrode due to a greater ΔP developed across the thicker electrode. Such increased penetration is equivalent to an increase in area; it results in improved performance in a manner similar to grooving the electrode.

Discussion

The concentration polarization data shown in Figures 14 through 20 are of a form typical of concentration polarizations. For a plane electrode, the i- η relationship is

$$\eta = \frac{RT}{nF} \ln \frac{i_L}{i_L - i} \quad (25)$$

where i_L = limiting current density.

The smooth curves drawn through the experimental points in Figures 14 to 20 have the same general shape as Equation (25) but deviate in detail, particularly at high current densities. This is probably due to the fact that the electrode has a range of different pore sizes each with its own characteristic limiting current density. Therefore, the i- η relationship in this case is a complex average of a large number of individual relationships similar to Equation (25). The average would be a complex one since the pores of different sizes (and, therefore, different activities) are interconnected not only electronically through the graphite but also ionically through the electrolyte and in the gas phase. Cl₂ and impurities can flow and diffuse from one pore to another, and the average is not a simple average of parallel paths. No detailed theoretical treatment of the shape of the i- η curve has been made. The theoretical treatment attempts to predict the limiting current

Table II.
Electrode performance data in amp/cm².

η ₂ (v)	1 atmosphere				2 atmospheres				5 atmospheres				
	50% Cl ₂	80% Cl ₂	95% Cl ₂	99+% Cl ₂	50% Cl ₂	80% Cl ₂	95% Cl ₂	99+% Cl ₂	50% Cl ₂	80% Cl ₂	95% Cl ₂	99+% Cl ₂	
1/8-in. electrode	0.1	0.37	0.71	1.34	1.90	0.37	1.06	2.34	4.30	0.52	1.53	2.65	(5.40)
	0.2	0.48	0.94	1.58	2.46	0.47	1.24	2.60	5.87	0.59	1.70	3.04	(8.10)
	0.4	0.53	1.09	1.80	2.99	0.56	1.41	2.76	6.53	0.64	1.78	3.28	(11.40)
	0.6	0.56	1.16	1.87	3.29	0.62	1.48	2.90	6.76	0.67	1.89	3.39	(13.20)
	0.8	0.58	1.23	1.96	3.47	0.66	1.56	2.95	7.01	0.70	1.94	3.50	(14.50)
	1.0	0.59	1.25	2.01	3.57	0.68	1.61	2.99	7.17	0.71	1.97	3.60	(15.45)
1/16-in. electrode	0.1	0.47	1.02	1.73	2.98	0.60	1.59	3.24	(2.05)	0.71	1.91	3.89	(3.50)
	0.2	0.65	1.42	2.37	3.98	0.78	1.91	3.70	(4.30)	0.83	2.17	4.25	(6.63)
	0.4	0.76	1.68	2.86	4.87	0.90	2.16	4.12	(8.40)	0.91	2.32	4.42	(12.25)
	0.6	0.83	1.84	3.12	5.29	0.97	2.26	4.32	(11.33)	0.97	2.44	4.57	(17.40)
	0.8	0.86	1.89	3.21	5.59	1.00	2.33	4.43	(12.65)	1.00	2.49	4.66	---
	1.0	0.88	1.93	3.30	5.74	1.01	2.41	4.50	(13.15)	1.02	2.54	4.72	---

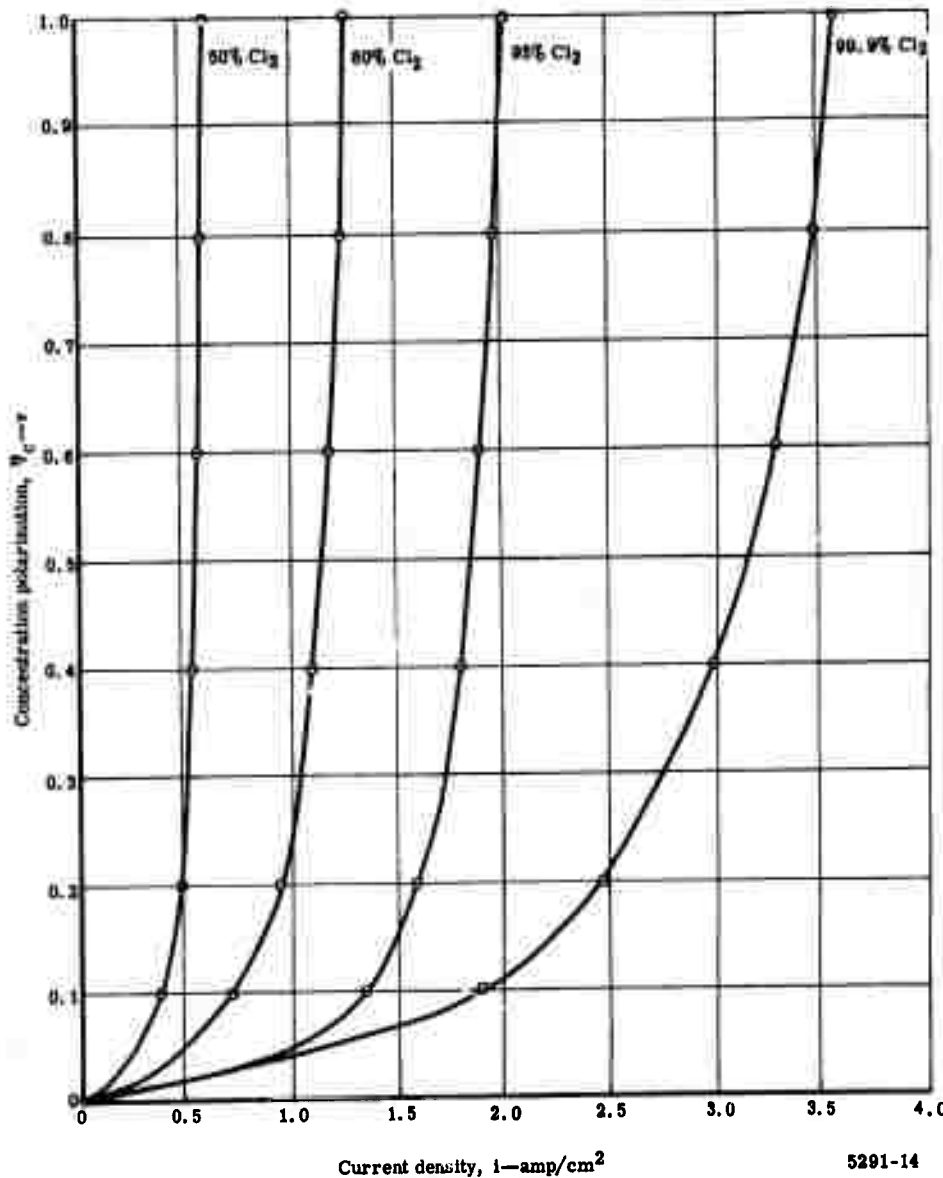


Figure 14. Concentration polarization versus current density for a 1/8-in. electrode at 1 atm.

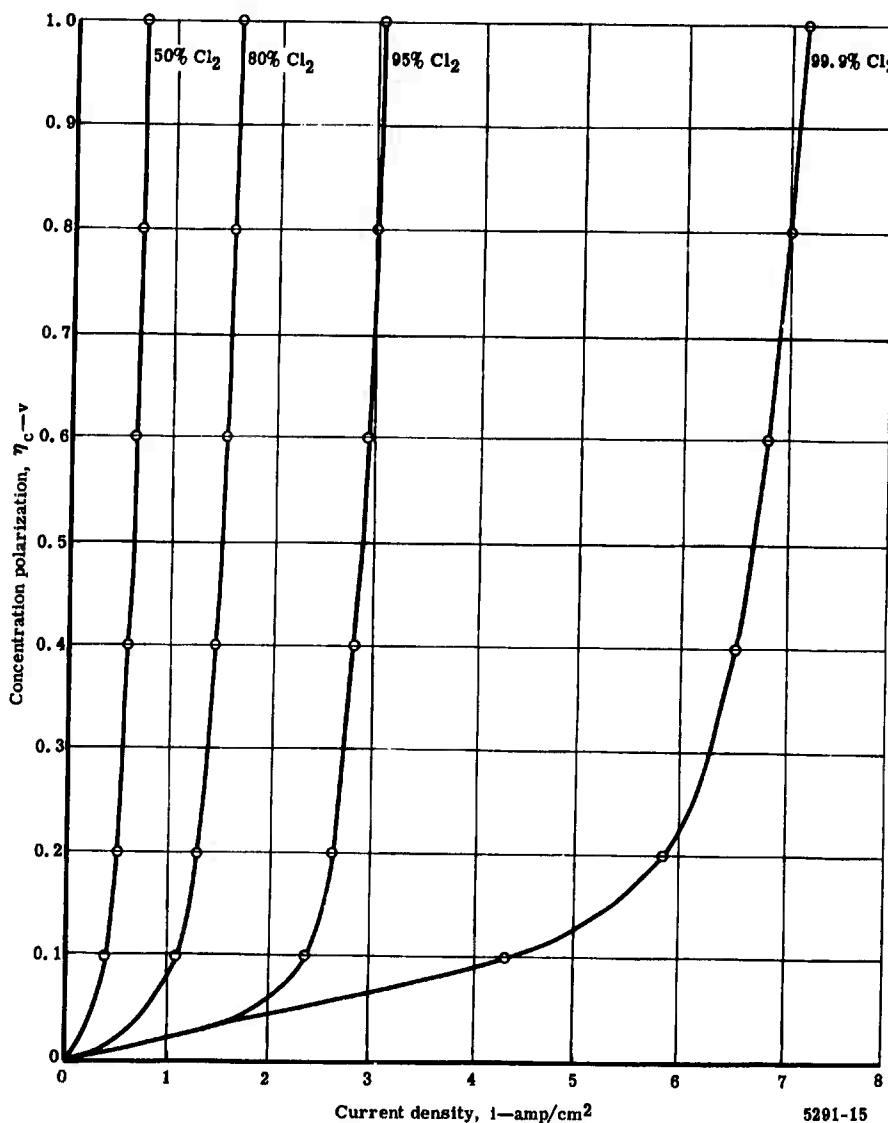


Figure 15. Concentration polarization versus current density for a 1/8-in. electrode at 2 atm.

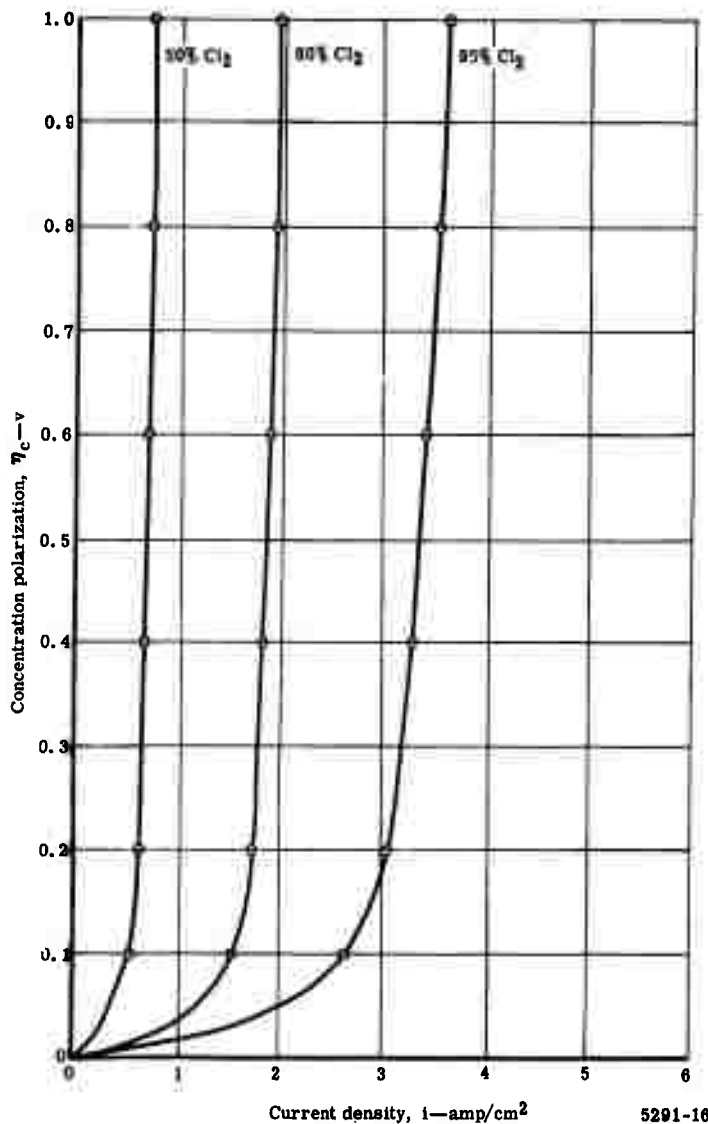


Figure 16. Concentration polarization versus current density for a 1/8-in. electrode at 5 atm.

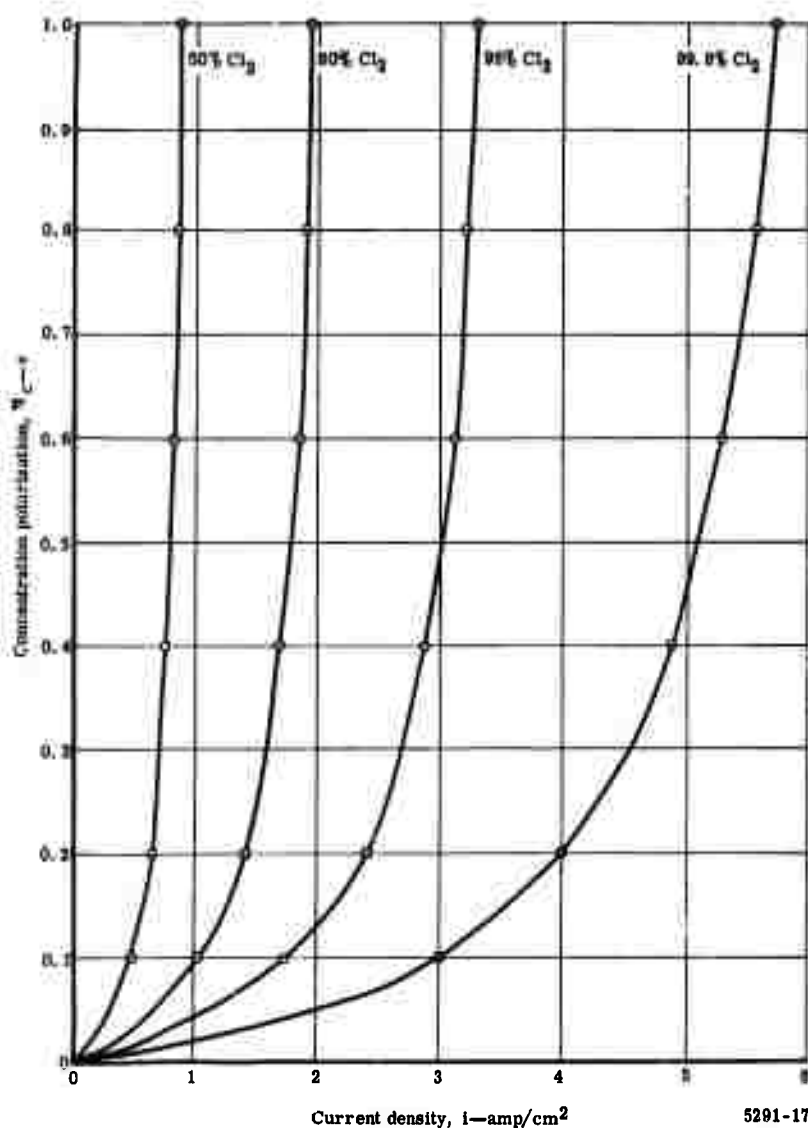


Figure 17. Concentration polarization versus current density for a 1/16-in. electrode at 1 atm.

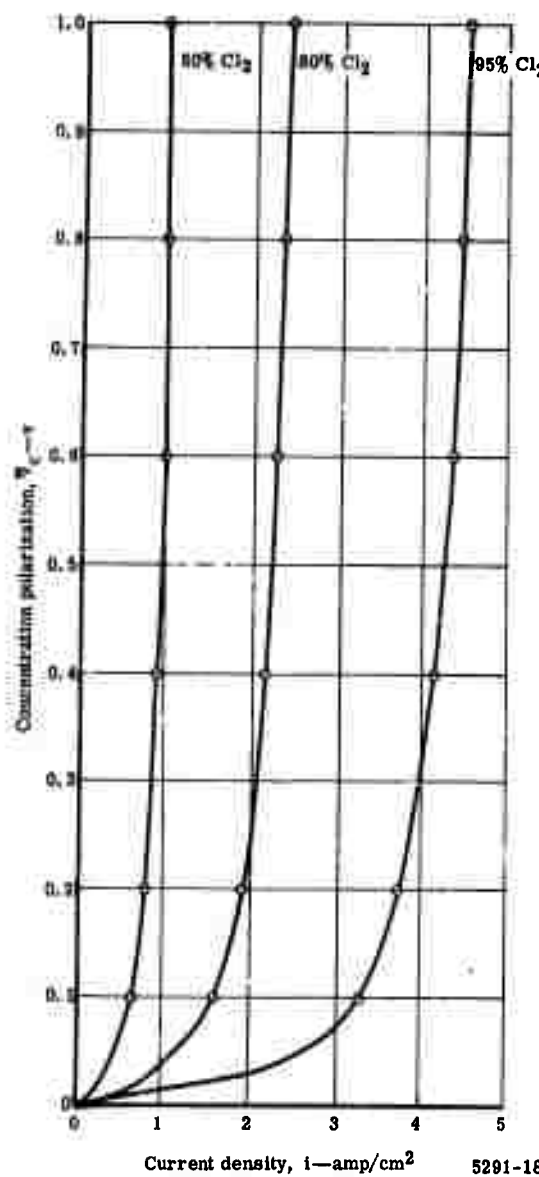


Figure 18. Concentration polarization versus current density for a 1/16-in. electrode at 2 atm.

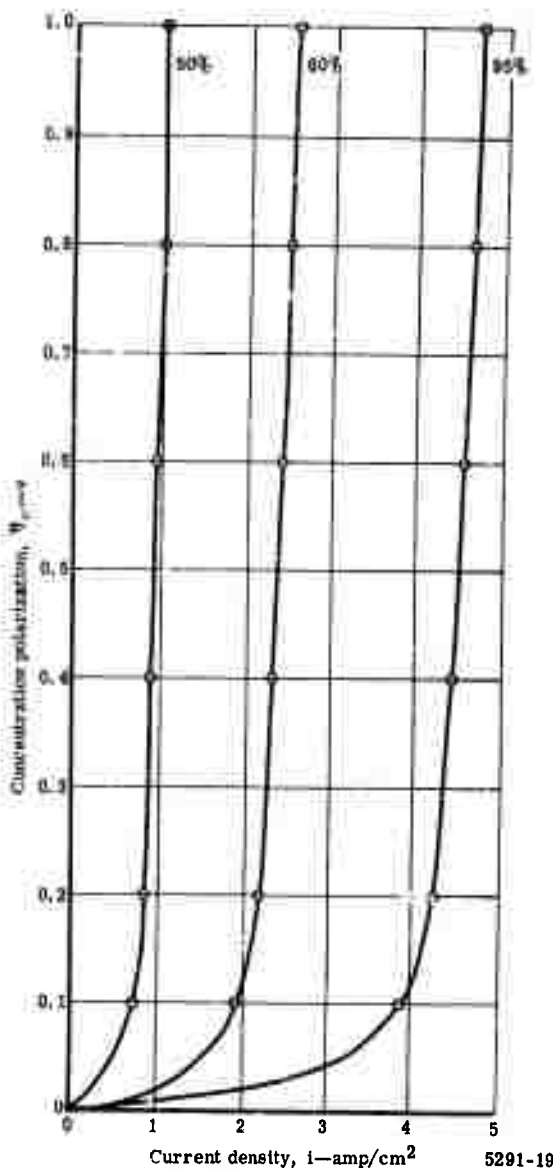


Figure 19. Concentration polarization versus current density for a 1/16 in. electrode at 5 atm.

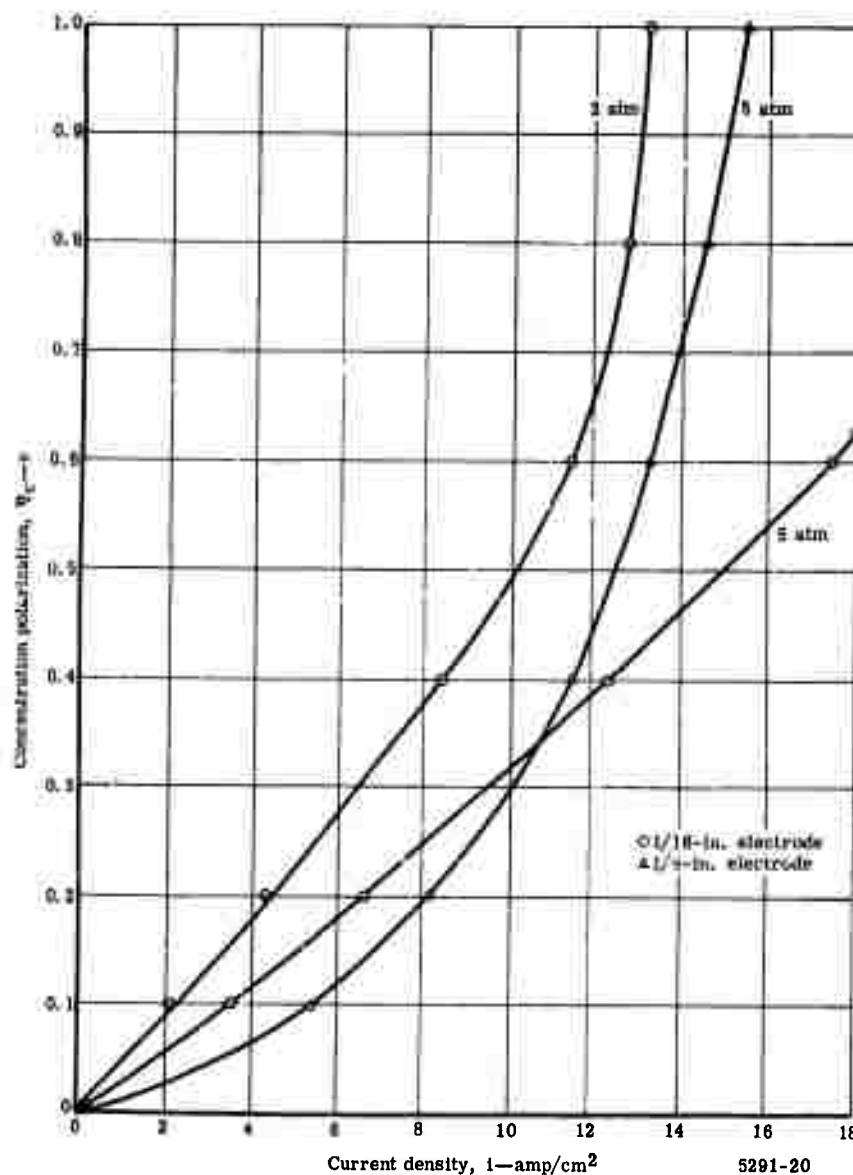


Figure 20. Concentration polarization versus current density for 1/8- and 1/16-in. electrodes using pure Cl_2 .

density which can be obtained under various conditions of pressure, impurity level, and electrode thickness. The results of these calculations are compared with the experimental limiting current densities in Table III. The experimental limiting current density is arbitrarily taken as the current density at 0.5-v polarization which is obtained by interpolation from the experimental data in Table II.

Table III.
Comparison between calculated and experimental limiting current densities (i_L).

	P_T	1/8-in. electrode		1/16-in. electrode	
		Calculated i_L (amp/cm ²)	Experimental i_L (amp/cm ²)	Calculated i_L (amp/cm ²)	Experimental i_L (amp/cm ²)
$P_T = 1 \text{ atm}$	99.9% Cl_2	2.79	3.15	4.84	5.10
	95% Cl_2	2.04	1.84	3.69	3.01
	80% Cl_2	1.22	1.13	2.27	1.77
	50% Cl_2	0.55	0.55	1.04	0.81
$P_T = 2 \text{ atm}$	99.9% Cl_2	5.96	6.67	10.3	10.1
	95% Cl_2	2.83	2.82	5.39	4.26
	80% Cl_2	1.54	1.46	2.97	2.22
	50% Cl_2	0.67	0.60	1.29	0.95
$P_T = 5 \text{ atm}$	99.9% Cl_2	7.25	12.4	14.2	14.9
	95% Cl_2	3.15	3.34	6.21	4.52
	80% Cl_2	1.70	1.83	3.34	2.39
	50% Cl_2	0.73	0.66	1.44	0.95

For the 1/8-in. thick electrode, the agreement is within the precision of the experimental data, which is about $\pm 10\%$ except for the 5-atm pure Cl_2 points. For the 1/16-in. thick electrode, the calculated values of i_L are generally higher than the experimental data by 25 to 40%. A possible explanation of this is that for the thinner electrode the ΔP developed across the electrode will be less. Therefore, the effective roughness of the electrode will be less since less electrolyte penetration will occur. By reducing the roughness factor used in the calculations from 5 to 3, the calculated values are reduced sufficiently so that the calculated limiting current densities are on the average high by only 12%. This is close to the precision of the experimental data. However, the roughness factor of 5 has been retained in the calculated values shown in the succeeding plots of i_L versus various parameters. Figure 21 shows i_L for a 1/8-in. thick electrode as a function of pressure and impurity level, while Figure 22 shows i_L at a fixed impurity level (0.1% impurities)

as a function of pressure and electrode thickness. In each case, relevant experimental points are also shown. Figure 21 clearly shows that increasing the total pressure beyond 5 atm results in little or no improvement in electrode performance. Even pressure increases above 2 atm are only useful when the Cl_2 contains less than 5% impurities. The effect of reducing electrode thickness is demonstrated by Figure 22; however, lower values of i_L were often observed on the thinner electrodes.

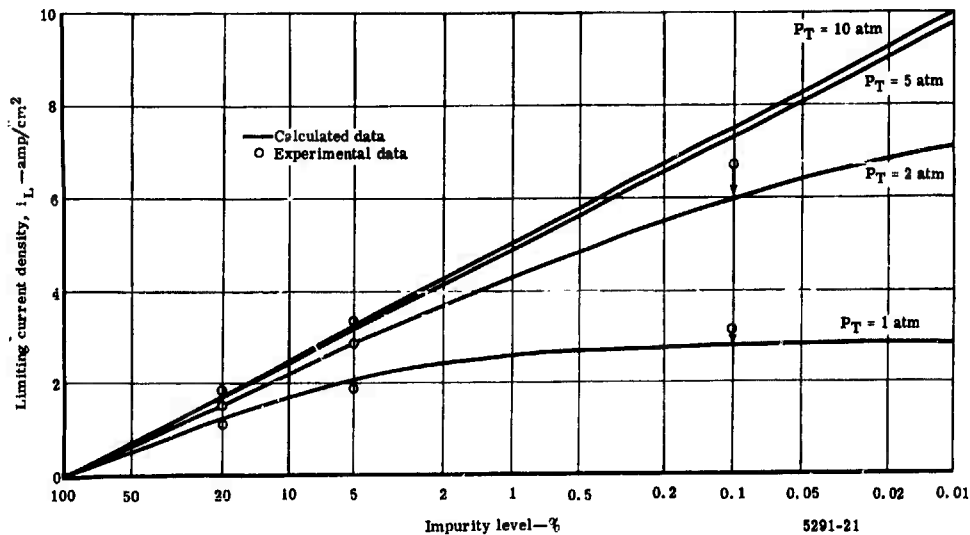


Figure 21. Limiting current densities for 1/8-in. thick Poco-AX electrode.

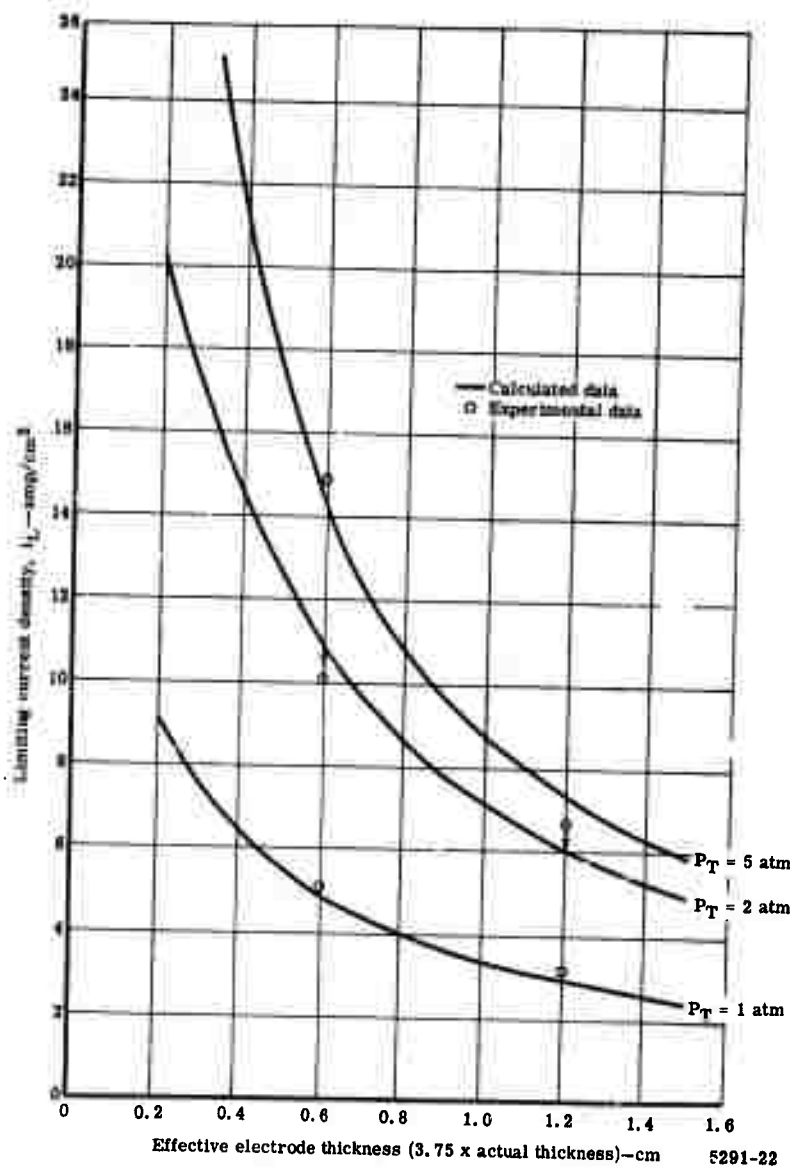


Figure 22. Limiting current density at an impurity level of 0.1% for Poco-AX porous graphite.

Finally, Figure 23 shows once again that to realize high current densities on the Cl_2 electrode pure Cl_2 must be used at somewhat elevated pressures (3 to 5 atm) using fairly thin electrodes ($\approx 1/16$ in.).

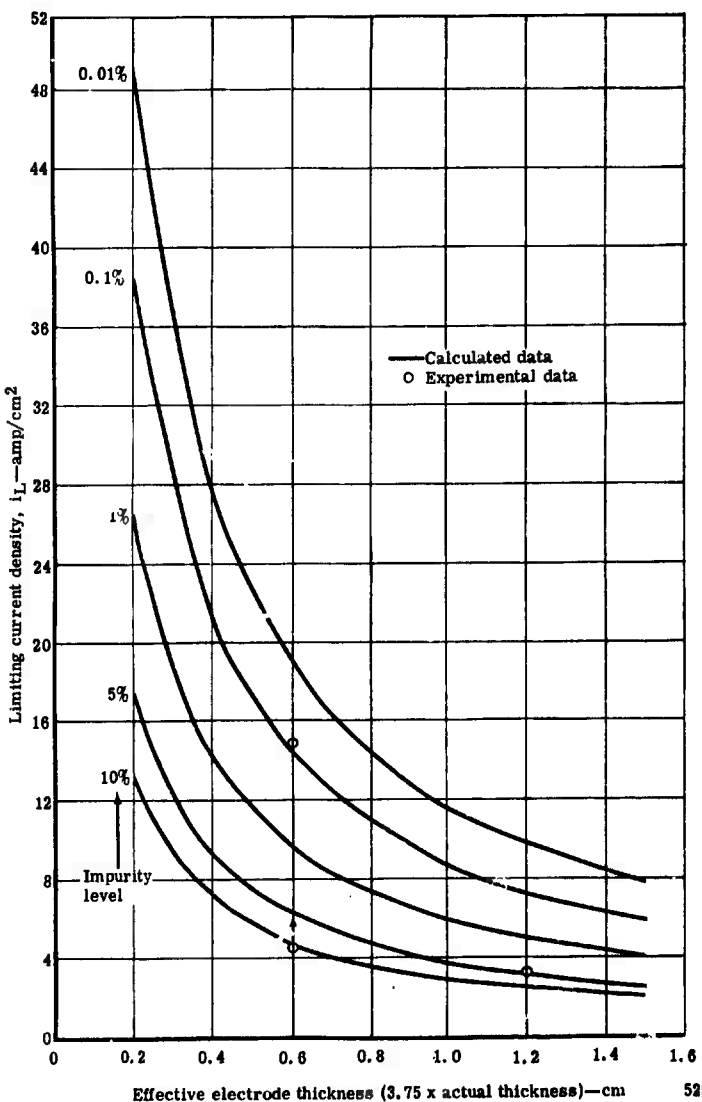


Figure 23. Limiting current density for Poco-AX at 5 atm.

ACTIVATION POLARIZATION

Theory

The activation polarization associated with the overall process



has recently been studied by Triaca, et al* at 1 atm on FC-11 porous graphite in LiCl at 650°C.

They showed that for the anodic process the discharge step



was fast and that the rate determining step (R. D. S.) was the recombination of Cl atoms



This mechanism for the Cl_2 electrode reaction is similar to the Volmer mechanism for the H_2 evolution reaction**

$$i = i_0 \left[\frac{\theta}{\theta_0} \exp \left(\frac{-\alpha nF}{RT} \eta \right) - \frac{1-\theta}{1-\theta_0} \exp \left(\frac{(1-\alpha)nF}{RT} \eta \right) \right] \quad (29)$$

where

θ = surface coverage of adsorbed Cl atoms at overpotential, η

θ_0 = surface coverage of adsorbed Cl atoms at equilibrium ($\eta=0$)

The exchange current density found by these authors was 0.19 amp/cm² at 656°C.

The activation polarization data obtained will be interpreted on the basis of Equation (29).

In the present work, the exchange current density was determined for the Poco-AX porous graphite material at 1, 2 and 5 atm pressure.

*Triaca, W. E., Solomons, C., and O'M Bockris, J. University of Pennsylvania, private communication.

**Vetter, K. J. Electrochemical Kinetics, New York: Academic Press, 1967, p. 528.

Test Cell

The test cell was the same as that used for the concentration polarization studies and only the functions of the electrodes was changed. The porous electrode in the bottom of the Graph-i-tite A cup was made the reference electrode, while the two concentric electrodes coming down from the top were the working and counter electrodes. By passing the current between the concentric electrodes, faster rise times could be obtained and more accurate activation polarization values could be measured.

Instrumentation

Since smaller electrodes could be used (1.39 to 0.09 cm²) in these experiments, the current controller was not necessary and the HP 214 pulse generator was used to supply currents to 2 amp directly to the working and counter electrodes. The voltage between the working electrode and the reference electrode was observed on the Tektronix 555 oscilloscope and the trace was photographed. The current pulses varied in length from 1 to 10 msec depending on the current density. The pulses were made long enough to establish the activation polarization but not long enough to form a gas film (anode effect) or gas bubbles on the electrode since these caused changes in effective electrode area. The activation polarization was measured immediately after the current was turned off again so that no IR drop was included in the measurement.

Results

Activation polarization data were obtained for Poco-AX porous graphite Cl₂ electrodes in LiCl at 650°C using pure Cl₂ (99.9%) at 1, 2, and 5 atm pressure. Some typical sets of transients are shown in Figure 24. These transients refer to a 1.39 cm² electrode of Poco-AX at 1 atm. The time base is 20 microsec/cm in each case. The current and activation polarization are indicated on each set. The polarization was read by extrapolating the instant the current was switched off, since some ringing occurred during the first 10 to 20 microsec.

A typical set of polarization data obtained in this way is shown in Figure 25 for a 1.39 cm² electrode at 1 atm. The polarization data for the anodic process (2 Cl⁻ → Cl₂ + 2 e⁻) behave normally, while the polarizations for the cathodic reaction (Cl₂ + 2 e⁻ → 2 Cl⁻) are larger than expected. (The dashed curve is the mirror image of the anodic side.) There are two possible reasons for this: (1) the activation polarization may be nonsymmetric about the equilibrium potential (i.e., $\alpha \neq 0.5$) and (2) the cathodic data may include some concentration polarization.

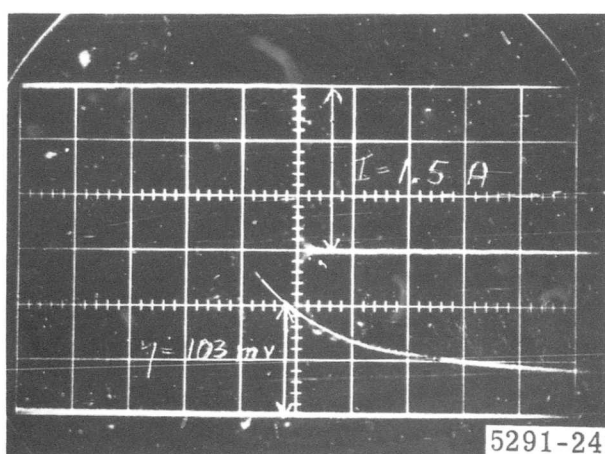
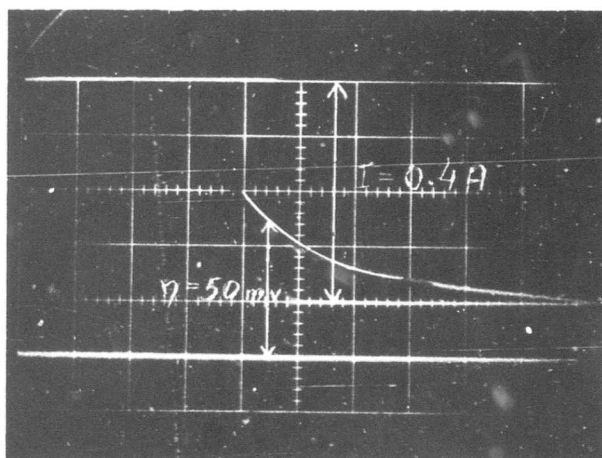
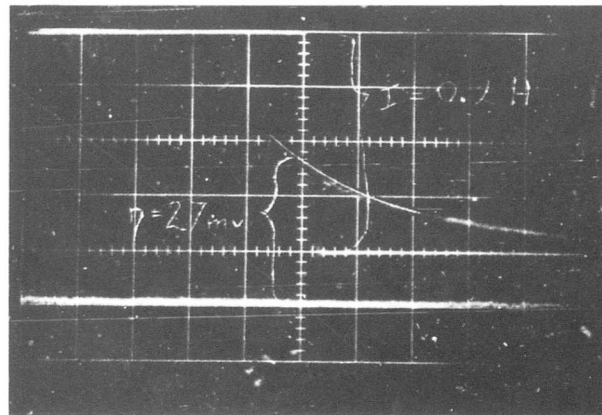


Figure 24. Typical current and anodic polarization traces for 1.39-cm^2 Poco-AX electrode at 1 atm ($20 \mu\text{sec/cm}$).

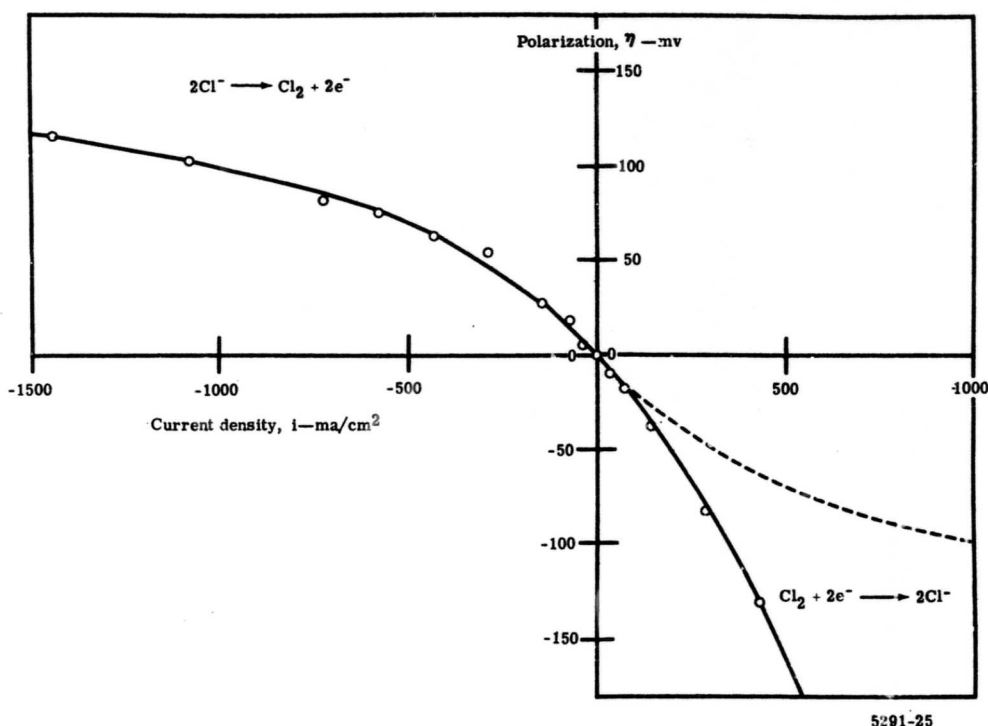


Figure 25. Polarization data for Poco-AX at 1 atm.

In view of the latter possibility, most data were taken for the anodic process.

All the data for eight runs on four different 1.39 cm^2 electrodes at 3 pressures have been averaged and are shown in Table IV.

Additional data were taken on smaller electrodes (0.24 and 0.09 cm^2). However, these data were judged to be less reliable for the following reasons.

- The electrode areas were less accurately known.
- These data showed a wide scatter and a definite time dependence—i.e., electrode performance improved with time over a period of days.
- During these tests, a crack developed in the graphite liner of the pressure cell causing corrosion of the stainless steel by Cl_2 . The metal chlorides formed may have affected the data.

Table IV.
Average anodic polarization data ($2 \text{Cl}^- \rightarrow \text{Cl}_2 + 2 \text{e}^-$)
for 1.39 cm^2 electrodes.

Current density (ma/cm ²)	Polarization (mv)		
	1 atm	2 atm	5 atm
36	8.2	4.9	3.3
72	15.6	9.8	7.0
144	28.2	18.9	12.9
288	48.3	32.3	23.7
432	65.1	43.0	32.0
576	82.4	57.6	40.1
720	95.8	65.8	46.5
1080	113.8	86.8	54.4
1440	124.4	96.8	62.5

For these reasons, only those runs on the smaller electrodes which were in general agreement with the data obtained on the larger electrodes have been used in calculating the final values of the exchange current density.

Discussion

The equation relating current density (i) and activation polarization (η)

$$i = i_0 \left\{ \exp \left(\frac{-anF}{RT} \eta \right) - \exp \left(\frac{(1-a)nF}{RT} \eta \right) \right\} \quad (30)$$

can be rearranged to

$$\log \left\{ \frac{i}{1 - \exp \left(\frac{nF}{RT} \eta \right)} \right\} = \log i_0 - \frac{a nF}{2.303 RT} \eta \quad (31)$$

By plotting the experimental data according to Equation (31), a straight line is obtained which has a slope of $-a$ and an intercept at $\eta = 0$ of $\log i_0$. This method gives more accurate estimates of i_0 and a than the usual Tafel plot when the data include low values of η .

At 650°C using $n = 2$, $RT/nF = 39.76 \text{ mv}$ and $2.303 RT/nF = 91.5 \text{ mv}$. Figure 26 shows the data of Table IV plotted in the form

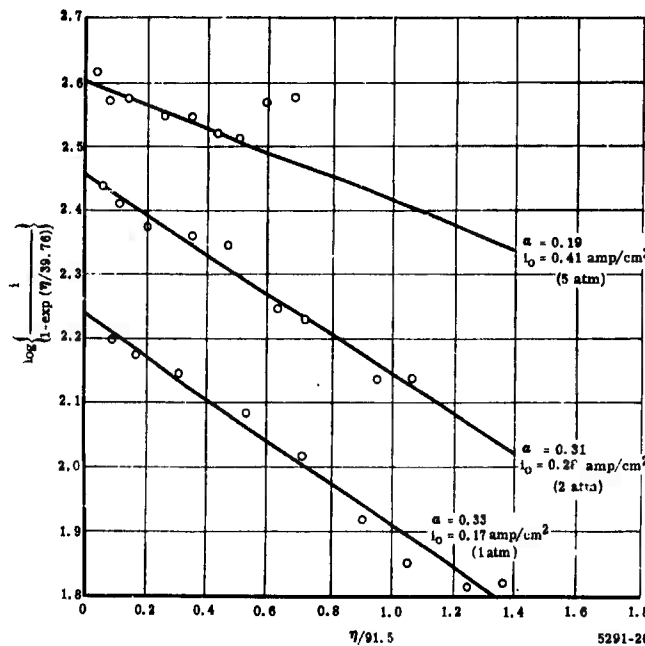


Figure 26. Data from Table IV plotted to evaluate α and i_0 .

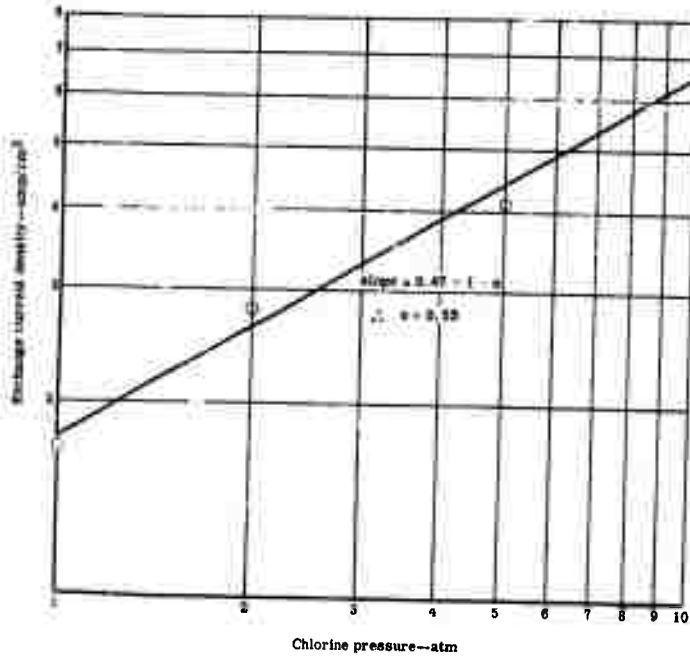
$$\log \left\{ \frac{i}{1 - \exp \left(\frac{\eta}{39.76} \right)} \right\} = \log i_0 - \alpha \frac{\eta}{91.5} \quad (32)$$

The values of α and i_0 obtained are shown in Figure 26. This gives $\alpha \approx 0.2$ to 0.3 .

Another method of obtaining α is

$$\left(\frac{\partial \log i_0}{\partial \log P_{Cl_2}} \right)_{a_{Cl^-}} = 1 - \alpha \quad (33)$$

This plot is shown in Figure 27 which leads to a value of 0.33 for α . These apparently conflicting numbers obtained from the same data can be explained by assuming a potential dependent surface coverage of Cl atoms and using Equation (29). At increasingly positive potentials reaction, Equation (27) will go further to the right and the coverage θ with Cl



5291-27

Figure 27. Plot of $\log i_0$ versus $\log P$.

atoms will increase. This increases the rate of the R. D. S. given by Equation (28) and leads to an effectively lower value of a . Therefore, the correct value of a is that obtained from Figure 27. Plots of Equation (31) should give the same value of a when plotted at constant coverage θ rather than at constant pressure. However, since no information is available regarding the coverage θ as a function of pressure and electrode potential, this cannot be checked at this time. The stoichiometric number (ν) for the overall reaction is the number of times the R. D. S. occurs for one completion of the overall reaction. It is given by

$$\nu = \frac{nF}{RT} i_0 \left(\frac{\partial \eta}{\partial i} \right)_{i \rightarrow 0} \quad (34)$$

Allison

Applying this to the data in Table IV, $\nu = 0.97, 0.95$, and 0.94 at $1, 2$, and 5 atm, respectively. Therefore, $\nu \approx 1$ which is consistent with the R. D. S. being the recombination of two Cl atoms during charge or the dissociation of Cl_2 during discharge. The data of Figure 26 are shown again in Figure 28, but with a theoretical line according to Equation (30) using $i_0 = 0.175$ amp and $\alpha = 0.28$. The agreement with the experimental data is excellent on both the anodic and the cathodic side. It is therefore probable that no concentration polarization is included in the cathodic data. The final best estimates of the exchange current densities obtained by including data from the smaller electrodes gave $i_0 = 0.23, 0.37$, and 0.50 amp/cm 2 at $1, 2$ and 5 atm, respectively. These values when plotted according to Equation (33) gave $\alpha = 0.5$.

Theoretical curves of the activation polarization using these values of the exchange current density (i_0) are shown in Figure 29. However, since the variation with potential of the coverage θ is not known, the plots could not be made according to Equation (29) but were made according to Equation (30) using $\alpha = 0.3$. This was found to give good agreement with the experimental data. See Figures 26 and 28.

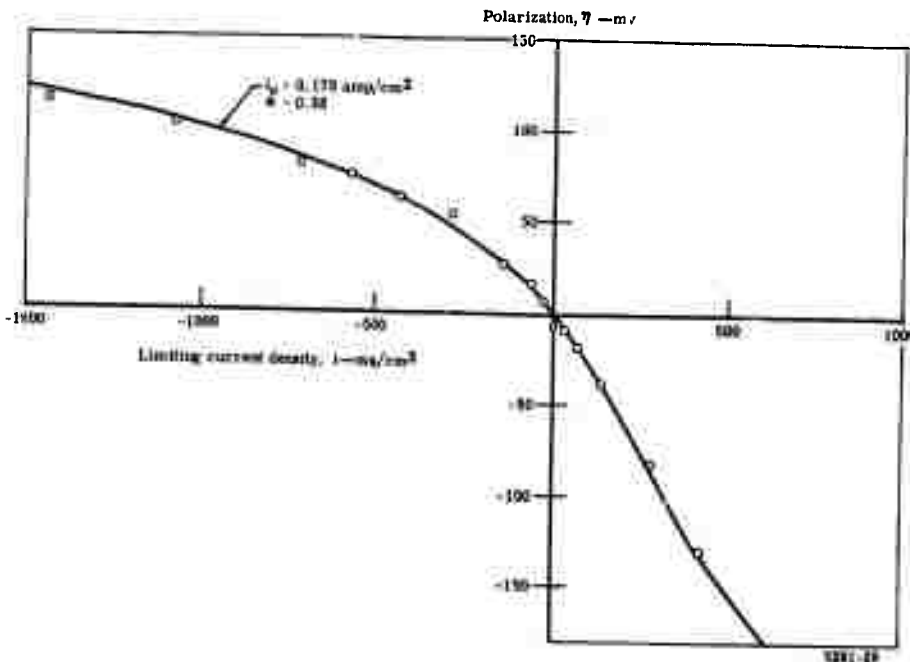


Figure 28. Polarization data for Poco-AX at 1 atm.

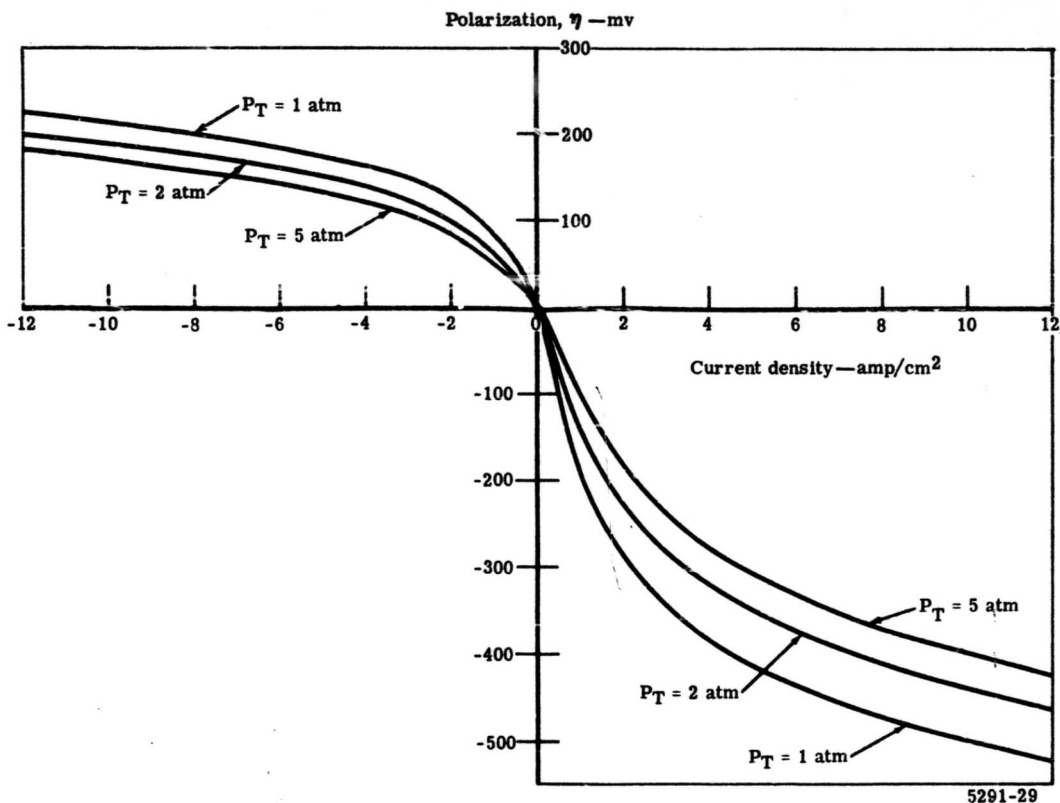


Figure 29. Activation polarization versus current density for Poco-AX.

The polarizations predicted on the cathodic side ($\text{Cl}_2 + 2 e^- \rightarrow 2 \text{Cl}^-$) appear quite high. However, it should be remembered that these are obtained mainly by extrapolation from the anodic reaction and hence refer to the same real area. However, on discharge the real area of contact per geometrical cm^2 is no doubt larger than on charge due to the ΔP developed across the electrode and hence the real current density will be considerably less than the current density per geometric cm^2 .

No attempt has been made to date to determine the ratio of real to geometric electrode area under various conditions. An assumed ratio of 5 was used in the limiting current density calculations and this gave excellent agreement with experimental data for the 1/8-in. thick electrode. However, this ratio will no doubt change with electrode thickness, Cl_2 pressure and purity and with current density. Therefore, it is not yet possible to predict the activation polarization of an operating cell with much certainty. However, the values shown in Figure 29 probably represent an upper limit.

Allison

SECTION IV

LABORATORY HIGH POWER DENSITY CELL

OBJECTIVES

The main objective of Task 2 was to demonstrate that a high level of performance, in terms of power-to-electrode area ratio, could be achieved in a Li-Cl₂ cell. A ratio of 20 w/cm² was set as a contractual goal. This power level was to be held for at least 20 min.

Other objectives were to establish the basic approaches to high power density electrode design and to determine the performance characteristics of these electrodes for their subsequent use in cell and systems design studies.

BASIC DESIGN CONSIDERATIONS

To achieve the desired power density, the following were apparent.

- Electrode spacing would have to be as close as permitted by considerations of reliability, simplicity, and cost.
- A "flow by" Cl₂ electrode would be required because close spaced electrodes would not permit "bubble through" operation.
- Thickness of the Cl₂ electrode should be small enough to permit the required diffusion rate of Cl₂ to the reaction site, while also permitting back diffusion and escape of gaseous impurities.
- Electrical resistance losses in the electrodes must be kept small. Therefore, in the case of the chlorine electrode, a simple thin disk would not suffice.
- A path for rejection of heat from the reaction zone would be required in order to prevent boiling of LiCl or Li, or melting of the Li electrode metal structure.

For the test results to effectively represent actual electrode performance, the electrode currents would have to be large relative to stray currents anticipated from edge effects to minimize the significance of edge effects contribution to cell performance. Also, the electrode area would have to be well defined, or else a suitable correction for lack of definition would be required.

Since the demonstration cell was only a laboratory device, another design consideration was to design it as a primary or secondary cell. A primary cell would be assembled with a Li charge, while a secondary cell would be charged during initial operation to generate the required Li.

Allison

The considerations favoring the secondary cell approach were as follows.

- Li-Cl₂ cell testing experience at the Allison laboratories was in the secondary field.
- A rechargeable cell could provide a greater discharge time per test and yield more data.
- Cell loading would be simplified because Li handling could be avoided.
- There would be no risk of Li attack on the Cl₂ electrode during heatup as there might be in a primary cell.
- Lithium wetting of a stainless steel electrode had proven to be quickly and reliably established in the electroplating of a charge operation, but experience had proven this to sometimes be difficult in a simple stainless steel to Li contact situation.

Considerations favoring a primary approach were as follows.

- The test results were to be used in projecting the performance of primary cells and primary cell systems. This test project represented an opportunity to develop early technology and experience in the field of primary cells.
- Effective Cl₂ removal during charge from a cell with very closely spaced electrodes would probably be very difficult.

The initial tests (cell No. 1) were with a primary cell design; however, it was decided to combine the advantageous features of each to provide subsequent cells with greater testing flexibility. The later cells were designed with an auxiliary Cl₂ charging electrode so that cell loading only required the handling of LiCl. The discharge electrodes were close spaced as in a primary cell, but the auxiliary electrode allowed recharging of the cell thus permitting additional test data to be obtained from a single buildup and test run.

POWER DENSITY CELL NO. 1

Description

The first test cell was designed as a primary cell having concentric cylindrical electrodes, matrix storage of Li, a thin flow by Cl₂ electrode, and employing wicking of Li to the reaction zone. Cell details and test installation are shown in Figures 30 through 34.

The Cl₂ electrode design was similar to that of cell No. 2 which is shown in detail later in this report.

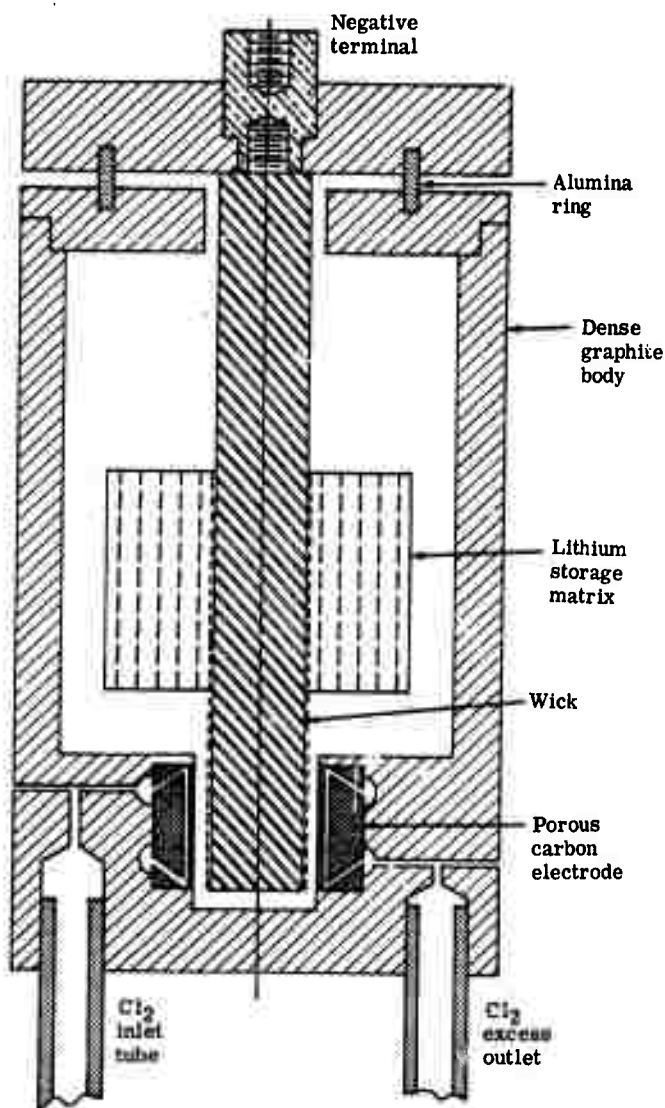


Figure 30. Sketch of test cell No. 1.

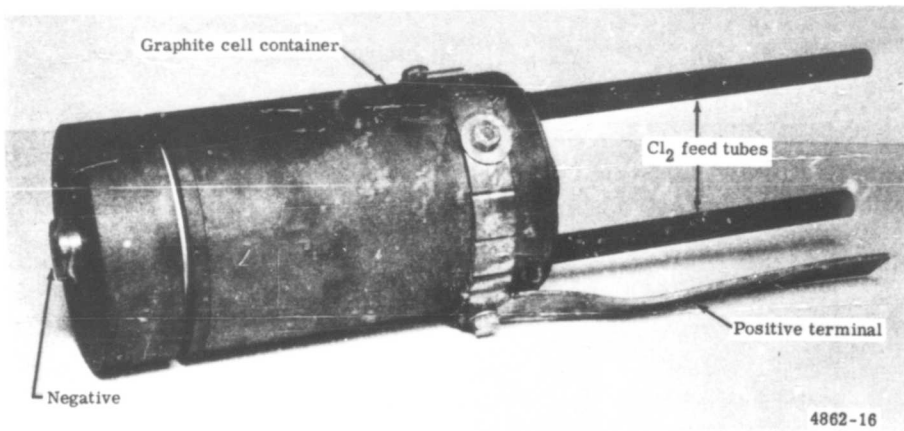


Figure 31. Assembled cylindrical cell.

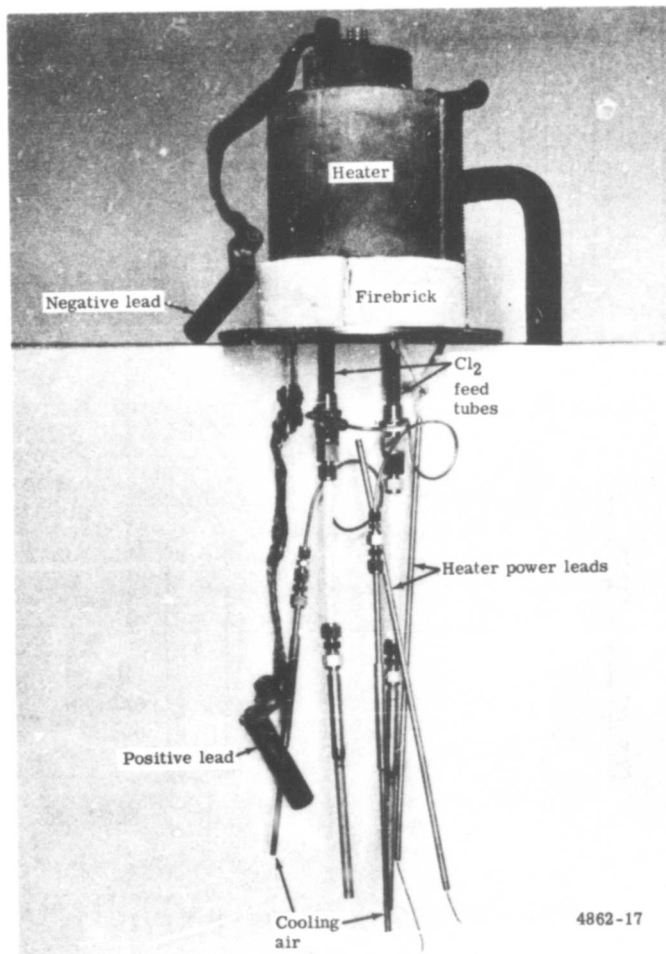


Figure 32. Assembled cylindrical cell shown inside the clam shell heater.

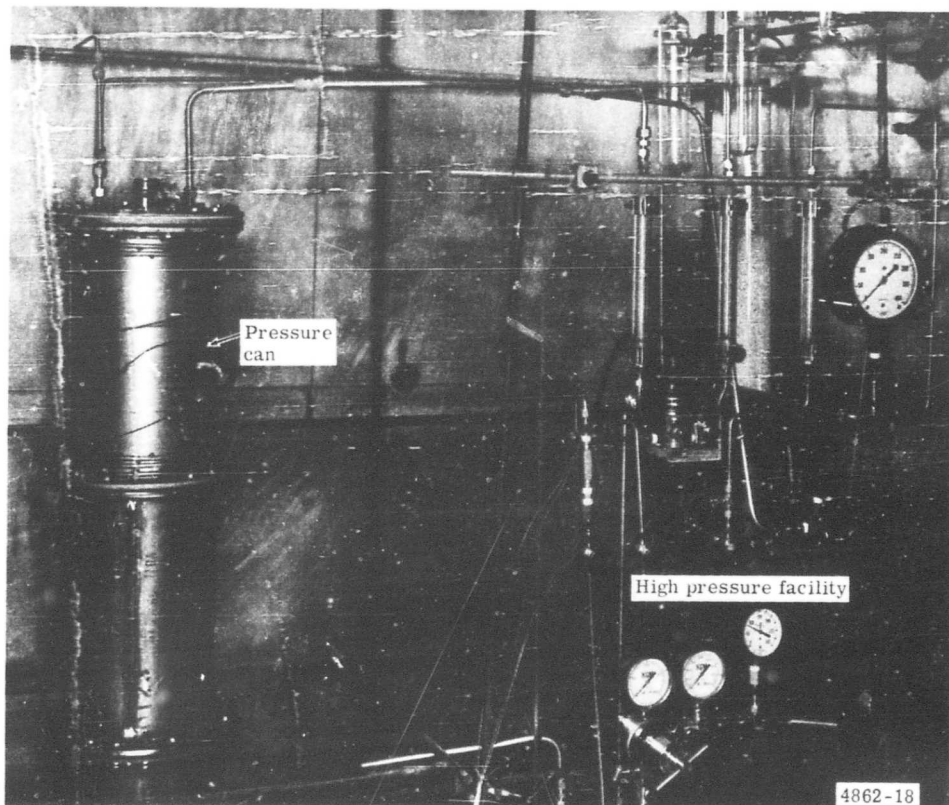


Figure 33. Pressure can, containing cylindrical cell, attached to high pressure gas facility.

Preparation

In preparation of the cell for testing, it was loaded with Li, assembled, loaded with electrolyte, and installed in the test facility. Accomplishing this procedure with minimum exposure to atmospheric contaminants proved more difficult than had been anticipated. Thus, a redesign of the cell was indicated to remedy this problem.

Operation and Test Results

During heat-up at one atmosphere, a short appeared between electrodes as the cell temperature passed the Li melting point. The short disappeared at the LiCl melting point and a small cell voltage appeared. Chlorine flow was then started and the voltage rose very slowly to slightly over 2 v.

The normal open circuit voltage of approximately 3.44 v was never attained. The highest open circuit voltage recorded was approximately 2.4 v. The highest power obtained was 20 w at 2 v and 10 amp. On the $20.5 \text{ cm}^2 \text{ Cl}_2$ electrode, the power density was approximately 1 w/cm².

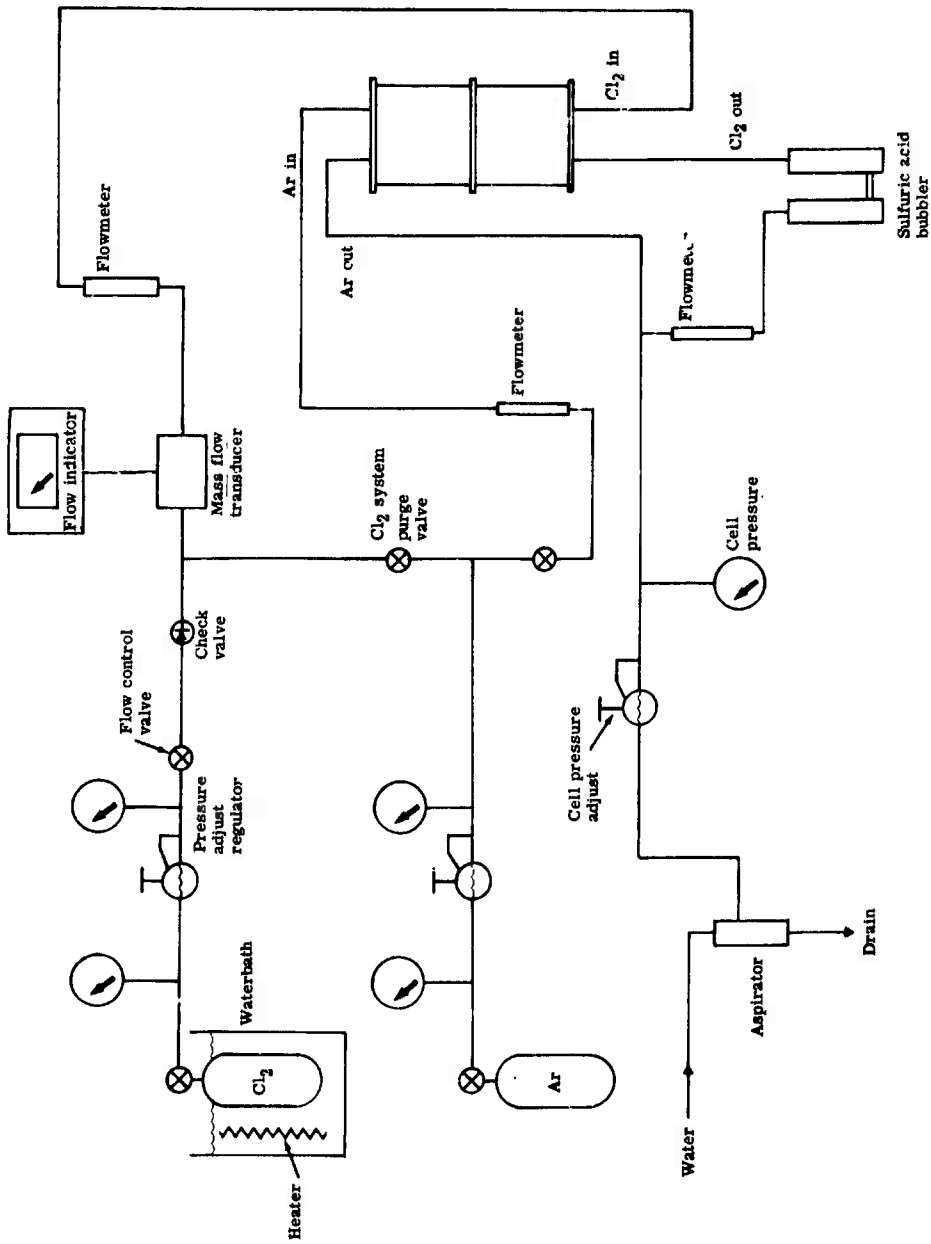


Figure 34. High pressure test facility used with cell No. 1

4882-20

Allison

Resistance checks indicated the low voltage was not caused by a short. Li was not feeding properly to the Li electrode. After a few minutes of operation, another short was indicated and the cell was shut down. The short remained after cooling.

Postoperational Analysis

On disassembly and inspection, it was found that both the Li and the Cl_2 electrodes were badly attacked. This attack apparently began when Li contacted the Cl_2 electrode during heat-up, giving the short indication when the cell temperature was near the melting point of Li.

Lithium attack on the Cl_2 electrode resulted in Cl_2 leakage which attacked the Li electrode. The final short indication was caused by electrode debris. Figure 35 shows the cell after testing. The electrolyte seepage shown is typical of graphite wetting following Cl_2 attack on stainless steel.

POWER DENSITY CELL NO. 2

Description

Cell No. 2 was a new design intended to avoid difficulties encountered by Cell No. 1. See Figures 36, 37, and 38. The more important design changes are presented in the following paragraphs.

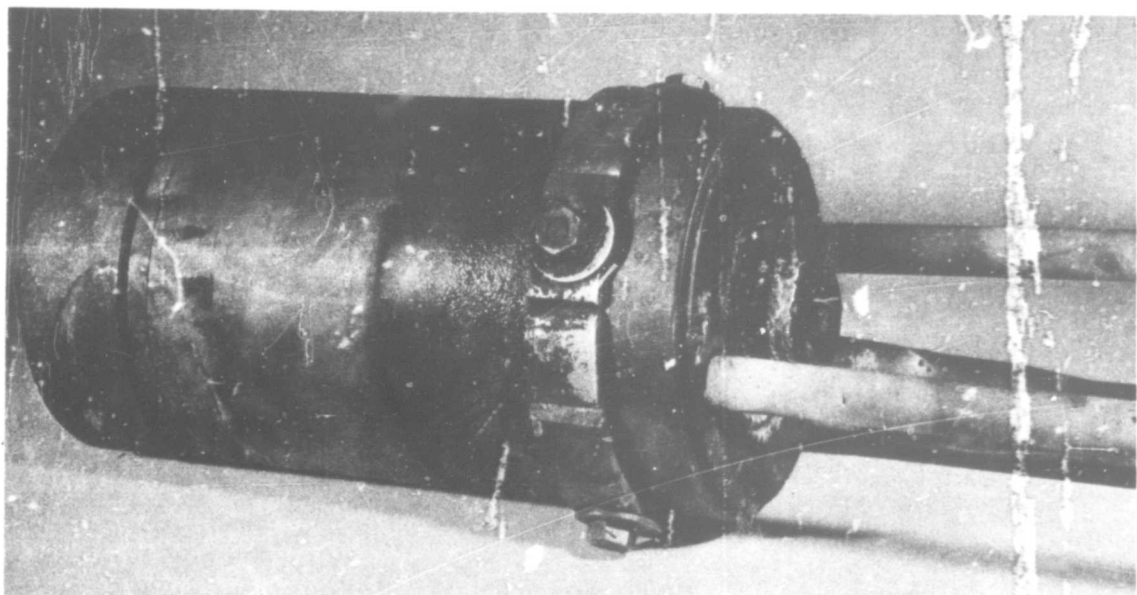


Figure 35. Test cell No. 1 after test.

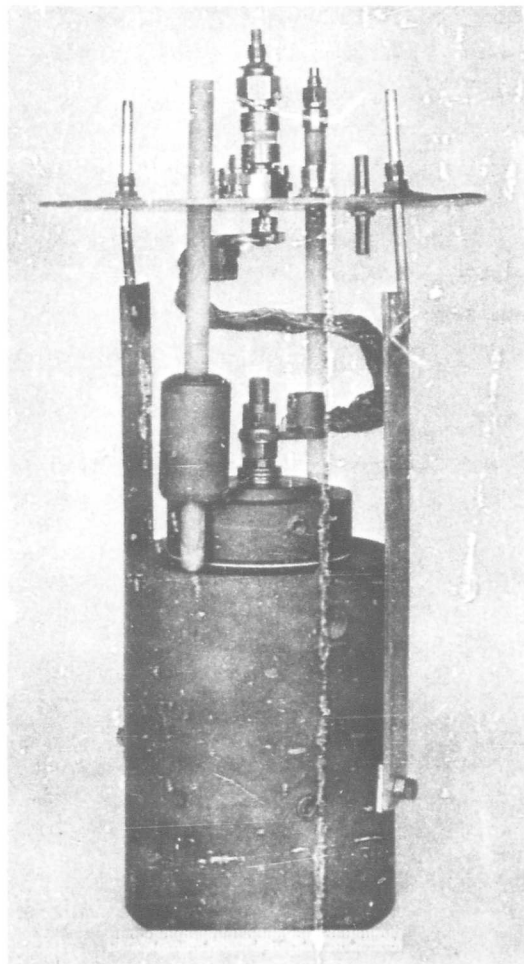


Figure 36. Test cell No. 2.

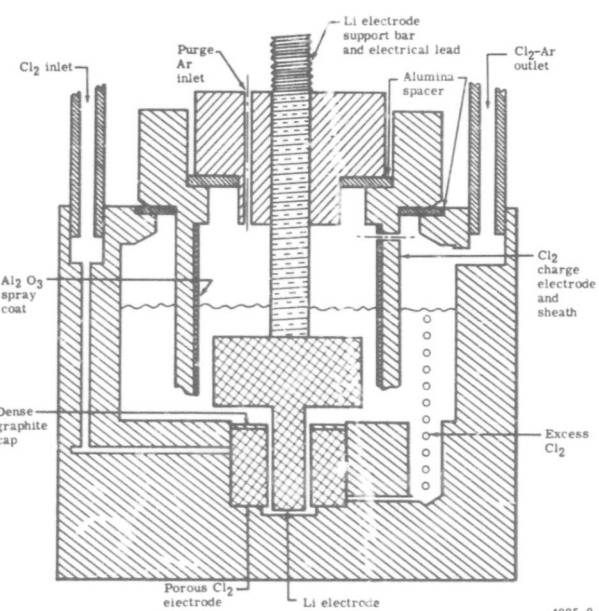


Figure 37. Detailed cutaway of test cell No. 2.

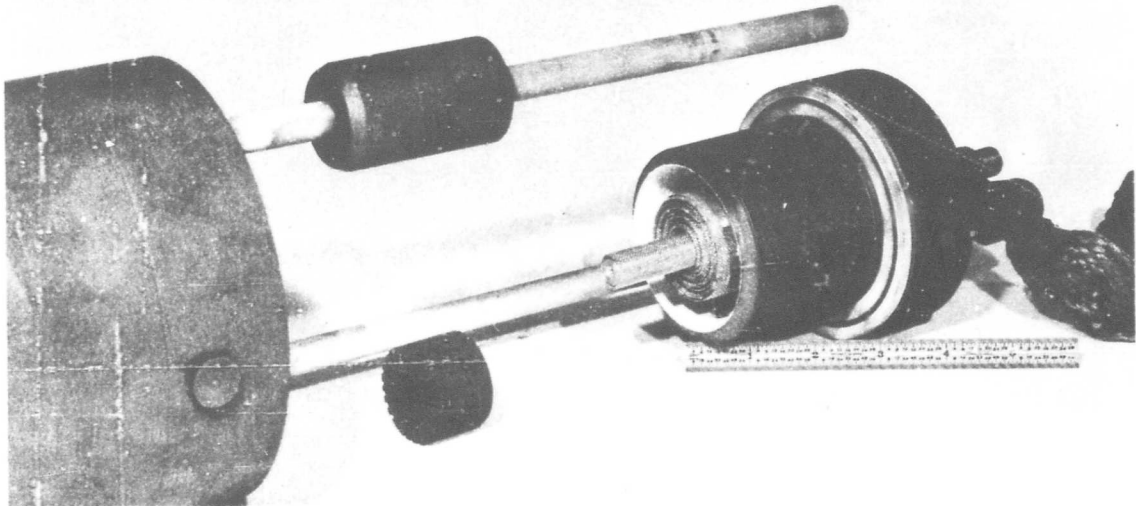


Figure 38. Test cell No. 2.

A second Cl_2 electrode was included for charging. It is basically a flanged short tube of dense graphite having an alumina spray coat on the inner surface. When a suitable potential is applied, chlorine is generated on the outer surface, while Li is generated on the Li electrode. The graphite tube also functions as a sheath around the Li electrode to prevent Cl_2 attack on the Li and the electrode structure. This design eliminates the need for loading Li into the cell and permits more than one discharge to be made by virtue of being rechargeable.

All tubes, leads, and cell supports were attached to the pressure vessel top cover to simplify the procedure of cell buildup and insertion into the can.

The excess Cl_2 flow path was changed so that the excess would bubble into the electrolyte near the cell bottom at a point between the charge electrode and the cell wall. This eliminates the need for delicate external control of the pressure differential across the Cl_2 electrode. This differential must be maintained between the pressure limits associated with flooding at one extreme and bubble-through at the other. Flooding is still possible with this arrangement, but recovery is automatic when adequate Cl_2 flow is resumed.

Another advantage of bubbling the excess Cl_2 into the electrolyte is that bubble formation and detachment causes pressure fluctuations in the Cl_2 feed system. These fluctuations visibly disturb the rotameter ball and have, in practice, permitted adjustment of the excess flow to near minimum values without reference to cell voltage decline.

Allison

The Cl_2 electrode area was reduced to 12.6 cm^2 to reduce the current magnitudes, heating effects, and Li storage requirements. The Cl_2 electrode drawing is shown in Figure 39. Electrode spacing was 1 mm.

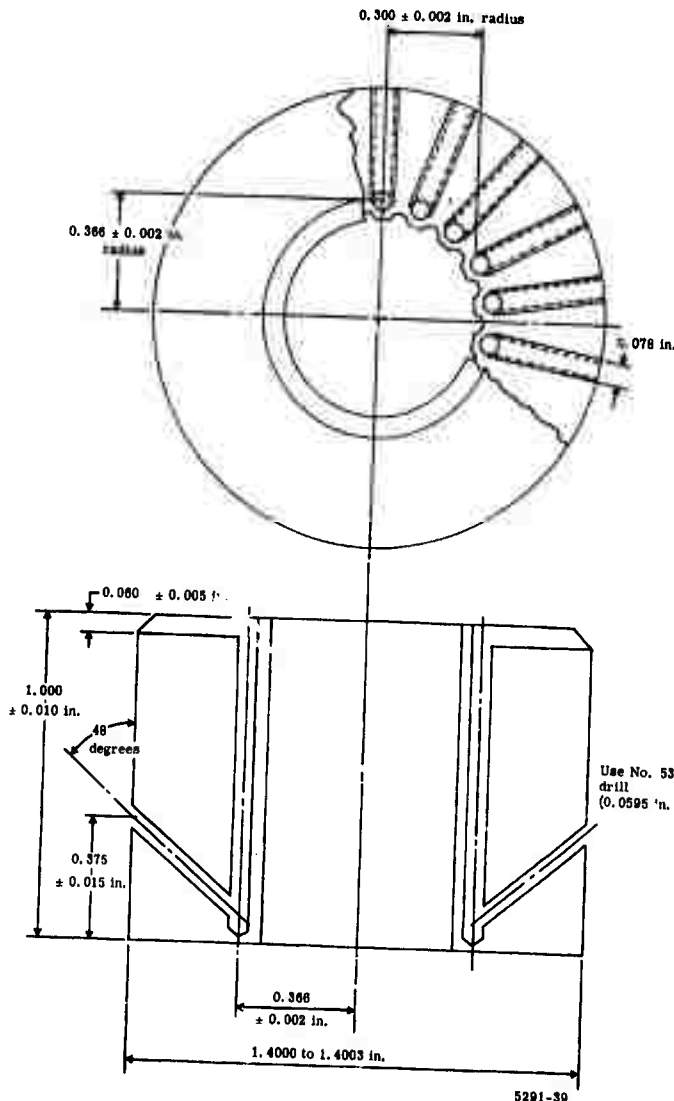


Figure 39. Details of chlorine electrode.

Allison

Test Facility Rework

The plumbing of the pressure test facility was modified to accommodate the new cell design and to provide automatic recording of Cl_2 flow rates and cell pressure. A schematic of the system is shown in Figure 40.

Preparation

The cell was assembled in an inert atmosphere and filled with crushed electrolyte. It was then removed from the inert atmosphere and installed in the pressure can.

Operation and Test Results

During heat-up and charge, argon flow was maintained through the Cl_2 electrode. The test pressure was one atmosphere.

After completion of the charge, chlorine flow was started and a normal open circuit voltage of 3.46 v appeared. Discharge was then started and the loading was increased in steps. The step with the longest duration was about two minutes at 2.67 v and 88 amp. The next longest step was 2.53 v at 96 amp. Power density at this point was about 19.3 w/cm^2 .

A power supply failure interfered for a time with further discharge attempts. When the failure was corrected, it was found that the cell would not discharge well and indicated Li depletion. A recharge was attempted but was unsuccessful and the cell was shut down.

Postoperational Analysis

Teardown inspection indicated that the excess Cl_2 had not been confined entirely to the annulus between the charge electrode and the cell wall. Some of the Cl_2 had bubbled under the charge electrode-sheath and into the Li electrode region where it consumed the Li and nearly severed the electrode support bar above the electrolyte level. The Cl_2 electrode appeared to be in excellent condition after washing in deionized water and was left in the cell body for buildup into cell No. 3.

POWER DENSITY CELL NO. 3

Description

Cell No. 3 was a modified version of cell No. 2. See Figures 41 and 42. The modifications consisted of the following:

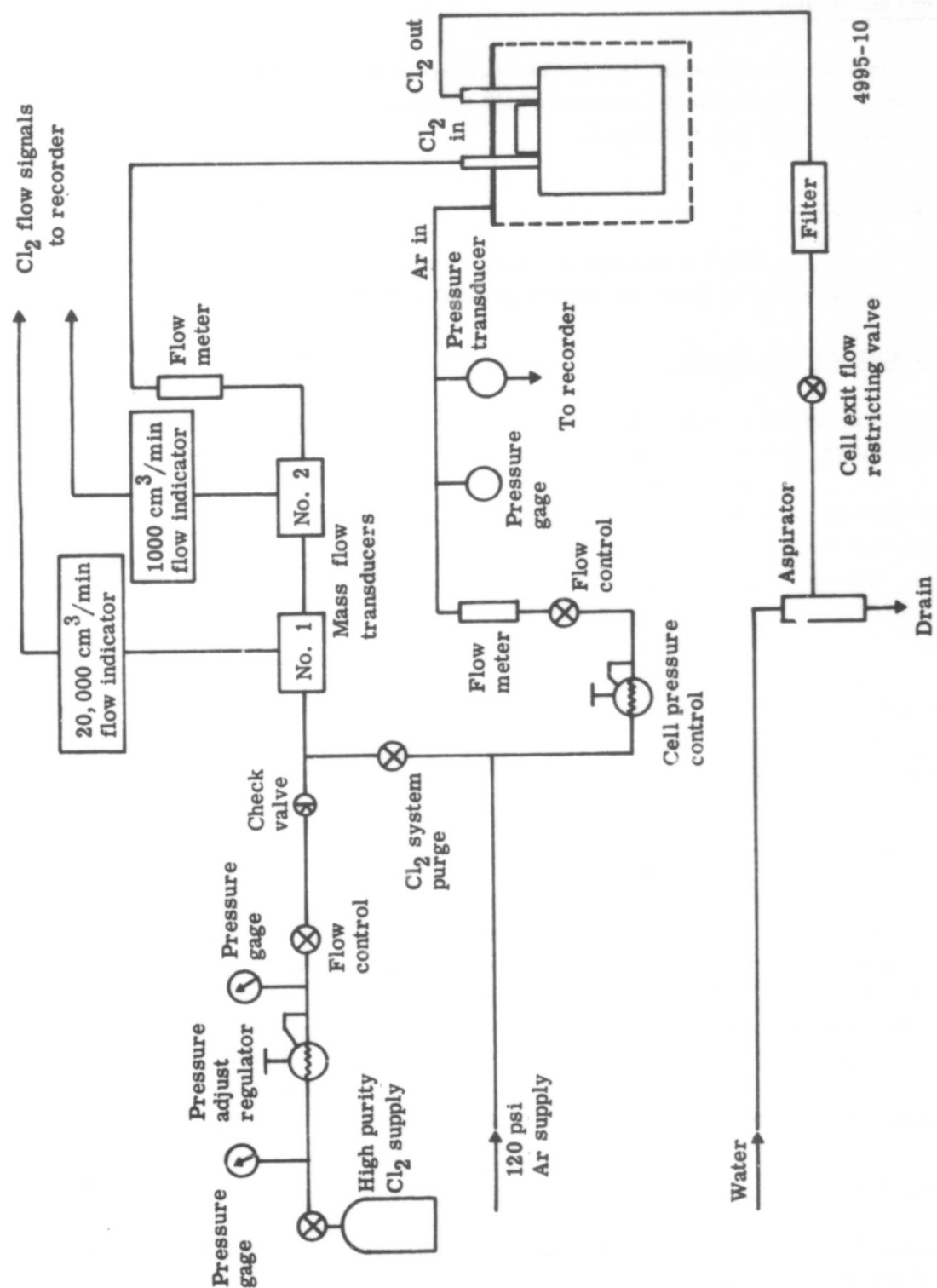


Figure 40. Schematic of modified pressure test facility.

- A longer Cl₂ sheath (charging electrode) to reduce the rate of Cl₂ entry into the Li electrode region
- A BeO tube sheath around the Li electrode support bar to reduce the Cl₂ attack rate
- A heavier charging electrode and cell top to better maintain electrode spacing against external forces of leads and installation pressures

Operation and Test Results

After preparation, as with cell No. 2, the cell was installed into the pressure can, pressurized to approximately 3 atm, and charged to approximately 70 amp-hr input. A discharge was then initiated in an effort to produce 20 w/cm² for 20 min. Voltage, current, power, and power density data are presented in Figure 43.

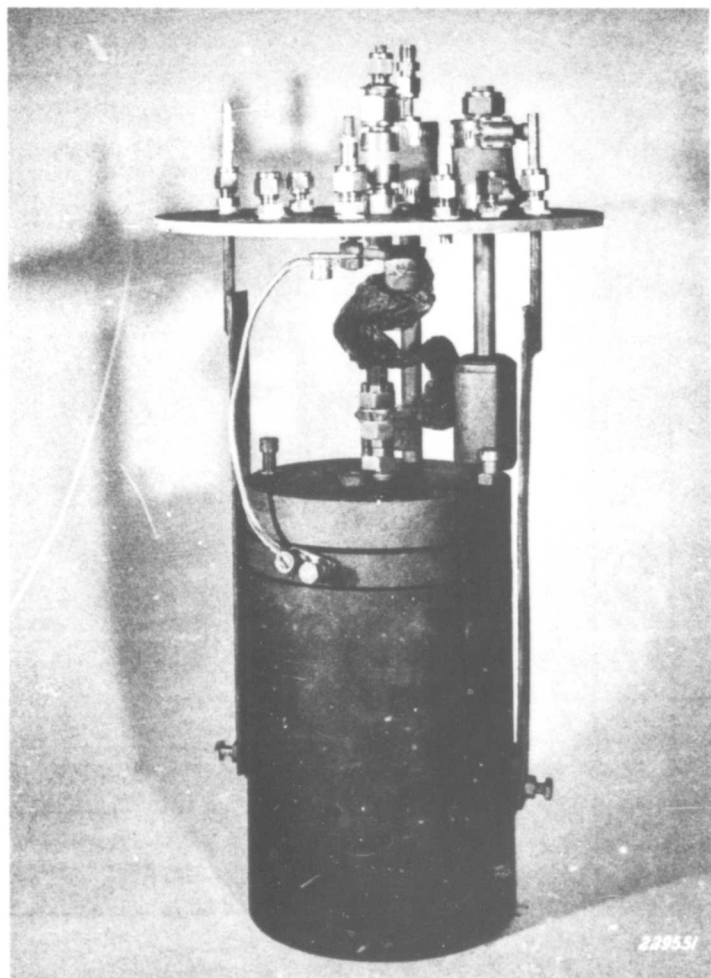


Figure 41. Test cell No. 3.

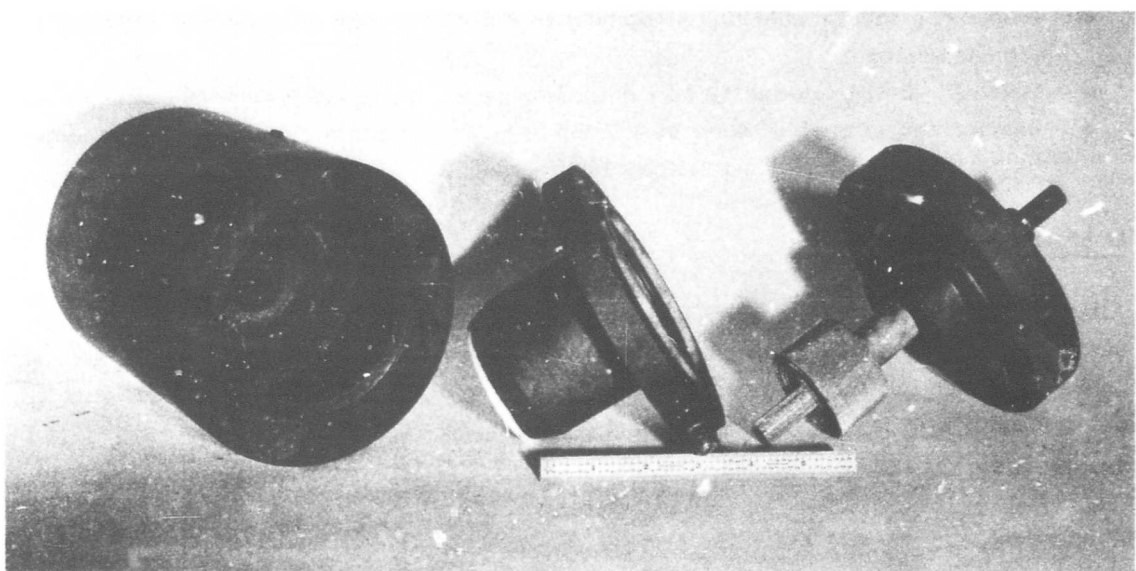


Figure 42. Test cell No. 3 components.

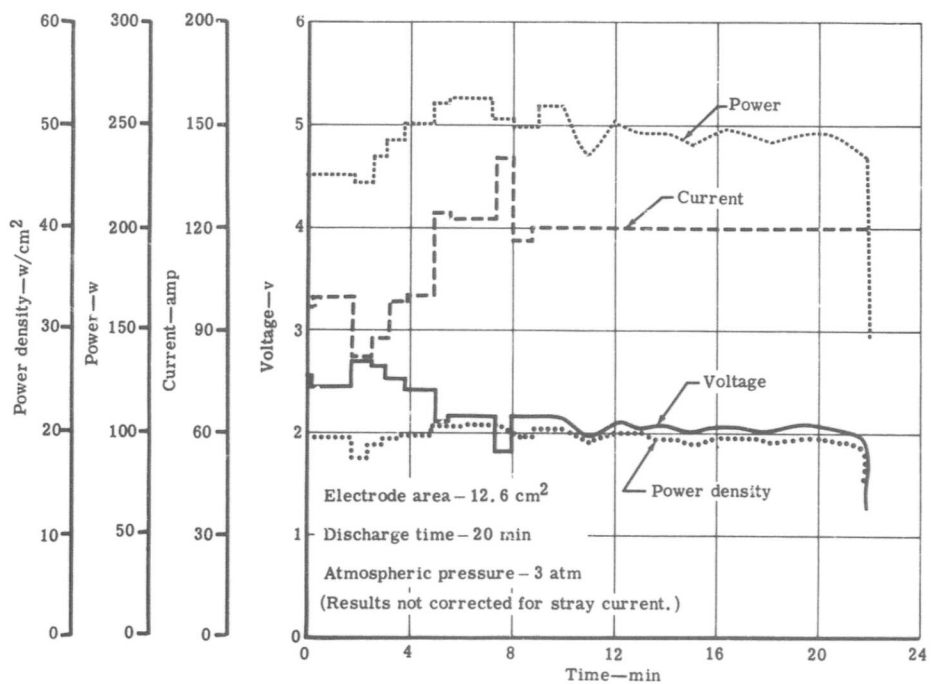


Figure 43. Twenty-minute discharge test results for test cell No. 3.

Allison

Step changes in the current were made during the first 9 min of the run. These changes were made for the purpose of obtaining cell performance data and finding the best degree of loading for maximum power output. After 9 min, the discharge was held constant at 120 amp.

The apparent power density averaged over 19 w/cm^2 . Total discharge was about 42 amp-hr, yielding an overall coulombic efficiency of approximately 60%.

A recharge was started for a second cycle and a recheck of equipment calibration was made. During this check, the leads were disconnected from the shunt in the discharge control circuit by error. The discharge current density immediately increased to over 30 amp/cm^2 for a period of about 1.5 sec. The cell voltage fell to near zero and efforts to revive it were ineffective.

Postoperational Analysis

On teardown, it was found that the Cl_2 electrode surface had ruptured in two places. This was probably the result of Li attack and/or rapid thermal transients. Both could have occurred during the period of excessive discharge current.

POWER DENSITY CELL NO. 4

Description

Cell No. 4 was rebuilt from cell No. 3 by replacing both the Li and Cl_2 electrodes. Electrode spacing was 0.06 cm.

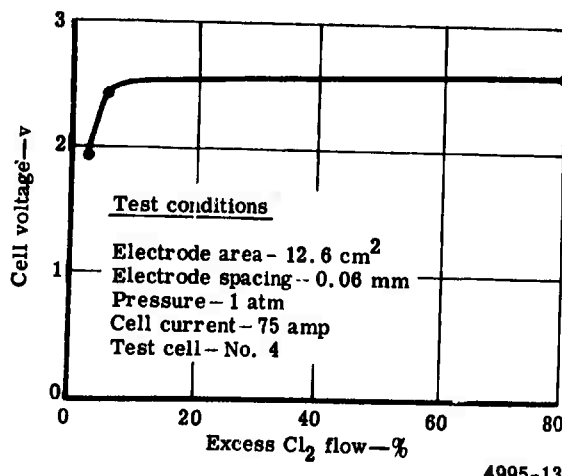
Operation and Test Results

The test pressure was one atmosphere. The test objective was to obtain Cl_2 flow rate data including minimum flow requirements, voltage versus excess Cl_2 flow, and self-discharge rate.

The cell ran two cycles before failure with a total discharge time of 2.5 hr. The self-discharge rate of the cell obtained from the open circuit Cl_2 consumption rate was determined at approximately 0.6 amp/cm^2 .

The effect of Cl_2 flow variation at a constant current of 75 amp is presented in Figure 44. It should be noted that there are only three data points indicated in Figure 44. The shape of the curve, therefore, can be considered as only approximating the true cell behavior.

Figure 44. Effect of Cl_2 flow on cell voltage.



4995-13

It was noted during cell operation that there is always some noticeable change in cell voltage with any great increase in excess flow, even between 200 and 300%. However, this is considered a result of stray current increase as the electrolyte is stirred by the Cl_2 .

The minimum Cl_2 flow rate versus current shown in Figure 45 is based on a calibration of the Hastings mass flowmeters by reference to a timed soap-bubble flowmeter. The calibration was corrected for temperature, barometric pressure, and partial pressure of water, but not the possible Cl_2 reaction with the soap. It is possible, therefore, that another correction factor is needed.

Postoperational Analysis

Failure of cell No. 4 was caused by the rupture of the Cl_2 electrode. Total discharge time was approximately 2.5 hr. Cl_2 starvation occurred many times in the course of determining minimum flow rate requirements. During these periods of starvation, lithium attack and thermal transients presumably occurred at the Cl_2 electrode causing eventual failure.

POWER DENSITY CELL NO. 5

Description

Power density cell No. 5 (Figures 46 and 47) was modified to improve the Cl_2 containment in the outer annulus and to increase the storage matrix volume by extending and enlarging the charge electrode/sheath.

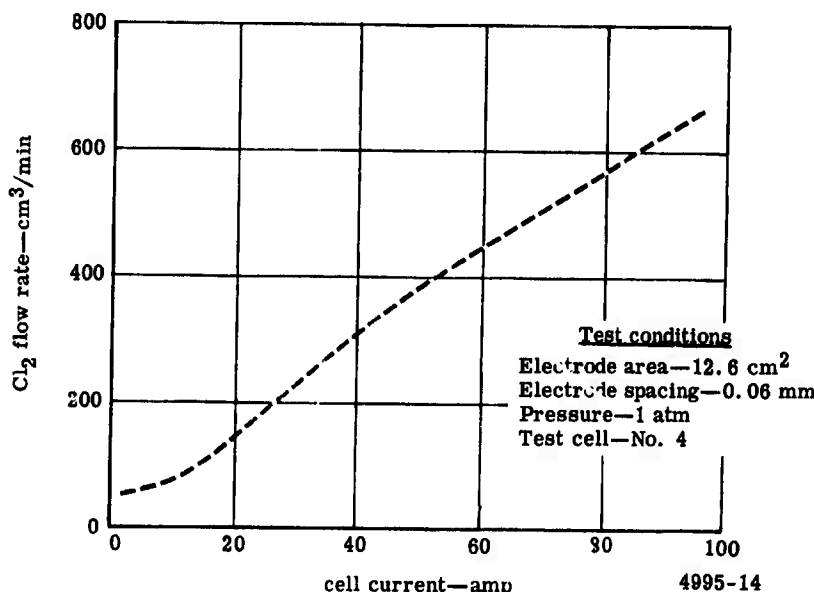


Figure 45. Minimum Cl₂ flow rate versus cell current.

The Cl₂ electrode was made more easily replaceable by including it in a replaceable graphite cup assembly. Electrode spacing was 1 mm.

Operation and Test Results

A charging power supply malfunction caused failure of the cell before any meaningful discharge data could be obtained.

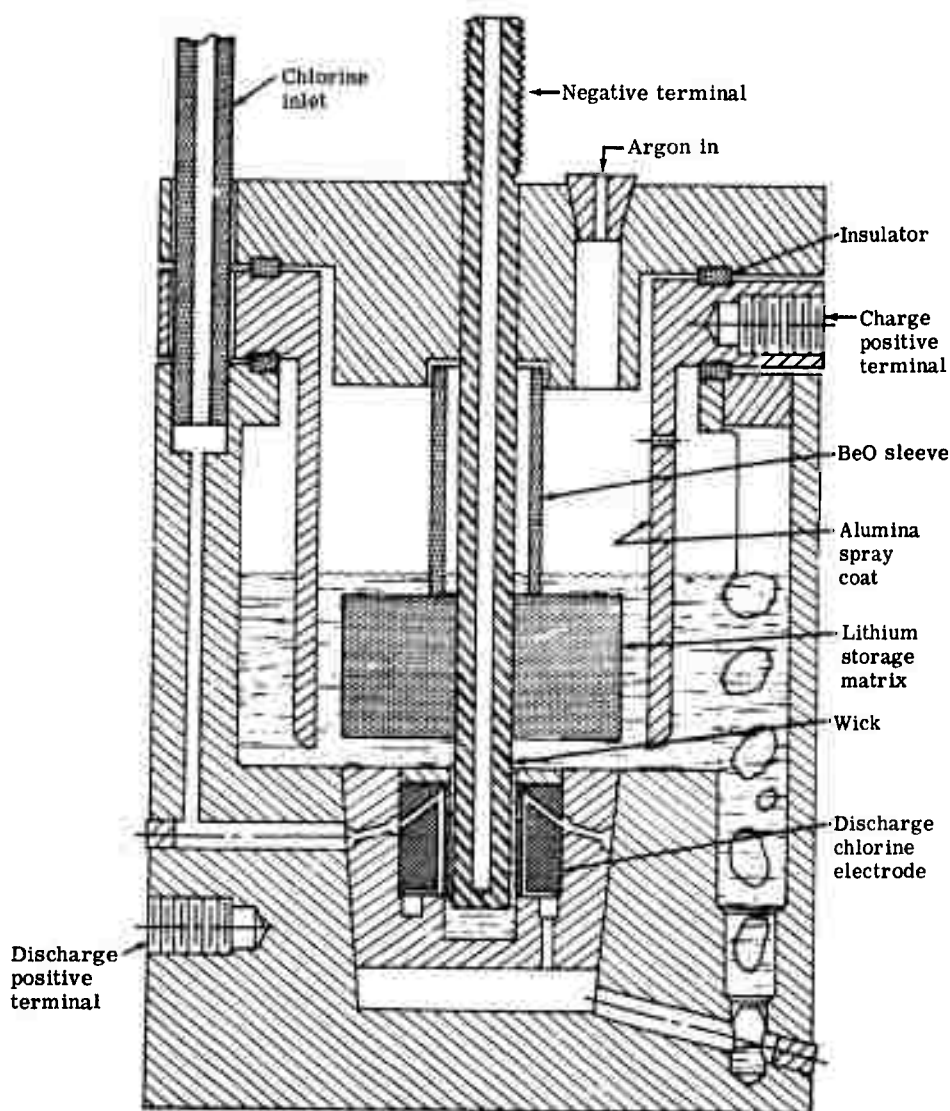
POWER DENSITY CELL NO. 6

Description

Power density cell No. 6 was identical to cell No. 5.

Operation and Test Results

This cell ran successfully for approximately 30 hr. Performance at 1.5 and 3 atm is shown in Figures 48, 49, and 50.



5291-46

Figure 46. Power density cell No. 5.

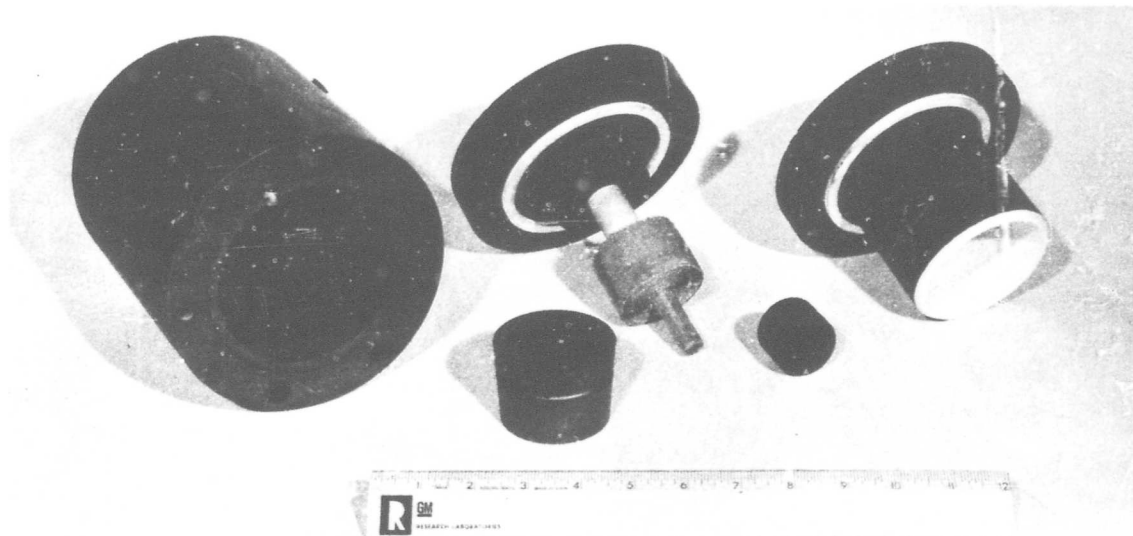


Figure 47. Test cell No. 5.

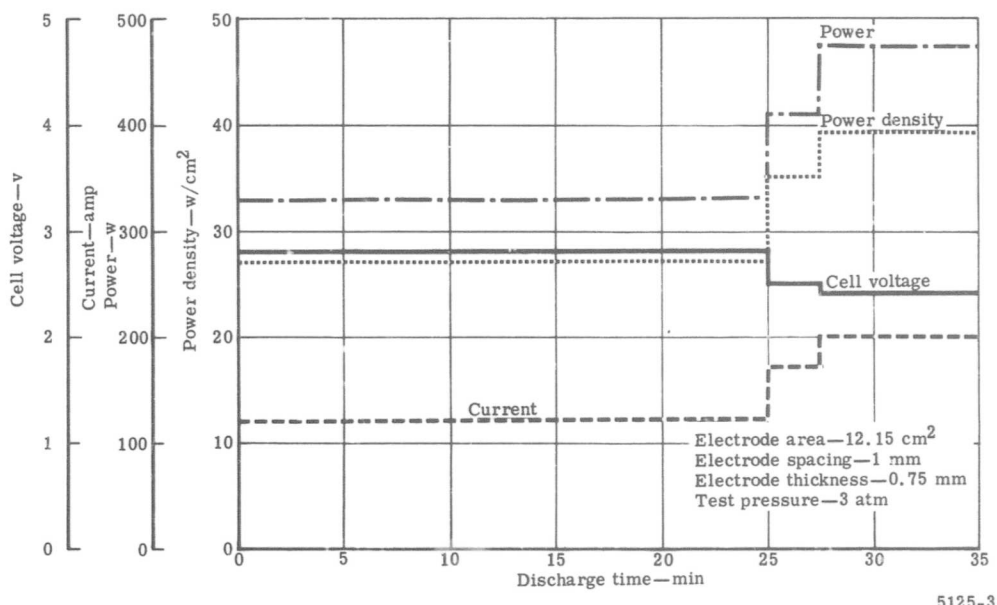
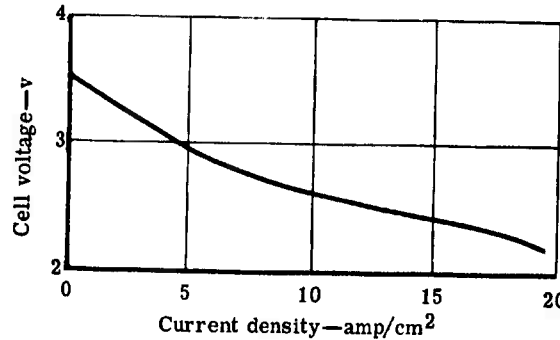
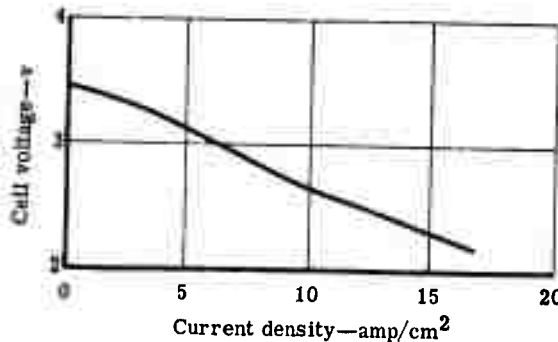


Figure 48. High power density discharge for power density cell No. 6.



5291-49

Figure 49. Voltage-current density plot at 3 atm for cell No. 6.



5291-50

Figure 50. Voltage-current density plot at 1.5 atm for cell No. 6.

Allison

Figure 48 indicates the performance obtained during a 34-min discharge at 3 atm. This performance was well in excess of the goal of a 20-min discharge at a power density of 20 w/cm^2 . The data presented herein were corrected for stray current where applicable. Chlorine excess flow rate was approximately 20% for the first 25 min and 40 to 50% thereafter.

A comparison of Figures 49 and 50 shows an improvement of only 5% cell power or less as a result of doubling the pressure at currents up to 200 amp (16 amp/cm^2). The highest power density shown at 3 atm is 41 w/cm^2 .

A plug developed in the cell vent tube during the test. After pressurizing the cell to 3.7 atm, it suddenly blew clear causing a perturbation in cell pressure. The cell voltage immediately fell to a low value and good performance could not be regained. The cell was then shut down.

Postoperational Analysis

Frozen LiCl was found in the Cl_2 inlet tube and the Cl_2 electrode pores. Operation of the Cl_2 electrode was impaired after a cell pressure surge occurred while discharging at 270 amp. The surge had forced LiCl into the Cl_2 gas channels.

POWER DENSITY CELL NO. 7

Description

Power density cell No. 7 was identical to cell No. 6 except that it included a probe to detect voltages at the back side of the Cl_2 electrode. Another voltage detector, at the center of the Li electrode in the region of the reaction zone, was also installed by drilling a hole to near the bottom of the molybdenum rod. A sheathed thermocouple was installed making electrical contact between the sheath and the rod at the bottom of the hole. The thermocouple served both as a voltage and temperature sensor for the Li electrode.

Operation and Test Results

At the beginning of the first discharge, low output, as in a high resistance cell, was indicated. Its response to pressurizing also was unusual. Within a period of 20 min, pressurization to 3 atm was accomplished and the apparent resistance became normal. This apparent resistance change during the first discharge is shown in Figure 51.

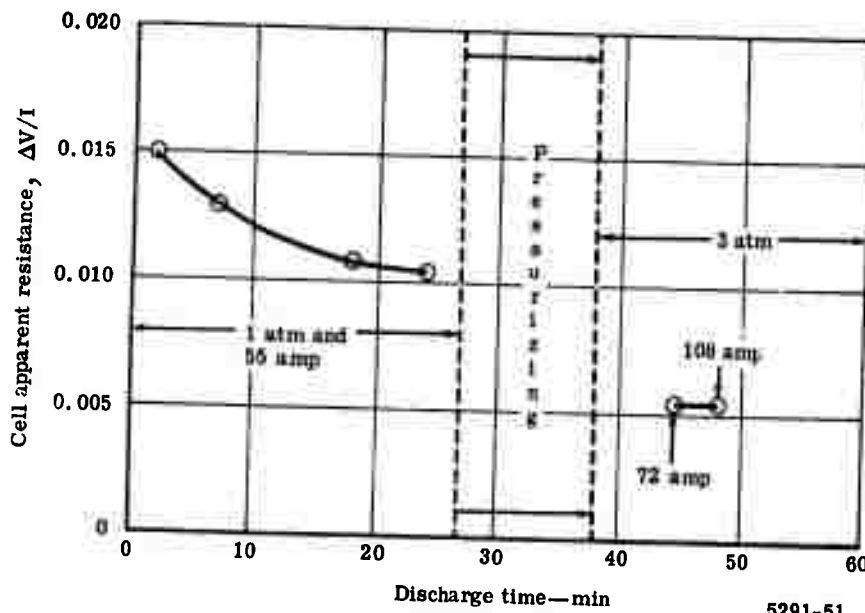


Figure 51. Apparent resistance versus time for the first discharge of power density cell No. 7.

The second discharge performance (Figure 52) was normal. The maximum power density reached was 43 w/cm^2 and the Li electrode temperature at the thermocouple reached 935°C (1715°F). Discharge was terminated because of voltage decline indicating probable Li depletion.

Succeeding discharges were aimed at obtaining Cl_2 flow requirement data; however, cell performance had deteriorated badly. The output was low and the Li electrode temperature rose quickly to high levels when normal discharge Cl_2 input rates were established.

Postoperational Analysis

The cell was not disassembled; however, it is probable that the Cl_2 electrode ruptured during cooling after the second discharge. Figure 52 indicates that less than one minute after discharge termination, the open circuit voltage dropped suddenly and remained low for a period of more than 7 min. This drop could have resulted from a piece of graphite from the Cl_2 electrode surface bridging the electrode gap. The temperature response to the Cl_2 input probably resulted from direct combination of Li with the Cl_2 escaping from the ruptured electrode.

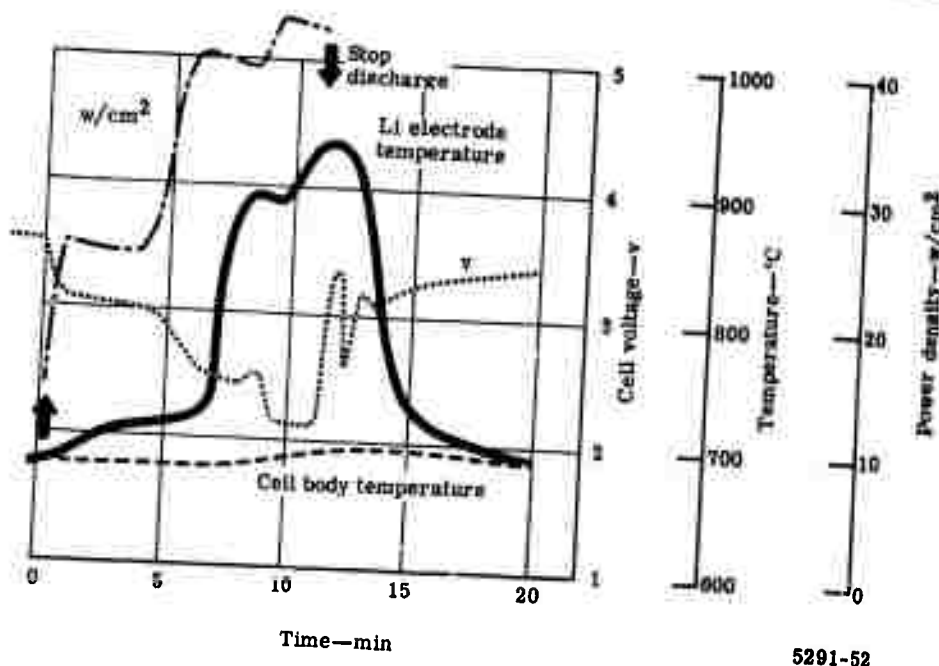


Figure 52. Discharge performance curve illustrating 43 w/cm^2 .

POWER DENSITY CELL NO. 8

Description

Cell No. 8 differed from cell No. 7 only in that the Cl_2 excess was piped out of the cell through an alumina tube inserted tightly into the excess flow discharge opening in the cell bottom. The purpose of the change was to permit direct measurement of excess chlorine flow rates.

Operation and Test Results

The cell operated near normal power output, but the excess Cl_2 flow rate requirement was extremely high. Approximately 15 times normal flow was required to hold 35 w/cm^2 at 3 atm.

Allison

Postoperational Analysis

On disassembly, the Cl_2 electrode was damaged during cell buildup. It appeared that the high Cl_2 rate requirement was due to partial blockage of some of the Cl_2 flow channels by particles resulting from the damage during assembly.

POWER DENSITY CELL NO. 9

Description

Cell No. 9 was a second attempt at direct measurement of excess chlorine flow rate. It was similar to cell No. 8.

Operation and Test Results

Chlorine electrode flooding caused cell failure soon after heat-up was completed. Electrolyte passed through the Cl_2 electrode and out the excess flow exit tube where it froze, preventing further cell operation.

The flooding was caused by partial plugging of the Ar exit line which resulted in an electrolyte-to- Cl_2 pressure differential of approximately 5 psi for approximately 20 sec.

POWER DENSITY CELL NO. 10

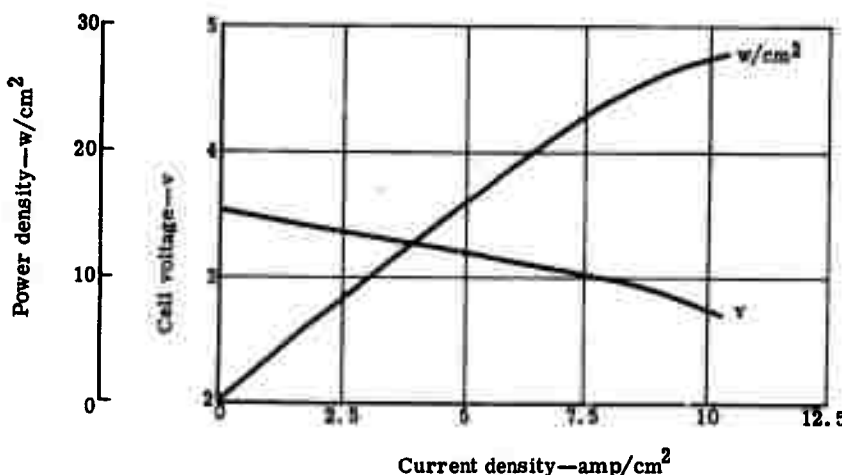
Description

Cell No. 10 was built to test the performance of a thicker (approximately 1.5 mm) electrode. Except for the thicker electrode, it was identical to cells No. 5 and No. 6 with 1-mm electrode spacing and an electrode area of 12.15 cm^2 .

Operation and Test Results

Gas exit tube plugging was encountered early in the test and on three occasions the plugs blew clear and emitted slugs of hot liquid electrolyte while operating at room temperature.

Despite the plugging problem, some successful operation at 3 atm was completed. The highest power yet obtained for operating potentials above 3 v was recorded. Over 20 w/cm² was indicated at 3 v. The cell performance quickly declined while a current-voltage curve was being plotted so that the thick electrode performance at 3 atm was not fully characterized. The portion of the current-voltage plot completed is shown in Figure 53.



5291-53

Figure 53. Discharge of high power density cell No. 10 at 3 atm.

Postoperational Analysis

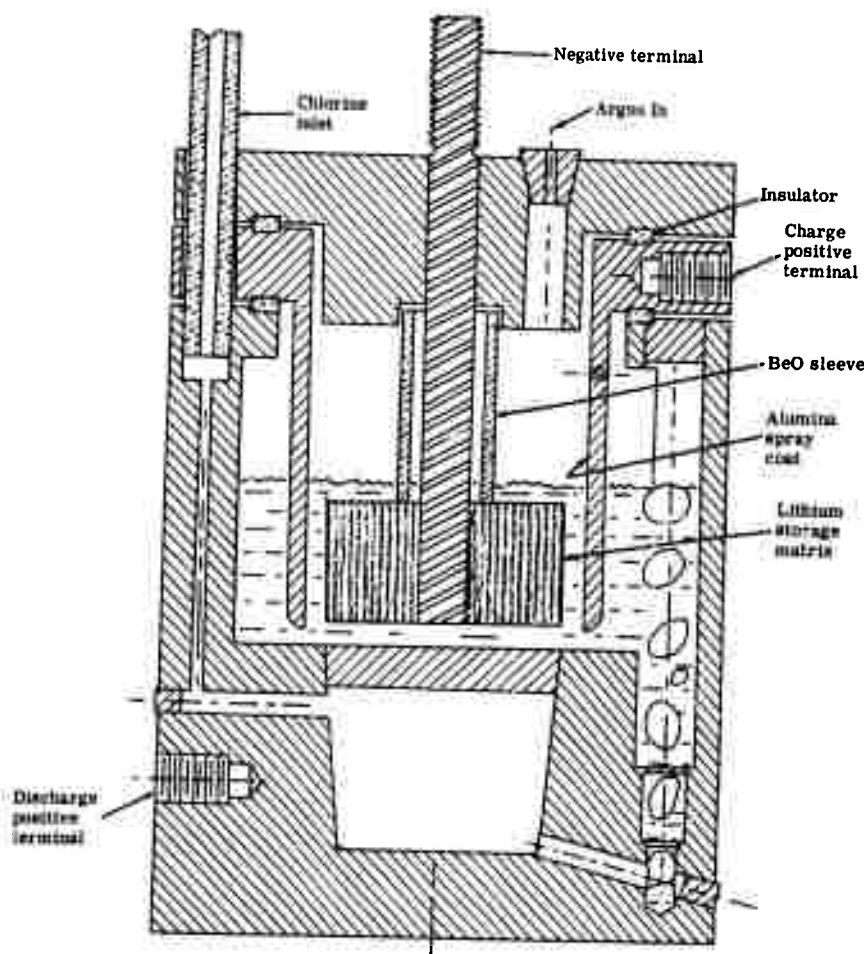
Although far more charge had been put into the cell than was removed by discharge, there was no Li present in the matrix at teardown. The electrolyte level was found to be low (because of that lost through the vent) and a dark scum was found to have been floating in the outer annulus.

The origin of the scum has not been determined. The argon purging hole in the sheath probably became plugged, causing pressure differentials which resulted in the electrolyte losses.

The absence of Li in the matrix on teardown was probably due to the low electrolyte level which allowed Cl_2 to reach the matrix and react chemically.

STRAY CURRENT CELL

The correction to indicated performance to compensate for the "lack of definition" of electrode area was determined in a "stray current cell." This cell, shown in Figure 54, was basically a reworked high power density cell from which the power density test electrodes had been removed.



5291-54

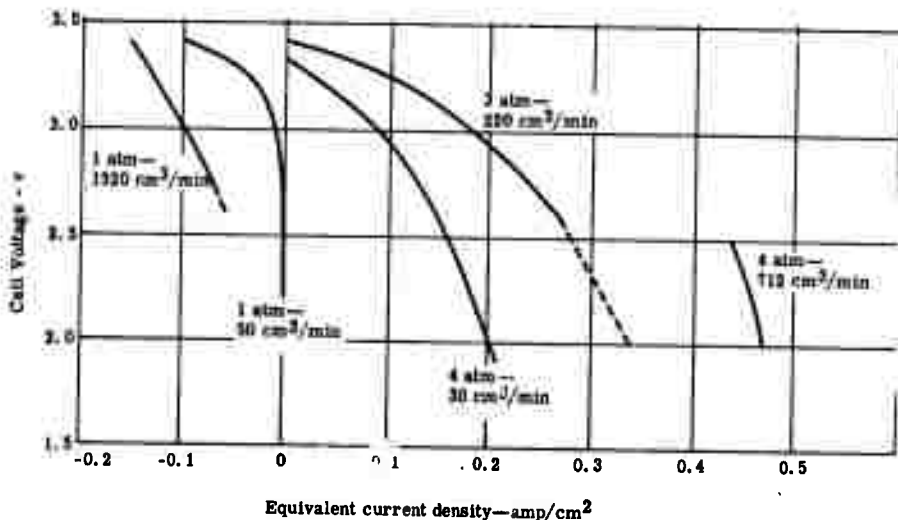
Figure 54. Stray current cell cutaway.

Allison

This cell was operated similar to the normal power density test cell. The currents produced by this stray current cell were assumed to be approximately the same as the currents produced between the storage matrix and cell body in a power density cell. The indicated performance of the power density cell then was corrected by subtracting the stray current cell performance before dividing the output power by the electrode area to obtain the cell power density.

Three stray current cells were tested and the combined performance data is shown in Figure 55. Stray current is a function of both voltage and pressure. The pressure effect is due to Cl_2 solubility.

At low pressures, dissolved Li reaches the cell wall faster than Cl_2 . As a result, the cell loses current internally in plating this Li back onto the Li electrode. At higher pressures, the dissolved Cl_2 consumes the dissolved Li and also is adsorbed on the cell wall where it can produce additional power in the discharge. Stray current then can be in either direction and is usually less than 1% of cell output.



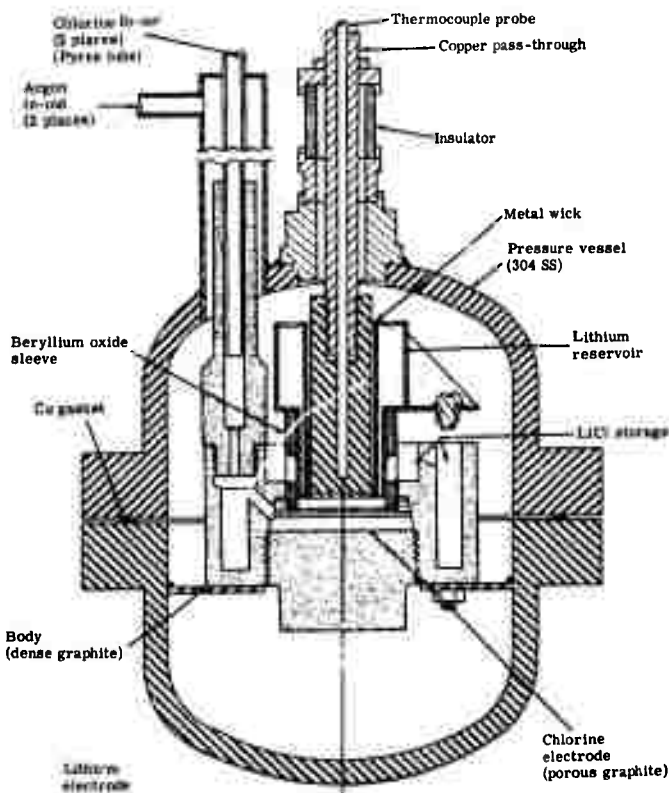
5291-55

Figure 55. Performance of stray current cells.

Allison

POWER DENSITY CELL NO. 11**Description**

The design for this cell run was completely different than the preceding cell designs. It consisted of horizontal circular Cl₂ and Li electrodes with the Li initially stored within the cell (primary cell capable of discharge only). This cell design is shown schematically in Figure 56.



5291-56

Figure 56. Cross-section view of cell No. 11.

Allison

The Cl_2 electrode was designed to permit excess Cl_2 flow-by. This was accomplished by drilling 1/16-in. dia holes 0.020 in. below the electrode surface and then properly mating the dense graphite body and the electrode so that Cl_2 could be admitted to and collected from these flow channels. The top surface of the Cl_2 electrode was grooved to increase the electrolyte/electrode contact area.

The original Li electrode design was modified to facilitate loading with Li. Initially, the Li electrode consisted of a stainless steel matrix enclosed by a metal container. This matrix configuration, in addition to the cell assembly design, prevented filling the Li reservoir by normal means. The matrix was removed and replaced by a Feltmetal® wick to form an annulus where molten Li could be cast into place. The wick provided a transport path for Li from the reservoir to the electrode surface. An electrolyte spacing of approximately 0.10 in. was maintained by a beryllium oxide spacer. The spacer was slotted to permit LiCl flow from the electrolyte region to a storage reservoir.

Operation and Test Results

The cell was assembled in a dry box to keep the Li and LiCl in an inert environment. Lithium was heated above its melting point and then poured into the annular reservoir. Finely powdered LiCl was then packed into the electrolyte region with sufficient LiCl placed in the outer storage region to fill the electrolyte region after its melting temperature was reached. Final cell assembly was accomplished by bolting (electrically isolated with Pyrex sleeves) the Li assembly and graphite cell body to the lower pressure vessel half. Final assembly was completed by lowering the upper pressure vessel half over the Cl_2 feed tubes and simultaneously inserting the Li current and voltage probe into the lithium reservoir. This final operation was completed with extreme difficulty due to the fragility of the graphite feed tubes, etc. The pressure vessel was installed in a kiln furnace and heated to approximately 650°C in approximately 1.5 hr. During this time, argon was passed through the Cl_2 feed system to provide an inert atmosphere.

At approximately the melting point of the LiCl , argon could not be passed through the Cl_2 feed system. Shortly thereafter, lithium appeared in the Cl_2 exit tube. This indicated that Li had left the reservoir and attacked the Cl_2 electrode sufficiently to enter the feed channels. The test was then terminated with no performance data obtained. Subsequent inspection revealed the dense graphite body had separated into two halves. This failure is believed to have resulted from differences in thermal expansion of the graphite and pressure vessel during heat-up to cell temperature. This would have resulted in loss of the electrolyte and would have allowed Li to reach the Cl_2 electrode and destroy it. No further testing of this design was attempted.

Allison

SECTION V

ANALYTICAL SYSTEMS STUDIES

The goal of the systems studies was to define primary battery design concepts utilizing the Li-Cl₂ fused salt couple and to evaluate the system characteristics over a range of operational, design, and environmental parameters. Specifically, these parameters included the following:

- Power level—5 to 30 kw_e (1 kw_e for design C)
- Power density—10 to 30 w/cm²
- Discharge times—10 to 30 min
- Operation at zero g or in a gravity field
- Heat rejection via radiation or to an internal heat sink

The system results developed in this study are aimed at exploring the effects of system design parameters on battery energy density and related parameters to permit the evaluation of tradeoffs between battery design and installation parameters.

Four short duration batteries were evaluated during this program to determine the effects of environmental or operational parameters and performance parameters. In addition, longer discharge systems of up to 100-hr duration were investigated. The designations of the five systems (A-1, A-2, B-1, B-2, and C) were coded to indicate the design conditions for the system. See Table V.

Table V.
Li-Cl₂ primary battery systems.

<u>Design</u>	<u>Gravity field</u>	<u>Thermal control</u>	<u>Mission time (min)</u>
A-1	0	Radiation	10 to 30
A-2	0	Heat sink	10 to 30
B-1	nonzero	Radiation	10 to 30
B-2	nonzero	Heat sink	10 to 30
C	nonzero	Radiation	to 6000

Each short duration system was designed at a baseline condition of 10 kw_e power level, 20 w/cm² power density, 30-min discharge time, and with an approximate battery voltage of 30 v. This baseline design was then scaled over the range of cell and battery design parameters as previously noted.

In addition, the systems with internal heat sinks were scaled over a range of battery case temperatures from 200 to 600°F. The extended discharge battery (C) was designed at the 1 kw_e power level and examined at discharge times of 10 and 100 hr with current densities ranging from 10 to 30 w/cm².

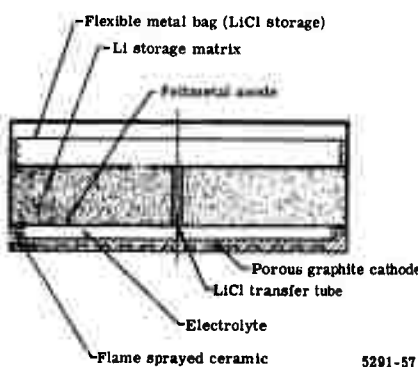
Each battery design is described in the following paragraphs including a discussion of the individual cell design utilized and the resulting parametric values for the system. A comparison of the design characteristics is included at the end of the section.

DESIGN A-1

As previously noted, this design was to operate in zero g conditions, radiating its excess heat to space from its high temperature battery surface. The basic cell design used in this concept is described in the following paragraphs followed by a discussion of the battery baseline design. System scaling data are presented for the range of design parameters already outlined.

Cell Design

The individual cell concepts used as a basis for the battery designs in this study were of circular cross section with the Li stored within each cell. A sketch of the A-1 cell is shown in Figure 57, presenting the major cell features. The cathode is machined from porous graphite to provide thin Cl₂ flow paths (\approx 0.050 in.). The back surface (or Cl₂ supply side) has a supporting grid work to provide mechanical strength and an electrical conduction path. The Li reactant is stored in a low density porous metal matrix within the cell and the lower surface serves as the anode of the cell. Cell operation relies on the difference in surface tension characteristics of Li and LiCl, with Li preferentially wetting the matrix material.



5291-57

Figure 57. Sketch of A-1 cell cross section.

System Design

The design characteristics of the A-1 battery designed to operate under zero g conditions are presented herein. Calculation procedures are shown for each of the major components in this design. The battery design can be divided into two sections—the power section and Cl₂ supply section: each is discussed in the following paragraphs. The A-1 battery configuration is shown in Figure 58.

Cl₂ Supply System

The Cl₂ supply system has been designed to provide Cl₂ vapor to the cell stack throughout the discharge cycle under zero g conditions. This is accomplished by maintaining Cl₂ in the vapor state throughout the pressure vessel. The use of high Cl₂ pressure reduces cell polarization problems associated with Cl₂ impurities. The supply of vapor to the

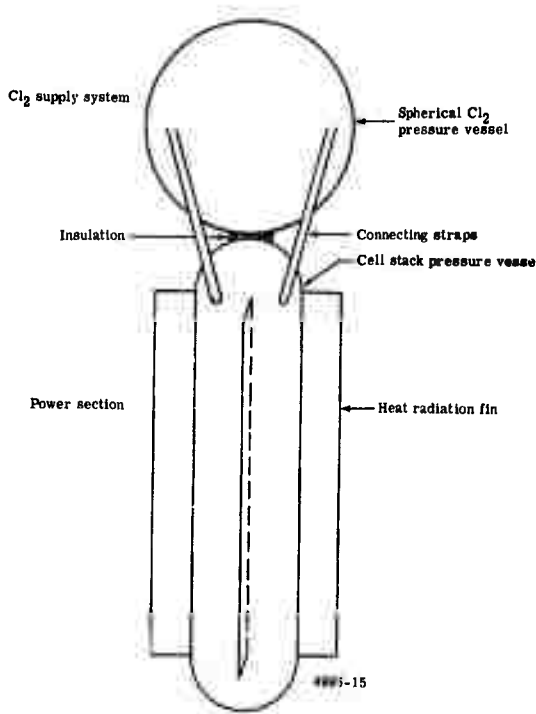


Figure 58. A-1 battery configuration.

cell stack also eliminates the possibility of supplying liquid Cl_2 to the cell stack which could result in instantaneous pressure surges in the cell stack pressure vessel.

Chlorine is initially stored, prior to activation, under its own vapor pressure. On activation it is heated to a temperature of 350°F and a pressure of 1600 psia. (The procedures used in the selection of this state point are discussed later.) The critical pressure and temperature for Cl_2 are 1118.4 psia and 291.2°F. Thus, at the initial condition, the Cl_2 tank can contain no liquid. As the cell stack discharges, heat is added to the Cl_2 tank such that the Cl_2 is maintained at a near constant bulk temperature of 300°F. The final Cl_2 pressure will be of the order of 700 psia. Figure 59 shows the path that the Cl_2 follows during discharge on a pressure-enthalpy chart.

A heat storage unit is enclosed in the Cl_2 tank to supply the heat required to the Cl_2 . The source of heat is the heat of fusion of a halide mixture of 0.60 mole CuCl and 0.040 mole KCl . The amount of heat required by the Cl_2 varies as a function of time. Since the conductivity of a gas is not pressure dependent, the use of heat of fusion satisfies the requirement of a variable heat source at constant temperature, in particular, a heat source at a constant 350°F.

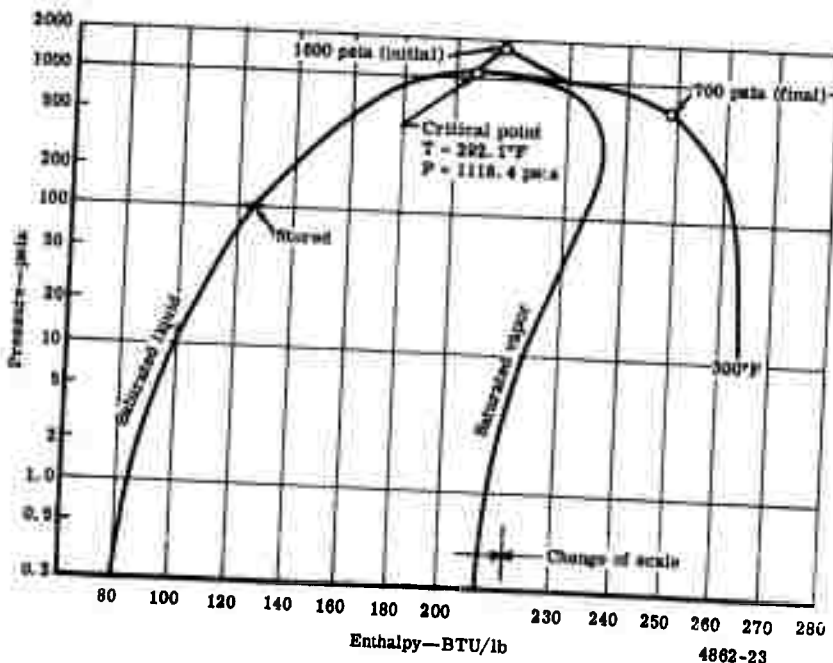
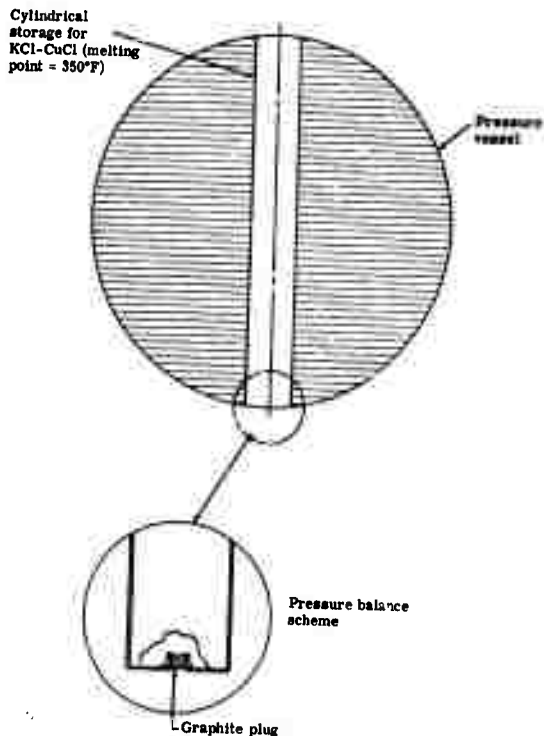


Figure 59. Pressure-enthalpy diagram for Cl_2 during discharge.

Since the heat storage unit must function in a zero g environment, the only effective mode of heat transfer is conduction. However, as is typical of all gases, Cl₂ vapor has an extremely low conductivity. The technique chosen to distribute the heat throughout the Cl₂ was to use circular fins about the cylindrical heat source. Figure 60 shows a sketch of the design of the heat storage unit located inside the Cl₂ tank. An electrical heating element is enclosed in the cylindrical heat source for Cl₂ subsystem activation. The heating element is sized for a 5-min start-up time. As the Cl₂ subsystem is heated, Cl₂ pressure will go from about 100 psia to 1600 psia. To reduce weight, the cylindrical heat storage cylinder is pressure balanced. The technique proposed is to use a porous graphite plug to cover a vent in the cylinder surface. This concept is illustrated in Figure 60.



4862-24

Figure 60. Sketch of heat storage unit conceptual design.

Allison

The amount of heat which must be added to the Cl_2 vapor is dependent on the amount of excess Cl_2 and is a function of time

$$\frac{dQ_{\text{Cl}_2}}{d\tau} = \frac{\dot{W}_{\text{Cl}_2} V_T}{(W_{0_{\text{Cl}_2}} - \dot{W}_{\text{Cl}_2} \tau)^2} \frac{dv_{\text{Cl}_2}}{dP} \left[\frac{V_T}{v_{\text{Cl}_2}} \frac{dh_{\text{Cl}_2}}{dP} - V_T \right] \quad (35)$$

where

\dot{W}_{Cl_2} = Cl_2 flow rate

W_0 = initial Cl_2 weight

V_T = Cl_2 tank volume

τ = time

v_{Cl_2} = specific volume of Cl_2

P = pressure

h_{Cl_2} = enthalpy of Cl_2

A linear approximation was made for dv/dP and dh/dP over the operating pressure range. The maximum heating rate of the Cl_2 occurs at final mission time. Figure 61 shows the effect of mission time on Cl_2 heating rate.

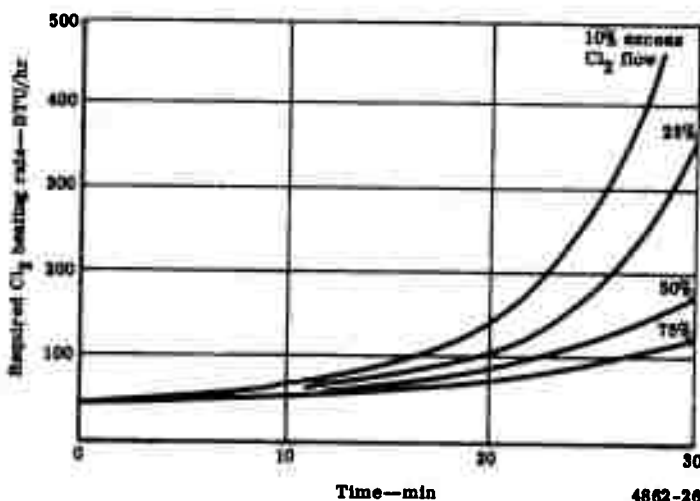


Figure 61. Effect of mission time on Cl_2 heating rate.

Allison

For a given conducting fin root temperature and fin design, there exists a value of excess Cl_2 (i. e., maximum heating rate) which results in minimum Cl_2 system weight. As the percent excess Cl_2 approaches zero, the heating rate approaches infinity, or the fin weight becomes extremely large. A point exists where an increase in excess Cl_2 weight is not accompanied by a greater decrease in fin assembly weight.

During battery activation, the Cl_2 system will be heated to the root temperature (heat storage material melting temperature). This temperature defines the pressure for which the pressure vessels must be designed. A root temperature exists, therefore, which results in minimum weight for a constant value of excess Cl_2 . A combination of root temperature and excess Cl_2 flow exists that will result in minimum weight. A computer program was written to define this combination. This minimum weight occurred at about 30% excess Cl_2 flow and a root temperature of 350°F. The initial Cl_2 temperature of 350°F corresponds to an initial Cl_2 tank pressure of 1600 psia. The final pressure will be approximately 700 psia.

The weight of $\text{KCl}-\text{CuCl}$ required for heat storage can be calculated by integrating dQ_{Cl_2}/dt to solve for Q_{Cl_2} . This is the total heat which must be added to the Cl_2 during discharge.

$$Q_{\text{HS}} = \frac{V_T}{dV_{\text{Cl}_2}} \left[\frac{dh_{\text{Cl}_2}}{dP} \ln \left(\frac{W_{0\text{Cl}_2}}{W_{0\text{Cl}_2} - W_{\text{Cl}_2} \tau_F} \right) + \frac{W_{\text{Cl}_2} V_T \tau_F}{W_{0\text{Cl}_2} (W_{0\text{Cl}_2} - W_{\text{Cl}_2} \tau_F)} \right] \quad (36)$$

where

Q_{HS} = heat supplied from heat storage
 τ_F = final time

The heat of fusion for the mixture of 0.060 mole CuCl and 0.40 mole KCl , which has a melting point at 350°F, is approximately 88 BTU/lb.

The computer-calculated weight breakdown of the Cl_2 system for the 30-min mission is as follows:

Weight (lb)

Cl_2	6.35
Pressure vessel	4.21
Fins	2.29

<u>Weight (lb)</u>	
Heat storage material	0.65
Heat storage cylinder	0.08
Cl ₂ system weight	13.48

The dimensions of the Cl₂ supply system are as follows:

<u>Dimensions (in.)</u>	
Pressure vessel radius	4.24
Pressure vessel thickness	0.063
Cylinder radius	0.430
Fin spacing	0.260

The maximum required heating rate is 277.6 BTU/hr. The total heat input is 47.8 BTU.

Calculations have shown that by allowing the cell stack pressure vessel to see the Cl₂ storage tank, the rate at which heat is radiated between the vessels and conducted through connecting straps is greater than the rate of heat radiation from the Cl₂ tank to space. As a result, by controlling the surface conditions of the Cl₂ tank and allowing the aforementioned heat leak, insulation will not be required for the Cl₂ tank.

The proposed method of connecting the Cl₂ supply unit and the power section is shown in Figure 58. In this design, a high density Min-K 1301 insulating pad is placed in compression by three locating straps in tension. These straps, due to their small cross section, could be metallic. The heat leaks through the straps and insulating pad are insignificant when compared to the heat radiated between the power section and the Cl₂ tank.

Power Section

The power section consists of the cell stack (10 cells in series), cell stack supports, and the finned pressure vessel. The cell stack supports also serve as conduction paths to the heat rejection surface.

The cell stack contains 10 of the previously described cells in the A-1 battery to provide approximately 30v under load conditions. The cell stack is housed in a pressure vessel which operates at the same pressure as the Cl₂ supply tank. Since the dead-ended cathode concept is used, no manifolding of Cl₂ is required. Instead, the cell stack operates within a high pressure Cl₂ environment and thus Cl₂ is fed from the Cl₂ tank as needed.

Allison

The computer-calculated performance characteristics of a Li-Cl₂ battery operating at a mean Cl₂ pressure of 80 atm, a power density of 20 w/cm², an electrolyte thickness of 0.118 in., and a Poco-AX graphite cathode 0.050 in. thick are as follows:

- Current density, i_d —6.54 amp/cm²
- Open circuit voltage, V_{oc} —3.64 v
- Voltage efficiency, η_v —0.840
- Current efficiency, η_i —0.975
- Operating voltage, V_{op} —3.06 v

The weight of reactants consumed in the production of 10 kw_e for 30 min was calculated as

$$W_{LiCl_G} = \frac{E}{\eta_v \eta_c C V_{oc}} = 5.84 \text{ lb} \quad (37)$$

where

W_{LiCl_G} = weight of LiCl generated in discharge

E = energy required

C = electrochemical equivalent

The weight of each reactant consumed is

$$W_{Li_c} = \frac{M_{Li}}{M_{LiCl}} (W_{LiCl_G}) = 0.956 \text{ lb} \quad (38)$$

where

M = atomic weight

W_{Li_c} = weight of Li consumed

$$W_{Cl_2c} = 5.84 - 0.956 = 4.884 \text{ lb}$$

The following assumptions were made in sizing the cell volume required for Li matrix storage:

- 5% dense metallic matrix
- 10% available Li excess
- 80% utilization factor

Allison

The latter factor assumes only 80% of the Li in the matrix can be fed to the anode. The weight of Li stored in each cell is

$$W_{LiS} = \frac{W_{LiC} (1.10)}{0.8N} = 0.1315 \text{ lb} \quad (39)$$

where

$$\begin{aligned} W_{LiS} &= \text{weight of Li stored} \\ N &= \text{number of cells} \end{aligned}$$

The volume of the Li stored in each cell is

$$V_{LiS} = \frac{W_{LiS}}{\rho_{Li}} = 7.54 \text{ in.}^3 \quad (40)$$

where

$$V_{LiS} = \text{volume of stored Li}$$

$$\rho_{Li} = \text{density of Li}$$

$$V_{matrixS} = 0.05 (75.4) = 0.377 \text{ in.}^3$$

The volume of the Li storage compartment is approximately 7.92 in.³. The weight of the matrix material for each cell will be 0.1095 lb ($\rho = 0.29 \text{ lb/in.}^3$). Thus, the weight of the filled Li matrix per cell is 0.241 lb.

The volume of the LiCl generated per cell during discharge is

$$V_{LiClG} = \frac{W_{LiCl}}{\rho_{LiCl}} = 10.72 \text{ in.}^3 \quad (41)$$

The weight of LiCl stored in the electrolyte is 0.0675 lb/cell. The volume expansion of LiCl on melting is approximately 0.365 in.³ per cell. The net volume required for LiCl storage, assuming a 10% safety factor is

$$\begin{aligned} V_{LiClS} &= 1.10 \left(V_{LiClG} - \frac{W_{LiC}}{N \rho_{Li}} + 0.365 \text{ in.}^3 \right) \\ V_{LiClS} &= 6.08 \text{ in.}^3 \end{aligned} \quad (42)$$

Allison

It was assumed that a 0.125-in. lip will be required to braze the cathode structure to the reactant containment section. The diameter of the cathode is 3.14 in.; therefore, the diameter of the storage region is 3.39 in. Based on these dimensions, the various cell region heights are:

Dimensions (in.)

LiCl storage	0.670
Li storage	0.376
Electrolyte	0.118
Cathode	0.100
Structure	0.020
LiCl bag	0.003
Cell height	<u>1.782</u>

The corresponding weight breakdown of the cell is:

Weight (lb)

Cell structure	0.1680
Li	0.1315
Cathode	0.0200
LiCl	0.0675
Matrix	0.1095
LiCl metal bag	<u>0.0120</u>
Cell weight	0.5087 \cong 0.509
Cell stack weight	5.09

To activate the cell stack, heat must be supplied to the power section to melt the Li and LiCl electrolyte. A breakdown of the heat input required to raise the temperature of the power section to 1200°F is as follows:

Heat input (kcal)

Li	425.0
LiCl	71.0
Matrix	33.7
Cathode	12.8
Cell structure	51.0
Cell supports	18.6
Pressure vessel	106.0
Heat input required	766.3 or 1040 BTU

Allison

A 5-min heat-up time was assumed. The rating of the assumed 0.2-in. dia heating element is 60 w/in.² (37.8 w/in. or 129 BTU/hr/in. This corresponds to a heating rate of 36,500 BTU/hr and requires 280 in. of heating element length and a weight of 2.64 lb. The element could be wrapped around the pressure vessel.

The heat required to raise the Cl₂ supply system temperature to 350°F is as follows:

<u>Heat Input (BTU)</u>	
Cl ₂	635
Pressure vessel	122
Heat storage	72
Fins and cylinder	71
Heat required	<u>900</u>

This corresponds to a heating rate of 10,800 BTU/hr for a 5-min start-up time. The corresponding heater element length is approximately 84.0 in. and the weight is 0.79 lb. This element could easily be placed inside the heat storage cylinder.

A design requirement was that the heat generated during discharge be radiated to space. Since the heat radiating surface is the outer surface of the surrounding pressure vessel, heat must be transferred from the cell stack to the outer vessel. The design constraint of a zero g operating condition means convection is not an available mode of heat transfer. Calculations have shown that heat can not be radiated between the cell stack and the pressure vessel at a sufficient rate to prevent cell heating. As a result, heat conduction paths must be created between the cell stack and the pressure vessel. The proposed cell design uses three equally spaced cell stack supports for this purpose. The section of these supports in contact with the cell reaction region is flame-sprayed with alumina. The back side of the support is also flame-sprayed with alumina and is in contact with the pressure vessel.

The waste heat generated during discharge comes from the heat release from direct reaction (\dot{Q}_{dr}) of Li diffusing through the electrolyte to the Cl₂ electrode and the so-called TΔS heating, or

$$\dot{Q}_{rej} = \dot{Q}_{dr} + \dot{Q}_{T\Delta S} \quad (43)$$

The heat release from the direct reaction is

$$\begin{aligned} \dot{Q}_{dr} &= \Delta H \cdot i_{ddif} \cdot A_{cath} \\ &= 334 \text{ w} \end{aligned} \quad (44)$$

where

$$\begin{aligned}\Delta H &= \text{heat of reaction} \\ i_d \text{dif} &= \text{diffusion current density} \\ A_{\text{cath}} &= \text{area of cathode}\end{aligned}$$

The $T\Delta S$ heating can be calculated using the relationship

$$\begin{aligned}T\Delta S &= \Delta H - \Delta F \\ \dot{Q}_{T\Delta S} &= (4.0 - V_{op}) (i_d) (A_{\text{cath}}) \\ &= 3180 \text{ w}\end{aligned}\tag{45}$$

where

$$\begin{aligned}\Delta F &= \text{free energy} \\ i_d &= \text{current density}\end{aligned}$$

Therefore, the magnitude of Q_{rej} is the sum or

$$Q_{\text{rej}} = 334 + 3180 = 3514 \text{ w} = 11,960 \text{ BTU/hr}$$

A portion of this heat will be used to heat the incoming Cl_2 (\dot{Q}_{Cl_2}). The incoming Cl_2 temperature is 300°F and the flow rate is 9.78 lb/hr . The rate at which heat must be rejected from the pressure vessel is

$$\begin{aligned}\dot{Q}_{\text{rad}} &= \dot{Q}_{\text{rej}} - \dot{Q}_{\text{Cl}_2} \\ &= \dot{Q}_{\text{rej}} - C_{P\text{Cl}_2} (\dot{W}_{\text{Cl}_2}) (\Delta T) \\ &= 10,550 \text{ BTU/hr}\end{aligned}\tag{46}$$

where

$$\begin{aligned}C_{P\text{Cl}_2} &= \text{specific heat of Cl}_2 \\ \Delta T &= \text{temperature rise}\end{aligned}$$

In sizing the conduction paths, it was assumed that the cell stack was at a uniform temperature of 1200°F and the radiation rejection temperature was 1000°F . The emissivity of both vessels was assumed to be 0.80. The magnitude of heat transfer via radiation is

Allison

$$\dot{Q}_{\text{rad,cs-p}} = \frac{\sigma A_{\text{cs}} (T_{\text{cs}}^4 - T_p^4)}{\frac{1}{\epsilon_{\text{cs}}} + \frac{A_{\text{cs}}(1)}{A_p(\epsilon_p - 1)}} = 4800 \text{ BTU/hr} \quad (47)$$

where

σ = Stefan-Boltzmann constant

A_{cs} = cell stack area

T_{cs} = cell stack temperature

T_p = pressure vessel temperature

ϵ_{cs} = emissivity of cell stack

ϵ_p = emissivity of pressure vessel

A_p = pressure vessel area

An additional 300 BTU/hr is transferred by radiation out of the ends of the cell stack. Thus, 5100 BTU/hr is transferred via radiation. The remaining 5450 BTU/hr must be conducted.

The conduction of Cl_2 from 1200 to 1000°F is about 0.012 BTU/hr. The spacing between the cell stack and the pressure vessel is 0.2 in. Assuming the cell stack to be at a uniform diameter of 3.40 in., the heat conduction rate through the Cl_2 is

$$\dot{Q}_{\text{cond,Cl}_2} = \frac{2\pi k \text{Cl}_2 \Delta T}{\ln\left(\frac{r_p}{r_{\text{cs}}}\right)} = 140 \text{ BTU/hr} \quad (48)$$

where

k = conductivity of Cl_2 gas

r_p = radius of pressure vessel

r_{cs} = radius of cell stack

Therefore, the heat transfer rate through the conduction members ($\dot{Q}_{\text{cond,m}}$) must be 5310 BTU/hr.

The required total cross section of the conduction path per cell (A_m) is

$$A_m = \frac{\dot{Q}_{\text{cond,m}}}{k_m (\Delta T / \Delta r) N} = 0.0514 \text{ in.}^2 \quad (49)$$

It was assumed that nickel plated copper strips would be used for the conduction members.

The calculated cross section of each member is 0.008 in.². For an assumed width of 0.500 in., the corresponding thickness is 0.016 in. However, no account was made for contact resistances or conduction through the insulating material. It was assumed that the member dimensions would be 0.5 in. \times 0.03 in. The calculated weight of each member is 0.22 lb, or a total weight of 0.668 lb.

As previously stated, the cell stack operates at the same pressure level as the Cl₂ supply tank. The operating pressure will vary from about 1600 psia initially to 700 psia at complete discharge. The pressure vessel has hemispherical ends and the cylindrical height of the pressure vessel is the same as the height of the cell stack. Its radius is 0.2 in. larger to allow room for cell stack supports.

It was assumed that the design stress for the vessel was 60,000 psia with a joint efficiency of 0.9. The maximum Cl₂ pressure was found to be 1600 psia. The required wall thickness was calculated using the expression

$$t_p = \frac{Pr_p}{\phi e - 0.6 P} = 0.06 \text{ in.} \quad (50)$$

where

t_p = thickness of pressure vessel

ϕ = design stress

e = joint efficiency

The calculated weight of the pressure vessel for the 30-min mission time was 4.77 lb.

Calculations have shown that for mission times less than 30 min and an outer surface temperature of 1000°F (200°F less than cell stack temperature), the pressure vessel must be finned. Since the heat rejection rate is a constant, the problem of heat radiation increases as the size of the power section decreases (i.e., shorter mission times), requiring fins or constant pressure vessel size to maintain the necessary rejection surface area. For weight considerations, these fins will be constructed from copper. A computer program was written to determine the fin design (i.e., fin thickness, number of fins, and fin width) which will give minimum weight.

In sizing the fin for the heat rejection surface, the cylinder surface and the fin surface were assumed to have an emissivity of 0.8 and a temperature of 1000°F.

The effective area required at 1000°F to reject all heat is

$$A_{rej} = \frac{Q_{rad}}{\sigma \epsilon T_p^4} \quad (51)$$

A computer program was written to determine the minimum weight fin geometry. The program assumed a fin thickness and number of fins and determined the fin length necessary to radiate \dot{Q}_{rad} . The process was repeated for various thicknesses and numbers of fins. The calculations considered fin effectiveness (η_f), the view factors of the fin to space, and the bare cylinder surface to space.

The value of the fin view factor-to-space (f_{f-sp}) is calculated using Figure 62:

$$f_{f-sp} = \frac{A_1 + A_2' - A_3}{2 A_1} \quad (52)$$

The effective radiating area (A_{fe}) at 1000°F is

$$A_{fe} = A_{fa} \cdot \eta_f \cdot f_{f-sp} \quad (53)$$

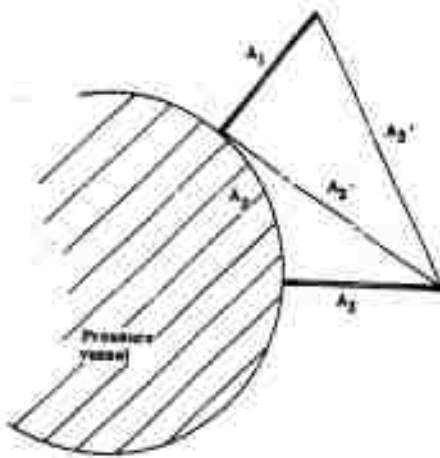
where

A_{fa} = actual fin area

η_f = fin efficiency

The view factor of the bare cylinder to space (f_{p-sp}) is

$$f_{p-sp} = 1 - 2 \left(\frac{A_2 + A_3 - A_2'}{2 A_2} \right) \quad (54)$$



4862-25

Figure 62. Reference for view factor equations.

The effective cylinder area is

$$A_{Pe} = A_{Pa} \cdot f_{p-sp} \quad (55)$$

where

A_{Pe} = equivalent pressure vessel area

A_{Pa} = actual pressure vessel area

The total effective area is the sum of the A_{fe} and A_{pe} . From a given combination of fin thickness and number of fins, the computer iterates to define the value of fin width which causes the sum to equal A_{req} .

The total weight of the A-1 battery system was 27.494 lb—14.27 lb for the Cl_2 system and 13.224 lb for the power system and support structure. This corresponds to an energy density of 182 w-hr/lb. The volume was 0.32 ft³, resulting in a volume energy density of 9.1 w-hr/cm³.

Parametric Scaling of the A-1 Design

The base-line design was sized for 10-kw_e output at 20 w/cm² with a 30-min operating time. Scaling to reduced mission times reduced the height of the reactant storage regions within each cell and the overall battery height. Since the heat rejection rate is not a function of time, the shorter mission time results in higher heat rejection per unit area for the battery case. Thus, for some design conditions, it was necessary to use a larger battery case (than required to contain the cell stack) to provide the necessary heat rejection surfaces.

Changing the power density for the design alters the cell electrode diameter. A constant differential of 0.25 in. was maintained between the cell outer diameter and electrode diameter when scaling for power density. Similarly, this differential was maintained as cell diameters change for different power levels. The battery outer case was sized for each design to provide the necessary heat rejection characteristics with minimum weight. The Cl_2 supply subsystem requirements also vary with each of these parameters and was sized for each design condition using the criteria previously detailed in the discussion of the baseline design.

The basic cell and battery configuration and operating characteristics previously described were constants as the system was scaled to various conditions. The system is based on the following constraints:

Allison

Electrolyte thickness	0.118 in.
Cathode material	Poco-AX graphite
Cathode thickness	0.050 in.
Mean operating pressure	80 atm
Open circuit voltage	3.64 v
Lithium storage matrix	5% densc
Excess Li	10%
Lithium recovery from matrix	80%
Excess Cl ₂	30%
Battery outer case temperature	1000°F
No. of cells	10

Using these inputs, the cell and battery characteristics were determined for the following design conditions:

- Power level—5, 10, and 30 kw_e
- Power density—10, 20, and 30 w/cm²
- Operating times—10, 15, 20, and 30 min

The cell performance values calculated for the three power densities and used to define reactant requirements were as follows:

<u>Power density (w/cm²)</u>	<u>Operating voltage (v)</u>	<u>Current density (amp/cm²)</u>	<u>Voltage efficiency</u>	<u>Current efficiency</u>
10	3.299	3.03	0.906	0.948
20	3.06	6.54	0.840	0.975
30	2.80	10.70	0.770	0.980

The results of the parametric investigation are shown in Figures 63 through 69. Figures 63 and 64 illustrate the weight and volume characteristics of the A-1 battery design as mission time and power density are varied for the 10-kw system. The crossplot of Figure 63 is shown in Figure 65 and defines the optimum power density to be near 20 w/cm² for all operating times investigated. These data from Figures 63, 64, and 65 were combined in the composite plot shown in Figure 66 which summarizes the weight and volume data.

System characteristics at variable power levels are shown in Figures 66, 67, and 68. Figure 67 is a plot of energy density versus operating time at various battery power levels. As indicated earlier, the battery case varies from one design to another to match heat rejection and minimum weight specifications. The resulting variable battery cases are reflected in the shape of the curves shown in Figure 67.

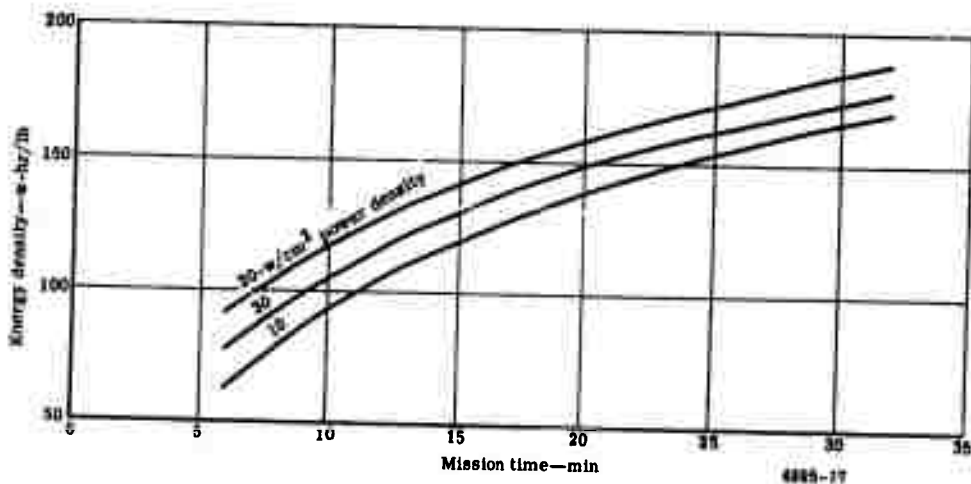


Figure 63. Energy density versus mission time at a 10-kw_e power level for the A-1 battery design.

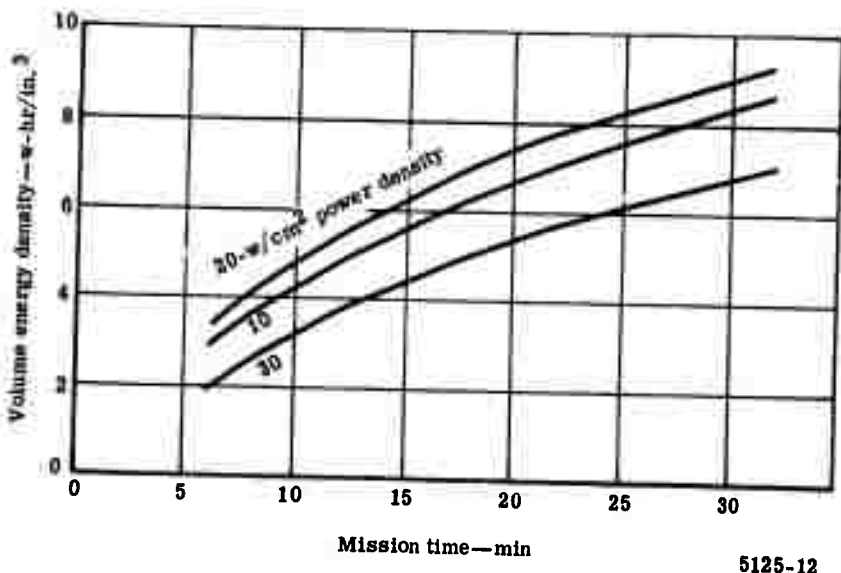


Figure 64. Volume energy density versus mission time for the 10-kw_e power level of the A-1 battery design.

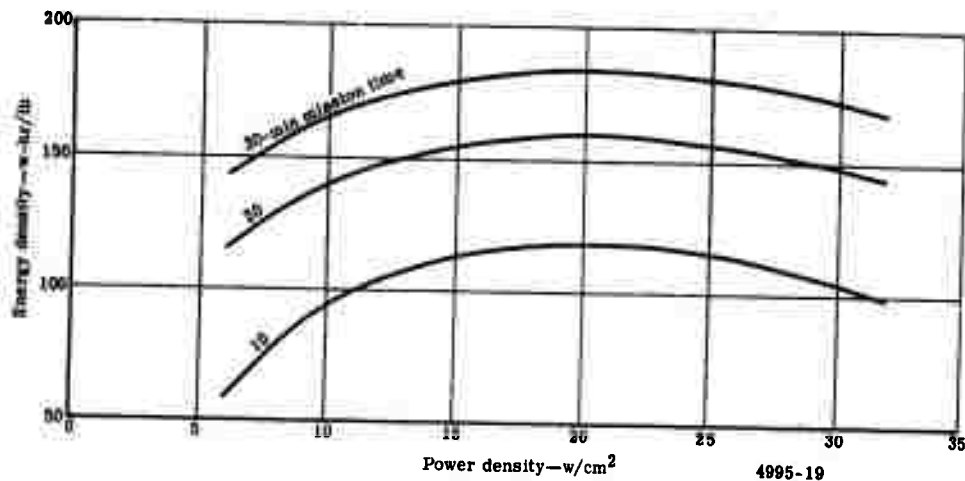


Figure 65. Energy density versus power density at a 10-kw_e power level and 30 v for the A-1 battery design.

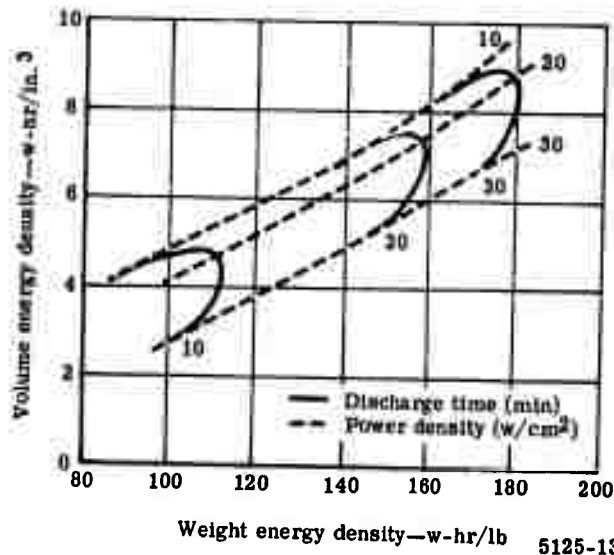
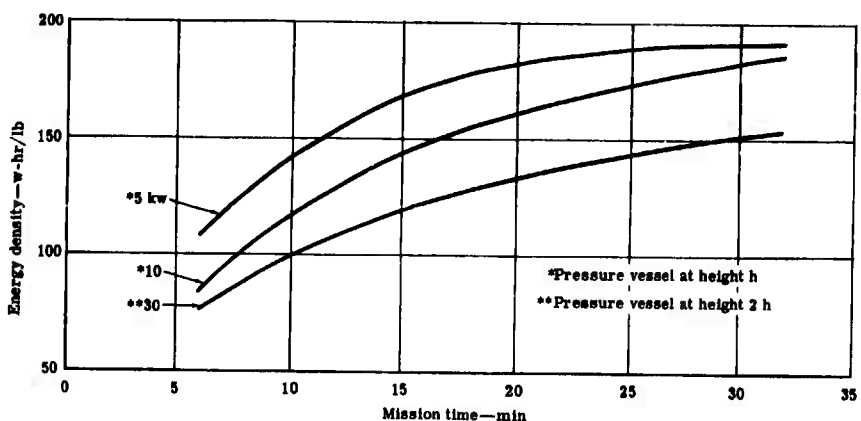
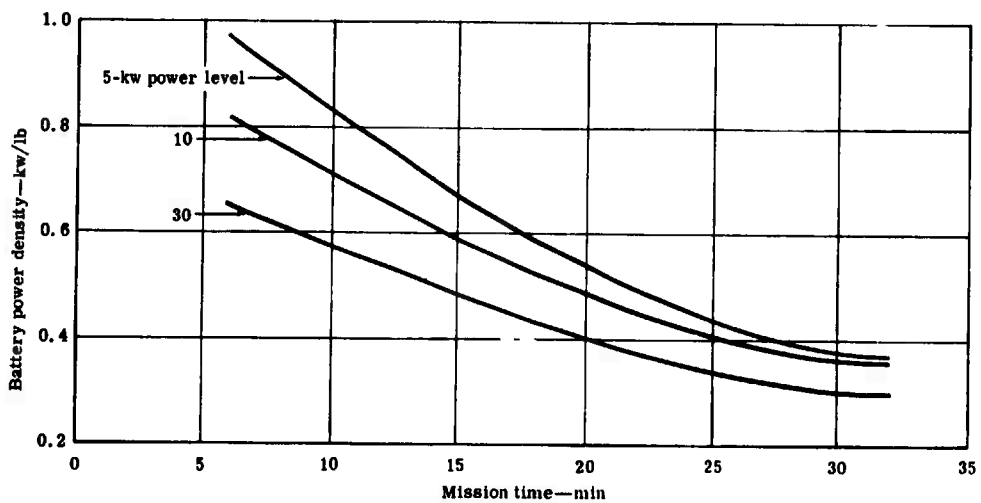


Figure 66. System characteristics of the A-1 battery design at 10 kw_e.



4995-21

Figure 67. Energy density versus mission time at 20-w/cm² power density for the A-1 battery design.



4995-22

Figure 68. Battery power density versus mission time at a 20-w/cm² power density for the A-1 battery design.

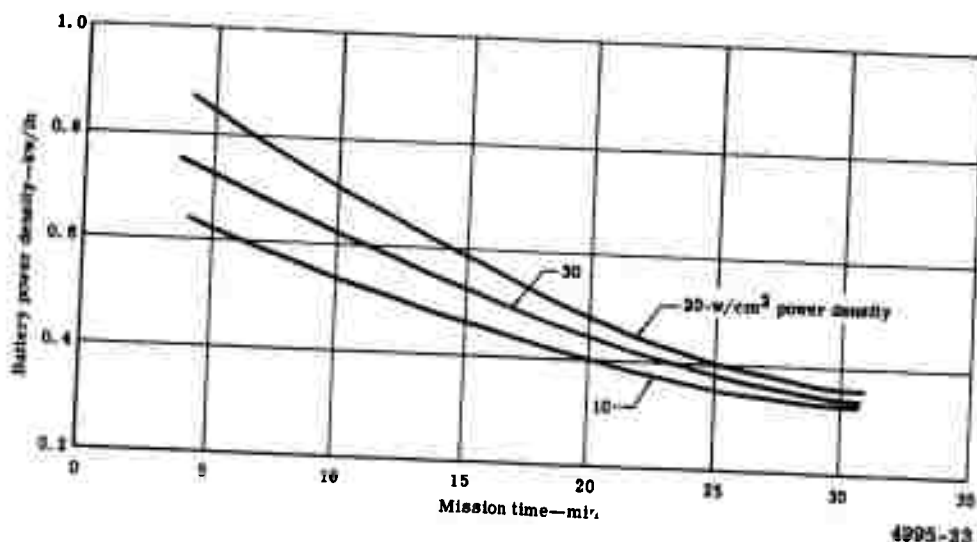


Figure 69. Battery power density versus mission time at a 10-kw_e power level for the A-1 battery design.

Battery power density versus mission time is shown in Figures 68 and 69 as a function of power level and power density. These results indicate that 20 w/cm² is near the optimum power density, while a 5-kw power level system provides a clear advantage over the higher power level systems.

A final item investigated on the A-1 battery design was to determine the effect of designing the battery for a range of voltage levels. The base-line design was varied to incorporate 5 or 15 cells to provide a voltage range from a nominal 15 to 45 v. The results are shown in Figure 70, illustrating the minor effect voltage level will have on the battery energy density.

DESIGN A-2

The distinguishing characteristic between the A-1 and A-2 battery designs is the requirement for the latter to store internally the waste heat generated during discharge instead of rejection via radiation. The design approach* utilizes the heat of fusion of LiH to absorb

*Technical Proposal for High Energy Density Li-Cl₂ Primary Battery. Allison Division, General Motors. EDR 4339. 7 July 1965.

Technical Proposal for Lithium-Chlorine Electrochemical System Feasibility Program. Allison Division, General Motors. EDR 4558. 7 February 1966.

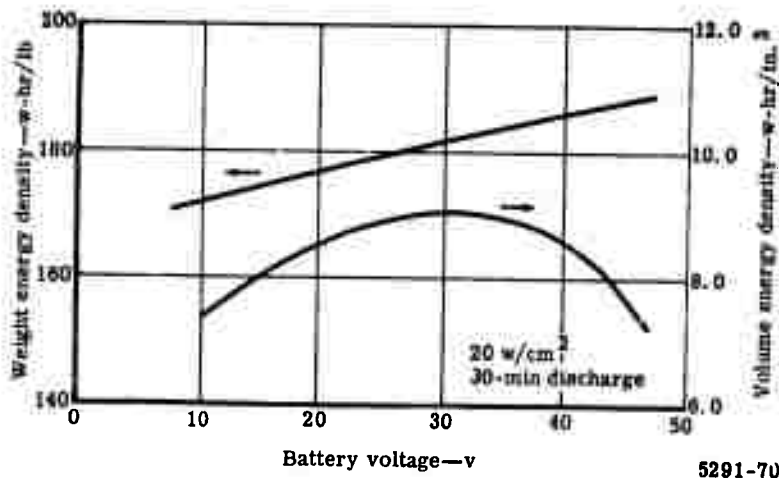


Figure 70. Effect of battery voltage on 10-kw_e A-1 battery energy density.

the heat generated during discharge. This heat sink concept is the basis for the design description and system parametrics detailed in the remainder of this section. However, alternate heat sink methods were evaluated to determine if other approaches would alter the battery weight and volume characteristics. Other methods investigated included the use of carbon tetrachloride or liquid Cl₂ as the heat sinks. Such systems use the heat of vaporization of the liquid and sensible heating of the vapor to provide both a heat sink and the Cl₂ supply to the cell. Excess vapors would have to be vented from the battery. Another approach studied would vaporize a liquid (e.g., water or ammonia) and also vent the resulting vapors. The results of these alternate approaches are presented at the end of this section on the A-2 design.

Cell Design

This design concept is for waste heat from the cells to be absorbed by melting LiH placed in close proximity to the cell electrode region. A basic constraint assumed in the evaluation of various heat sink configurations was to maintain the heat sink diameter equal to the cell reactant storage diameter. In this manner, heat sink sections could be integrated into the A-1 battery designs to provide a degree of commonality in the two systems.

The amounts of LiH required per cell, coupled with the dimensional constraint noted previously and the poor thermal conductivity of LiH, indicated the necessity of thermal paths

to distribute the thermal energy throughout the heat sink without large temperature gradients. Large gradients ($>200^{\circ}\text{F}$) would lead to increased material compatibility problems plus the increased cell reactant requirements due to cell inefficiencies at higher temperatures. Since LiH melts near 1250°F , a 100°F temperature gradient across the heat sink was used as an upper limit in defining a suitable configuration.

The following one dimensional analysis was used to estimate the LiH melting characteristics for sizing heat sinks. Based on the following assumptions,* the LiH melting system shown in Figure 71 can be approximated.

- The heat capacity of the melted LiH is negligible relative to the latent heat of fusion.
- The properties of the molten LiH are uniform, i.e., not a function of temperature.
- The solid LiH is initially at melting temperature.
- The heating rate q/A is constant.
- The heat transfer coefficient between the constant heating rate source and the LiH is infinite.

To maintain a constant heating rate into the LiH, the LiH temperature at heat absorbing surface ($x = 0$) is linear in time and experiences a known ΔT over the total melting time. The temperature transient at

$$x = 0 \text{ is } T = T_{\text{melt}} + (\Delta T, \theta_{\text{max}}) \quad (56)$$

where

T_{melt} = LiH melting temperature

ΔT = total temperature rise

θ = time

θ_{max} = total melting time

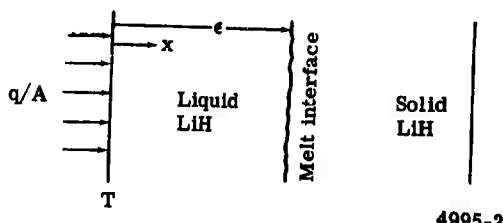


Figure 71. Model of LiH melting system.

*Kreith, F. Principles of Heat Transfer. Scranton, Pennsylvania: International Textbook Company, 1958, pp 430-36.

The rate of heat flow per unit area (q/A) across the melted LiH as a result of the temperature potential is

$$q/A = (T - T_{melt}) / (\epsilon/k) \quad (57)$$

where

ϵ = the length of melt

k = thermal conductivity of the melt

Since no sensible heat in the molten LiH is considered, the heat flow per unit area supplying the heat of fusion required for melting the LiH is

$$q/A = \rho L_m (d\epsilon/d\theta) \quad (58)$$

where

ρ = density of molten LiH

L_m = heat of fusion of LiH

Equating Equations (57) and (58) and substituting Equation (56) provides

$$\rho L_m (d\epsilon/d\theta) = (k/\epsilon)(T - T_{melt}) \quad (59)$$

$$\rho L_m \epsilon d\epsilon = (k\Delta T/\theta_{max})\theta d\theta \quad (60)$$

Integrating both sides and solving for ϵ provides

$$\rho L_m \epsilon^2/2 = k\Delta T \theta^2/2 \quad (61)$$

$$\epsilon = (k\Delta T/\theta_{max} \rho L_m)^{0.5} \theta \quad (62)$$

From Equations (57) and (62), the heating rate can be shown to be constant having the value of

$$q/A = \frac{k [T_{melt} + (\Delta T/\theta_{max})\theta - T_{melt}]}{(k\Delta T/\theta_{max} \rho L_m)^{0.5} \theta} \quad (63)$$

$$q/A = (k\Delta T \rho L_m/\theta_{max})^{0.5} \quad (64)$$

Equations (62) and (64) were used to estimate heat sink characteristics to evaluate the various design configurations considered.

Allison

A number of possible heat sink configurations were reviewed including the following:

- Heat sink adjacent to cathode
- Heat sink adjacent to anode
- Heat sink combined with lithium matrix
- Heat sink adjacent to both electrodes

The concept shown in Figure 72 was selected for use in the A-2 battery system. Two heat sinks, such as shown in Figure 72, are placed in each cell—one adjacent to each electrode as shown in Figure 73. The tapered copper fins provide conduction paths to reduce the heat sink temperature gradients to approximately 70 to 90°F for this arrangement. The copper base plate in the heat sink conducts the heat from the electrode region to the base of the fins.

Design conditions

Cells/battery—12
Power density—20 w/cm²
Power level—10 kwe

Mission time—30 min
Battery case temperature—300°F

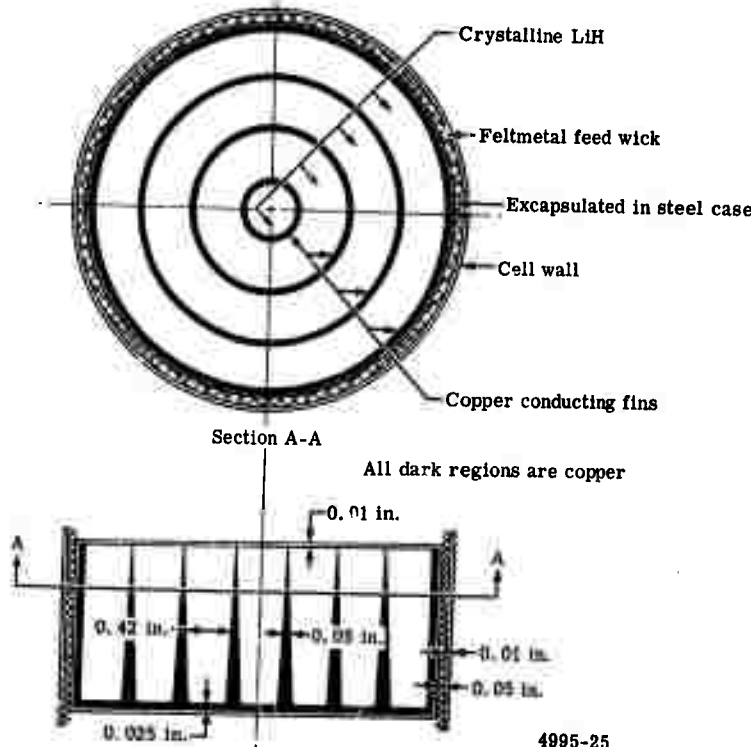


Figure 72. Heat sink design for the A-2 battery system.

Design conditions

Power density—20 w/cm²
Power level—10 kw
Cells/battery—12
Battery case temperature—300°F
Mission time—30 min

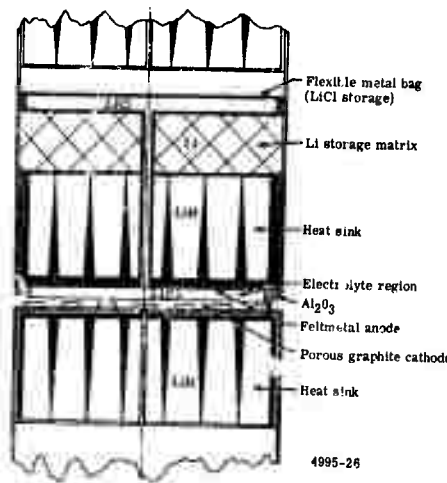


Figure 73. Li-Cl₂ cell concept for the A-2 battery design.

Feltmetal wicking is mounted between the heat sink and outer cell wall in the heat sink adjacent to the anode providing a Li feed path from the Li matrix to the anode. The weight estimated for this heat sink addition to the cell for the conditions noted in Figure 73 is 3.8 lb of heat sink for each lb of LiH required. The volume is 1.25 times greater than the LiH volume required.

System Design

The A-2 battery system is similar to the A-1 battery design with the major exception that the A-2 battery design has three stacks of four cells each rather than a single ter-cell stack as in the A-1 design. Figure 74 is a sketch of the A-2 battery layout. This change was required due to excessive cell stack heights when the heat sinks were added to each cell. For example, with a 30-min mission time, the cell height increases from 1.8 in. for the A-1 design to 4.4 in. for the A-2 system. By having three stacks of four cells, the A-2 battery is much shorter and moderately larger in diameter. Also, the larger number of cells increases the output voltage of the system from an operating voltage of approximately 30 v to about 36 v for the A-2 battery.

Design conditions

C. "s/battery—12
Power density—20 w/cm²
Power level—10 kw
Mission time—30 min
Battery case temperature—300°F

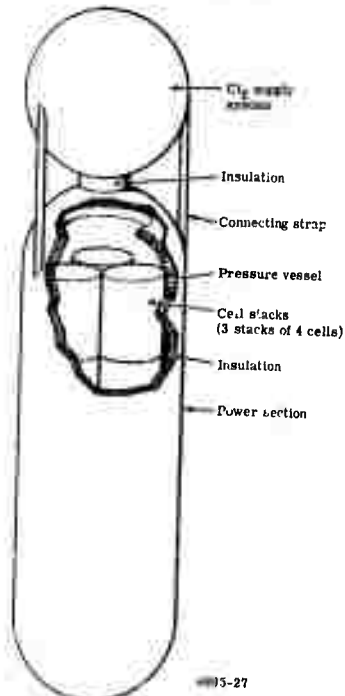


Figure 74. Design for A-2 battery system.

To maintain the temperature requirements on the surface of the pressure vessel, insulation (Min-K type 1301) was placed along the inside surface of the vessel. Thickness of the insulation is dependent on the amount of thermal energy liberated by the cell stacks and by the desired external skin temperature of the system. This also permits use of a higher design stress level for the pressure vessel.

The Cl₂ subsystem remained unchanged from the conceptual design specified for the A-1 system since zero g operation was still required.

Even though the fins from the A-1 battery design were removed from the pressure vessel for the A-2 design, the A-2 design is heavier and occupies a greater volume. The additional weight and volume of the A-2 battery design is a result of the added weight and

volume of the heat sink and insulation, along with the increased weight of the pressure vessel. The larger pressure vessel (i.e., more weight) is necessary to house the greater volume of the cell stacks.

The weight of the base-line design (i.e., 10 kw, 20 w/cm², 30 min) was 55.77 lb with a volume of 1400 in.³. The resulting energy densities were 89.6 w-hr/lb and 3.6 w-hr/in.³.

As noted earlier, alternate heat sinks were reviewed to determine if the system weight and volume characteristics could be improved. The following three alternate types of heat sinks were considered:

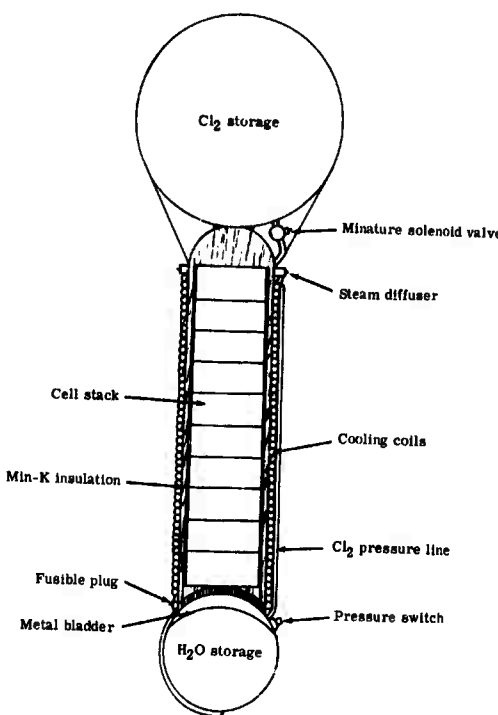
- Chlorine or Cl₂ containing compounds that act as a heat sink and subsequently release Cl₂ for cell reaction
- Heat of vaporization of a liquid—i.e., water
- Heat pipes as heat transfer media in the LiH

Several Cl₂ compounds (CCl₄, S₂Cl₂, PCl₅, and CuCl) were investigated in addition to liquid Cl₂ as possible heat sinks. A general conclusion for each source was that little or no weight advantage appeared possible when the heat absorption and Cl₂ supply criteria were matched. In addition, the difficulties of separating liquid/vapor states at zero g and the separation of impurities from the Cl₂ vapors obtained from Cl₂ compounds indicated that any weight improvements in the system would also entail offsetting system complexities.

If system requirements permit the exhausting of vapor from the power system, it appears that battery energy densities can be improved substantially over the basic A-2 heat sink design.

Utilizing a water boiler installed on the A-1 battery design, a battery operating at a 300°F skin temperature can be obtained. Such a concept is shown in the sketch in Figure 75. The energy density of this concept is 140 w-hr/lb compared to 180 w-hr/lb for the A-1 and 90 w-hr/lb for A-2 battery design.

The possible use of heat pipes as conduction paths in the LiH resulted in system weights very similar to the original A-2 battery design. Heat pipes, however, increased the volume requirements of the heat sink and the weight of packaging the heat sink. This increase offset the lower weight when comparing a heat pipe to a copper conduction fin. Of the alternate approaches to the heat sink design, improvements in energy density only appear feasible if the system characteristics will tolerate venting the coolant vapor.



5125-14

Figure 75. Sketch of the alternate heat sink design for the A-2 battery design.

Parametric Scaling of the A-2 Design

The A-2 battery design was scaled over the same range of parameters described previously for the A-1 design. In addition, the battery outer case temperature was also used as a design variable. The parameters and the ranges of values included in the study, therefore, were as follows:

- Power level—5 to 30 kw_e
- Power density—10 to 30 w/cm²
- Mission time—10 to 30 min
- Battery case temperature—200 to 600°F

The calculation of battery weight and volume for each design condition consisted of modifying the A-1 cell design for those conditions to include a heat sink and to adapt it to a 12-cell battery design. Major components which varied in scaling from the A-1 design to the A-2 design included the following:

- Cell stack pressure vessel weight and volume
- Battery start-up heating element
- Cell support weight
- Added insulation for A-2 design
- Added heat sink weight

The resulting battery weights and volumes were then combined with the design energy or power level to yield the system characteristics of w-hr/lb, w-hr/in.³, and kw/lb. These data are presented in Figures 76 through 84 for the A-2 heat sink battery concept. Figures 76 and 77 present the weight and volume energy density (w-hr/lb and w-hr/in.³) as functions of mission time and power density at a 10-kw power level. The characteristic increase in energy density with mission time is present; however, the levels are about half of the corresponding A-1 design levels, indicating the penalty associated with the heat sink requirement. Figure 78 illustrates the optimum power density of the design which varies inversely with mission time (i.e., lower power densities for longer mission times).

The weight and volume energy density increases which result from increased pressure vessel temperature are shown in Figures 79 and 80. Greater allowable surface temperature means more heat may be radiated, and consequently less heat must be internally absorbed. The larger effect of temperature on weight energy density than on volume energy density may be attributed to the difference in weight and volume design factors for the heat sink. The weight factor associated with the heat sink is about 3.8, while the volume factor is only 1.25.

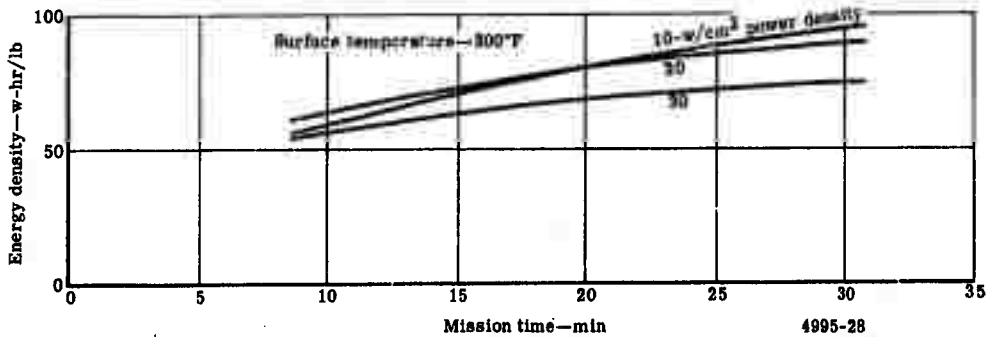


Figure 76. Weight energy density versus mission time at a 10-kw_e power level for the A-2 battery design.

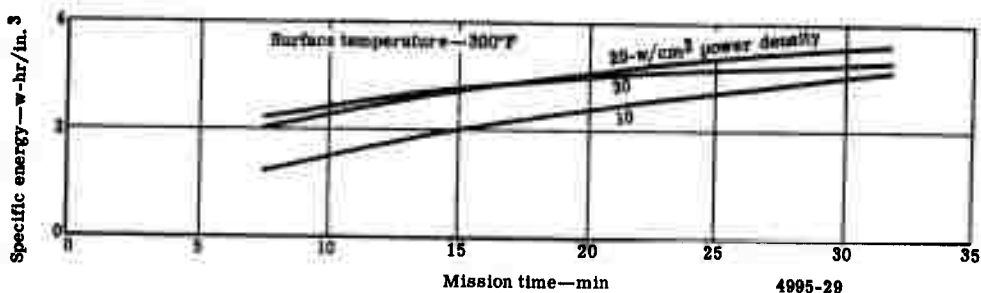


Figure 77. Volume energy density versus mission time at a 10-kw_e power level for the A-2 battery design.

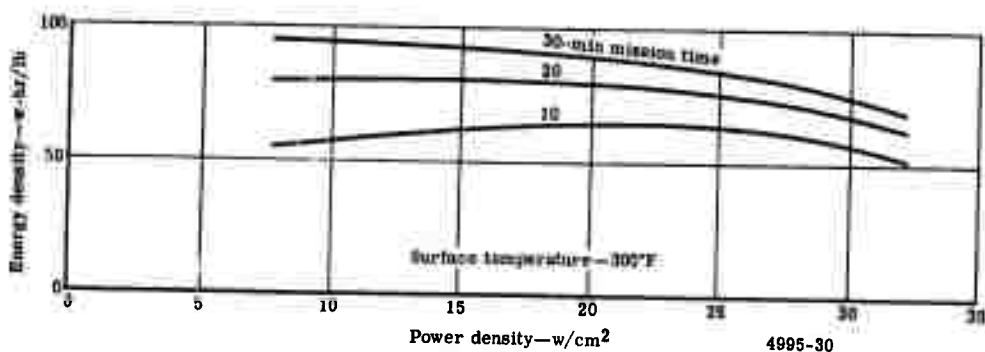


Figure 78. Weight energy density versus power density at a 10-kw_e power level for the A-2 battery design.

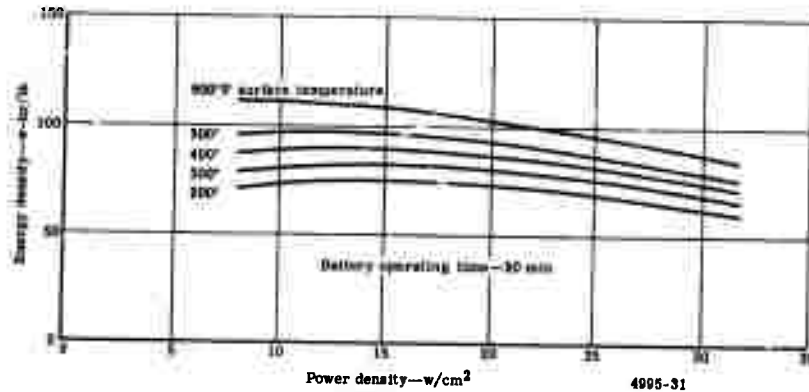


Figure 79. Weight energy density versus power density at a 10-kw_e power level for the A-2 battery design.

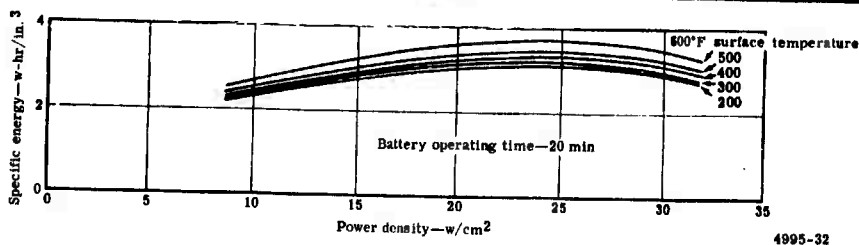


Figure 80. Volume energy density versus power density at a 10-kw_e power level for the A-2 battery design.

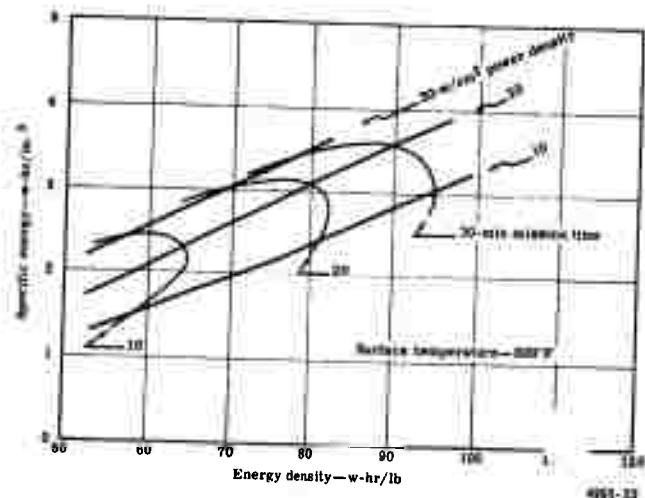


Figure 81. System characteristics of A-2 battery design at 10-kw_e power level.

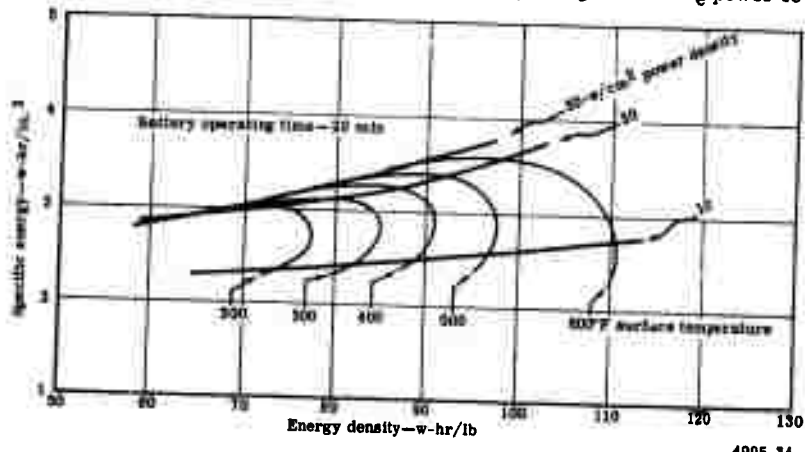


Figure 82. System characteristics of A-2 battery design at 10-kw_e power level.

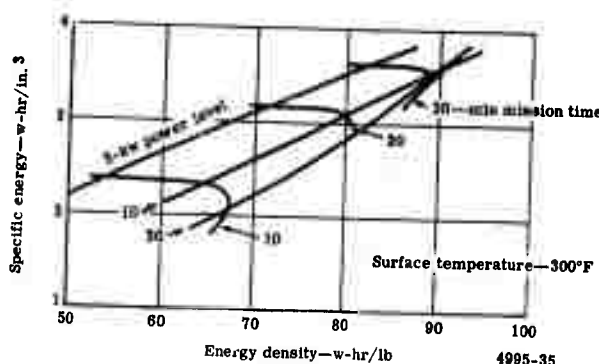


Figure 83. System characteristics of A-2 battery design at 20 w/cm^2 power density.

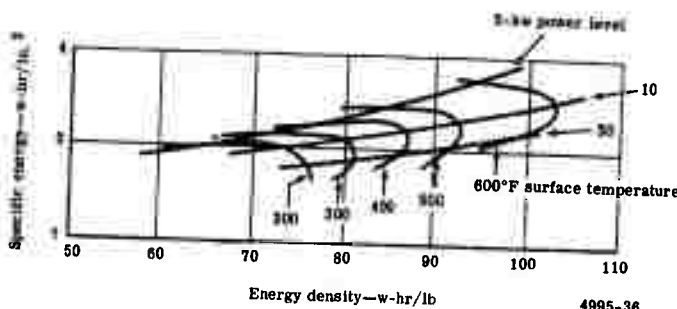


Figure 84. System characteristics of A-2 battery design at 20 w/cm^2 power density.

The parametric results of the A-2 battery design are summarized in Figures 81 to 84. These plots combine the weight and volume criteria for various power densities, power levels, mission times, and battery case temperatures. The first composite (Figure 81) shows how a weight critical system requires a lower power density than a volume critical design. Similarly, Figure 82 indicates the effects of case temperatures. Figure 83 illustrates that a 10-kw system is the near optimum power level for the A-2 battery design concept (compared with 5-kw for the A-1 design). Figure 84 relates power levels and case temperatures to the system parameters with similar results. In general, it was found that a 20 w/cm^2 power density will provide a system weight or volume that is within 4% of optimum for the ranges of parameters investigated.

The results of combining the A-1 and A-2 battery design data on the basis of battery case temperature are shown in Figure 85. This curve illustrates the penalties incurred if the application requires reduced battery surface temperatures. As noted at the beginning of the discussion of the A-2 battery design, these data are for a self-contained heat sink employing LiH.

DESIGN B-1

Battery design B-1 meets the operational requirements of functioning in a gravity field and rejecting waste heat via radiation from the battery case. The gravity field was assumed to act along the battery centerline.

Cell Design

A simplification in cell design results from operating in a gravity field. The bellows compartment used in the A-1 battery design to store excess LiCl can be simplified by removing the bellows in the chamber. In a gravitational environment, the LiCl/Cl₂ cover gas interface can be predicted, and the cell plumbing arranged to prevent direct Li-Cl₂ chemical reactions within the cell. A sketch of the cell design is shown in Figure 86.

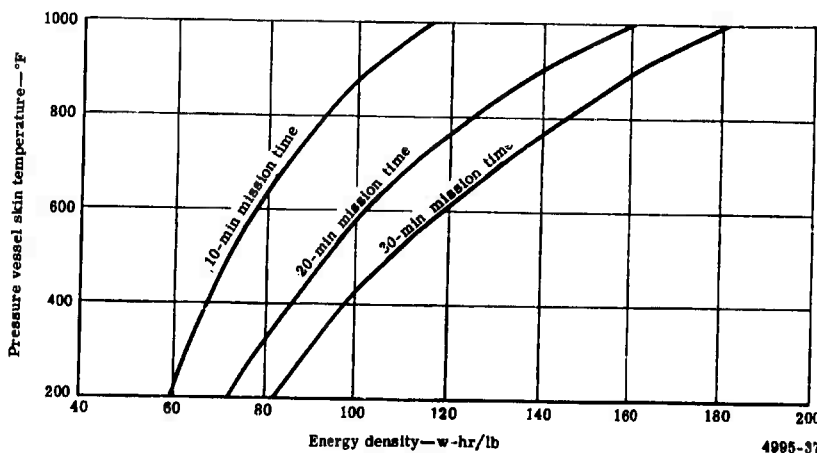
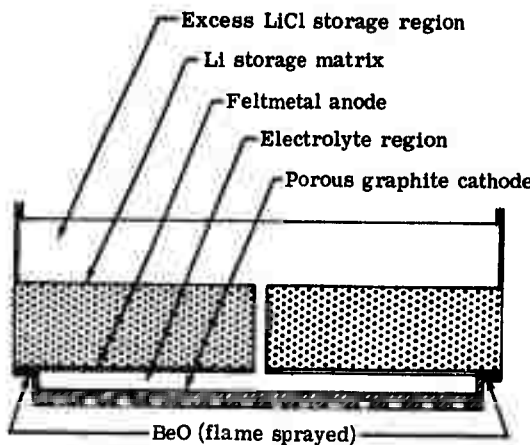


Figure 85. Effect of case temperature on energy density at 10-kw power level.



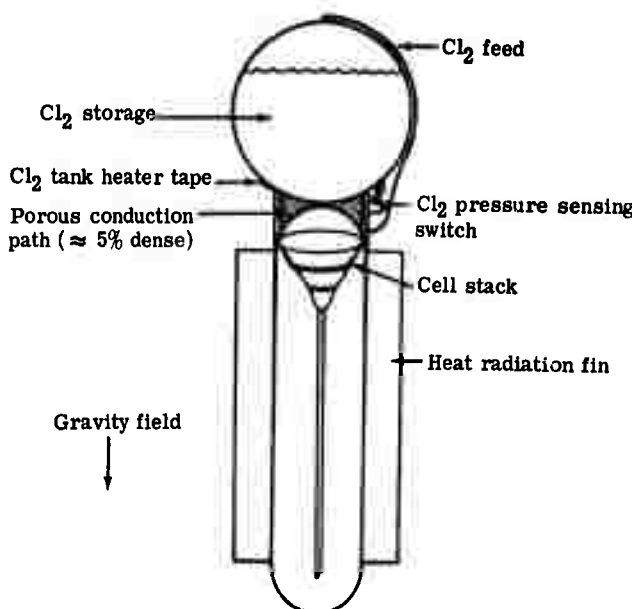
5125-15

Figure 86. Sketch of the B-1 cell cross section.

System Design

This system has the design objective of operating in a gravity environment with heat rejection via radiation from the battery case. The design closely resembles the A-1 battery design with the major exception of the Cl_2 storage subsystem. Operation in a gravity field permits the use of liquid storage and the resulting reduction in storage volume. In addition, storage and system operating pressures can be reduced with corresponding lower pressure vessel weights.

The Cl_2 storage system is also simplified by the use of liquid rather than gaseous storage which allows omitting the heat storage unit and conduction fins. In the B-1 battery design, heat to maintain the vapor pressure at system operating pressure (≈ 10 atm) is supplied to the Cl_2 vessel via conduction from the cell pressure vessel. This conduction path consists of Feltmetal® or a similar material which has a controlled density to provide the required thermal conductivity between the two surfaces. Chlorine pressure is sensed by a pressure switch which controls the power to an electrical heater blanketing a section of the Cl_2 tank. Approximately 80 to 90% of the required heat for Cl_2 vaporization will be transferred to the Cl_2 tank via conduction. The remaining heat requirements will be supplied via the electrical heater which acts as a topping control device. A sketch of the B-1 configuration is shown in Figure 87.



5125-16

Figure 87. Sketch of the B-1 battery design.

The base-line system weighed 16.46 lb with a volume of 369 in.³ which resulted in energy densities of 303 w-hr/lb and 13.5 w-hr/in.³. This increase over the corresponding A-1 battery reflects the weight and volume reductions possible through the use of liquid Cl₂ storage.

Parametric Scaling of the B-1 Design

The scaling of this system was completed over the same range of parameters as for the A-1 and A-2 battery designs:

- Power level—5, 10, and 30 kw_e
- Power density—10, 20, and 30 w/cm²
- Discharge times—10, 15, 20, and 30 min

Since the B-1 system can operate at lower pressures, the cell performance was reduced slightly to the values listed in Table VI. The cell open circuit voltage was also reduced from 3.64 to 3.56 v for operation at 10 atm.

Table VI.
B-1 battery design performance values.

<u>Power density (w/cm²)</u>	<u>Operating voltage (v)</u>	<u>Current density (amp/cm²)</u>	<u>Voltage efficiency (%)</u>	<u>Current efficiency (%)</u>
10	3.21	3.1	90.3	94.8
20	2.96	6.75	83.3	97.1
30	2.68	11.2	75.3	97.2

The basic method for calculating the B-1 system weights and volumes utilized the previously calculated zero g system (A-1 battery design) as a base line and to modify those system components affected by the change from zero g to a gravitational environment. Pressure vessel thicknesses were limited to a minimum gage of 0.020 in., since the reduced system pressures actually permitted material thicknesses which were questionable from a handling standpoint if designed to their stress limits. In general, the comments previously noted about system variations for the A-1 battery design are applicable to the B-1 battery design.

The results of this parametric scaling are shown in Figures 88 through 96. Weight and volume energy densities are defined as functions of discharge time and power density for a 10-kw_e system in Figures 88 through 91. Comparing these results with the A-1 battery system shows the improved energy density levels resulting with the B-1 design and the slight shift of optimum power densities for minimum weight systems to about 22 w/cm². The results of Figures 88 through 91 were combined in Figure 92 to illustrate both weight and volume characteristics for the 10-kw_e power level.

Similarly, the effects of power level are presented in Figures 93 through 95 on system weight and volume parameters. Battery power density versus battery energy is plotted in Figure 96. These results are preliminary and could vary as additional design parameters are considered. However, the design changes reviewed have resulted in variations of less than 10% for most design points.

DESIGN B-2

The last short duration battery analyzed was to operate in a gravity environment but reject its heat internally to maintain lower battery case temperatures. The design concept was based on previous work on the A-2 and B-1 systems, combining features from both designs.

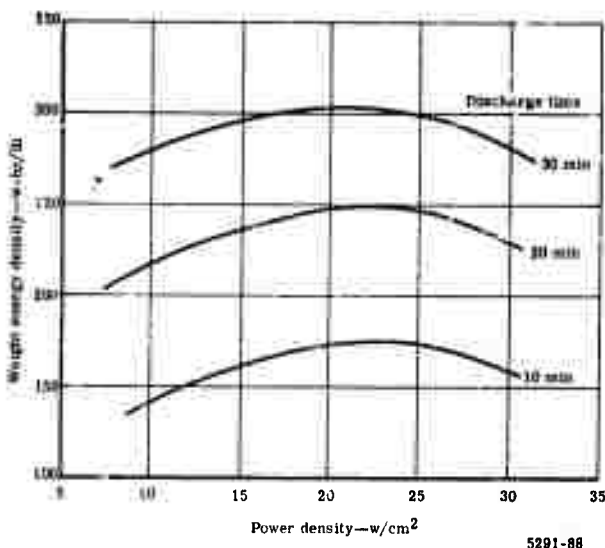


Figure 88. Weight energy density versus power density for the 10-kw_e B-1 battery design.

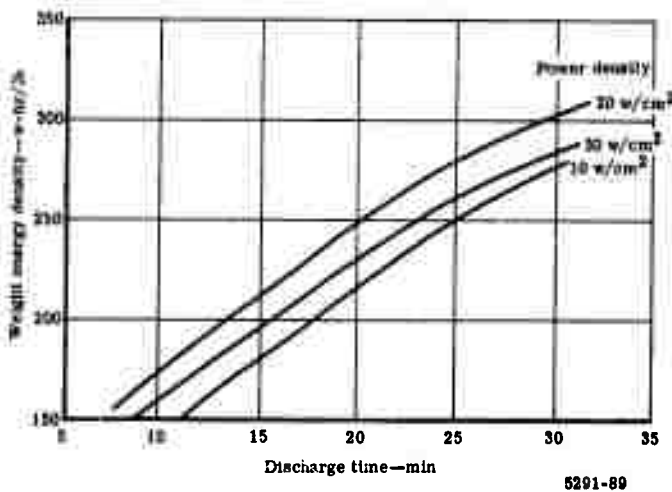


Figure 89. Weight energy density versus discharge time for the 10-kw_e B-1 battery design.

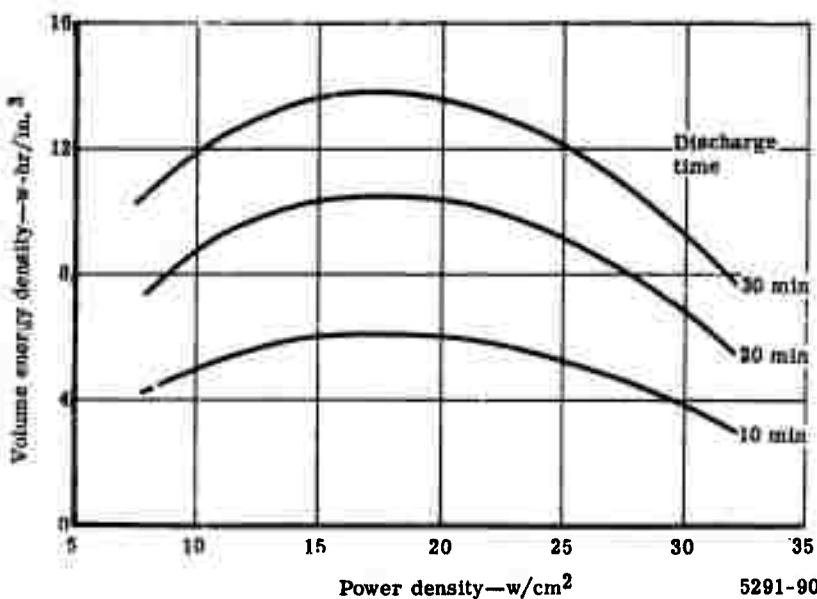


Figure 90. Volume energy density versus power density for the 10-kw_e B-1 battery design.

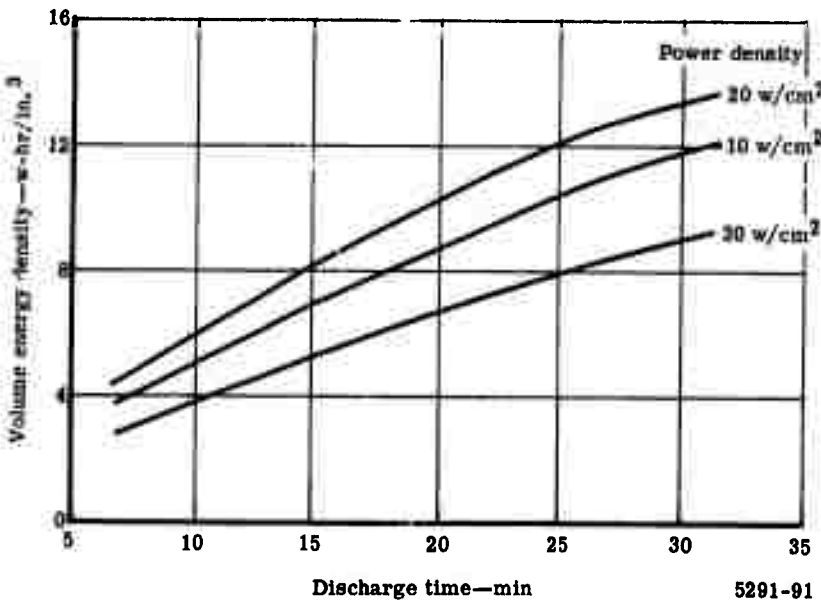


Figure 91. Volume energy density versus discharge time for the 10-kw_e B-1 battery design.

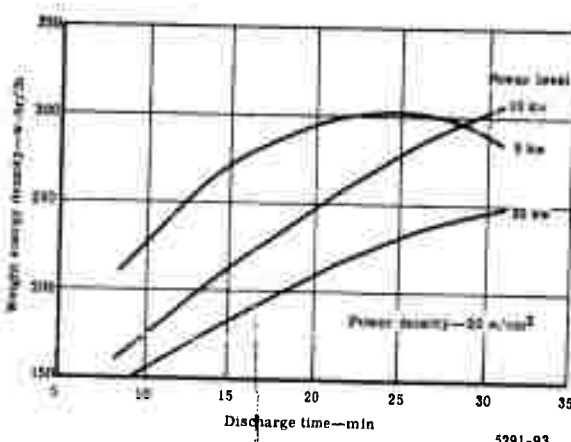


Figure 92. Volume energy density versus weight energy density for the 10-kw_e B-1 battery design.

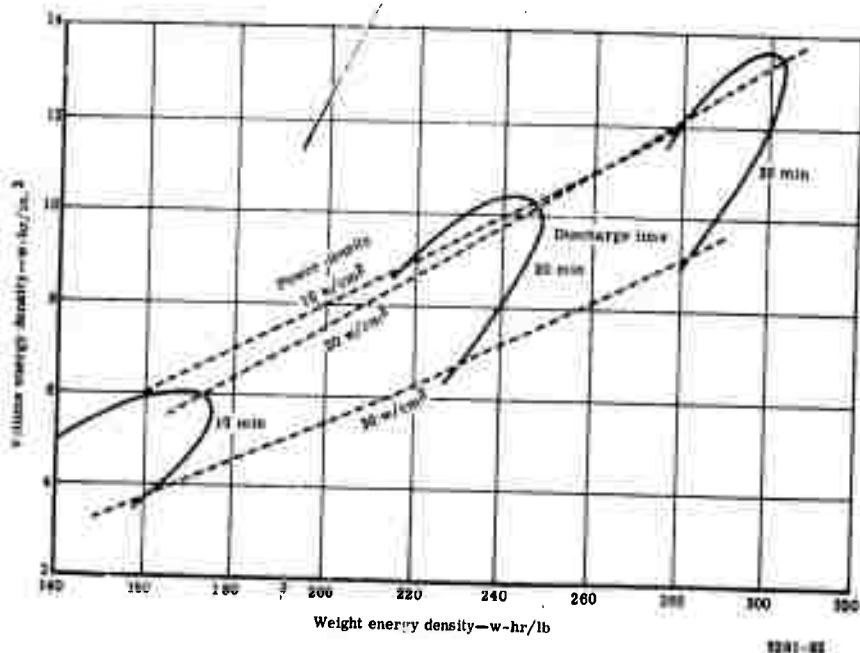


Figure 93. Effect of power level on the B-1 weight energy density.

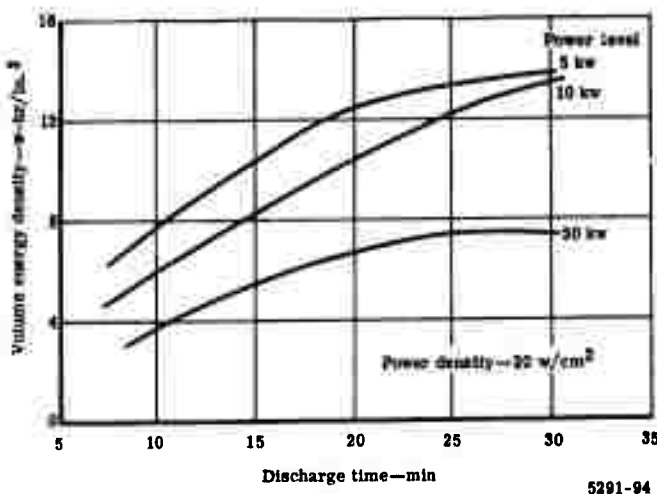


Figure 94. Effect of power level on the B-1 volume energy density.

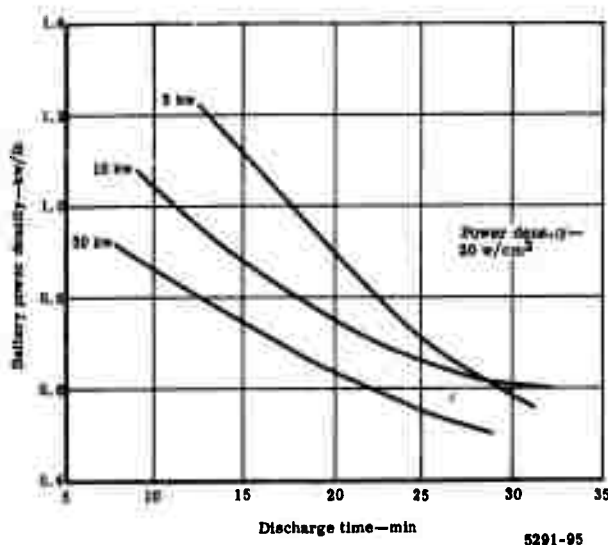


Figure 95. B-1 battery power density versus discharge time.

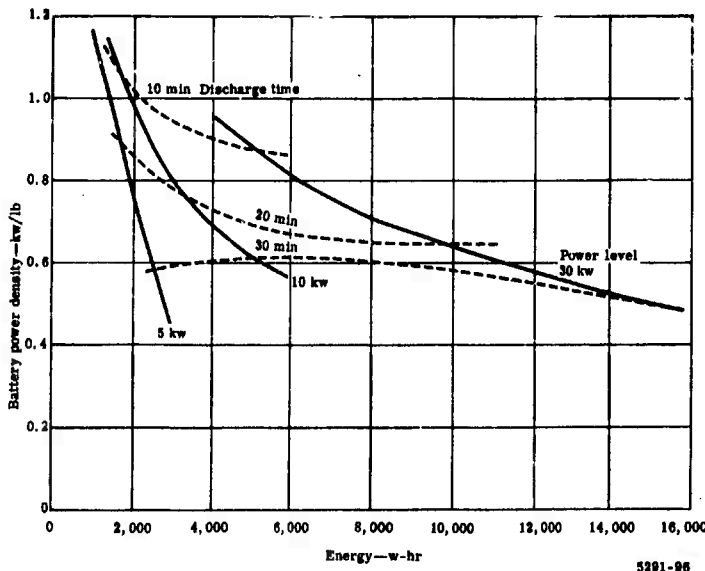


Figure 96. Battery power density versus energy storage for the B-1 battery design.

Cell Design

The cell design of the B-2 battery is identical to that of the A-2 design shown previously in Figure 73 with the exception that the flexible bellows isolating the LiCl storage region was removed. Operation in a gravity field permits prediction of the location of fluid levels within the cell, eliminating the need for the mechanical separator. The basic cell design and operation did not change with LiCl fed to the anode from the remote storage location and the waste heat stored in the LiH heat sinks on either side of the electrode.

System Design

In a similar manner to that for the B-1 battery system, the B-2 battery design is based on the zero g heat sink battery (A-2 design) described previously. Changing to a gravitational environment modifies the Cl₂ supply system previously noted and permits the use of lower system pressures.

In addition, the heat balance of the B-2 battery design is modified from that of the A-2 concept, since the Cl_2 is stored at a lower temperature and in the liquid state. The Cl_2 supply, therefore, acts as a more useful heat sink to the system and permits further reduction in the heat sink requirements of the battery to maintain a given surface temperature.

In the B-2 battery design, heat to the Cl_2 tank is supplied primarily via radiation rather than conduction which is used in the B-1 battery system. A topping system is again used to regulated Cl_2 pressure, utilizing an electrical heater mounted on the Cl_2 supply vessel which is actuated by a Cl_2 pressure sensing switch. A sketch of the B-2 battery concept is shown in Figure 97.

Parametric Scaling of the B-2 Design

The B-2 battery design was scaled over the same range of parameters as for the B-1 battery design. In addition, the battery case temperature as a parameter varied from 200 to 600°F. The reduction in the Cl_2 storage system coupled with the other changes have the predictable effect of improving both weight and volume power densities over those of the zero g design (A-2 battery design).

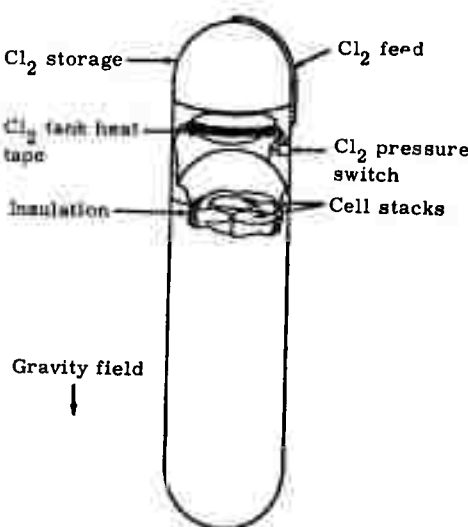


Figure 97. Sketch of the B-2 battery design.

The results of the parametric scaling are shown in Figures 98 through 108. Weight and volume energy densities as a function of power density, discharge time, and battery skin temperature are shown in Figures 98 through 103 with composite weight-volume plots shown in Figures 104 and 105. Weight minimums are strongly dependent on discharge time (Figure 98), while minimum volumes occur between 23 and 27 w/cm² over the range of parameters investigated.

The effects of battery power level on system parameters are shown in Figures 106 through 108. As battery power level is varied, optimum volume systems occur at low power levels, while weight optimums occur at higher power levels.

DESIGN C

In addition to the short discharge batteries described, longer discharge times were investigated to determine cell and system characteristics if operating times were up to 100 hr in duration. These extended discharge batteries were sized at 1 kw_e output using cell current densities of 10, 20, and 30 w/cm² and operating in a gravitational environment. Two discharge times were examined—10 hr and 100 hr. Battery voltage was approximately 30 v under load (10 cells).

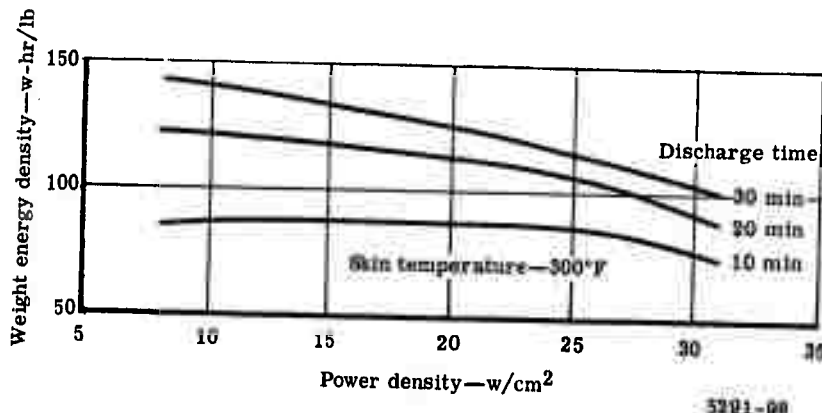
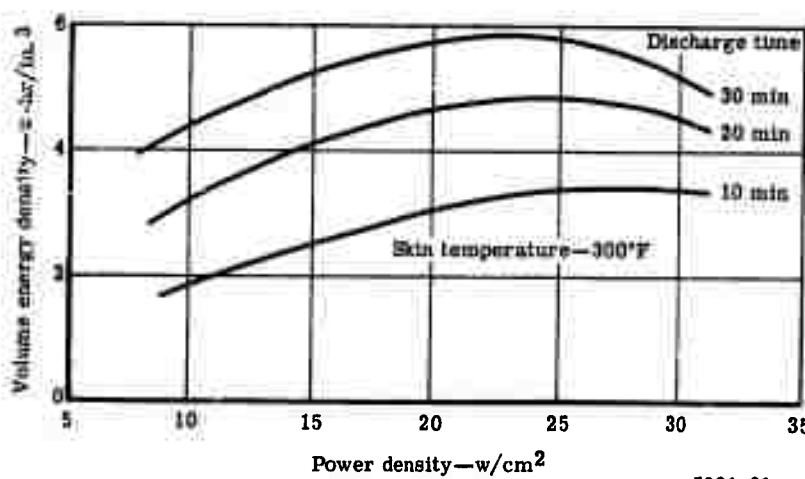
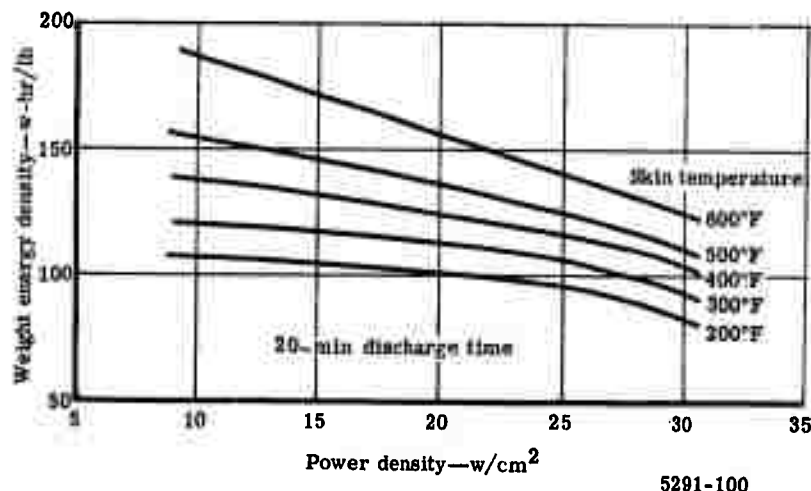


Figure 98. Weight energy density versus power density for the 10-kw_e B-1 battery design.



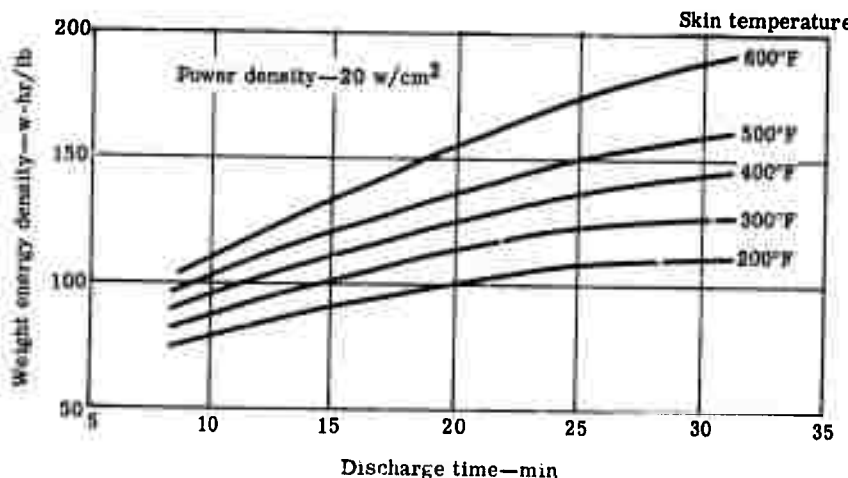
5291-99

Figure 99. Volume energy density versus power density for the 10-kw_e B-2 battery design.



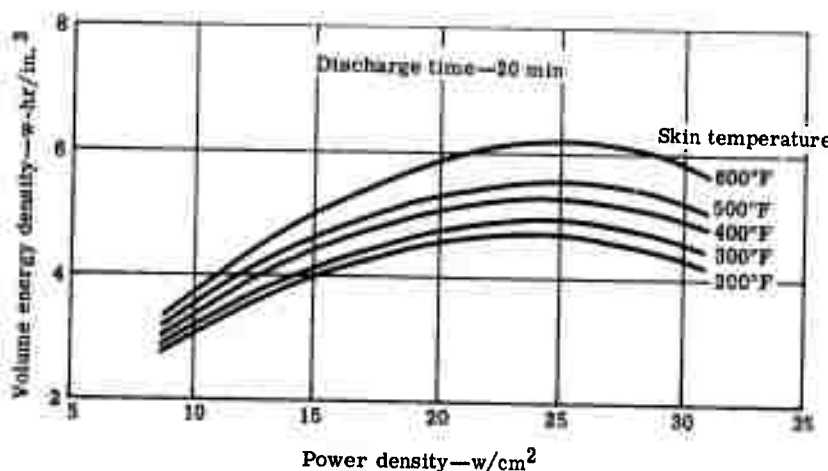
5291-100

Figure 100. Weight energy density versus power density for the 10-kw_e B-2 battery design (temperature effects).



5291-101

Figure 101. Weight energy density versus discharge time for the 10-kw_e B-2 battery design (temperature effects).



5291-102

Figure 102. Volume energy density versus power density for the 10-kw_e B-2 battery design (temperature effects).

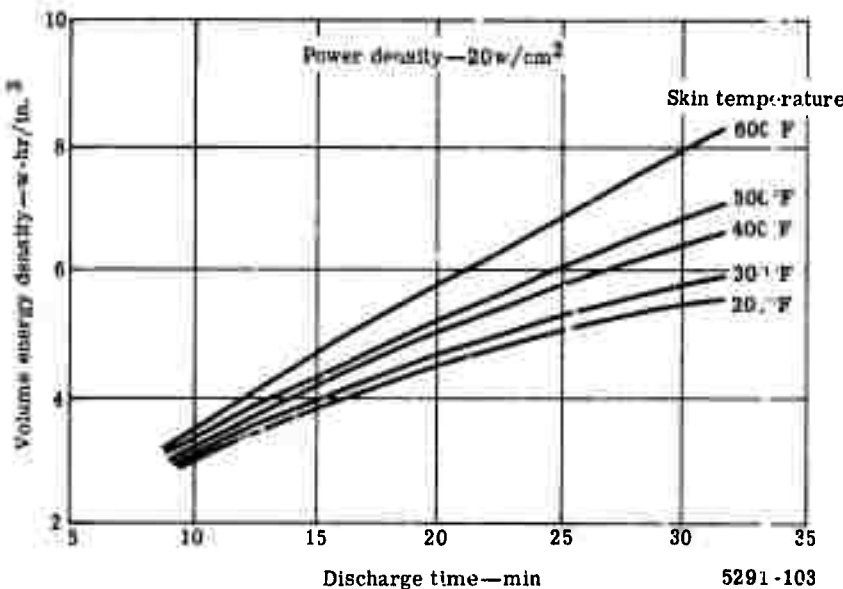


Figure 103. Volume energy density versus discharge time for the 10-kw_e B-2 battery design (temperature effects).

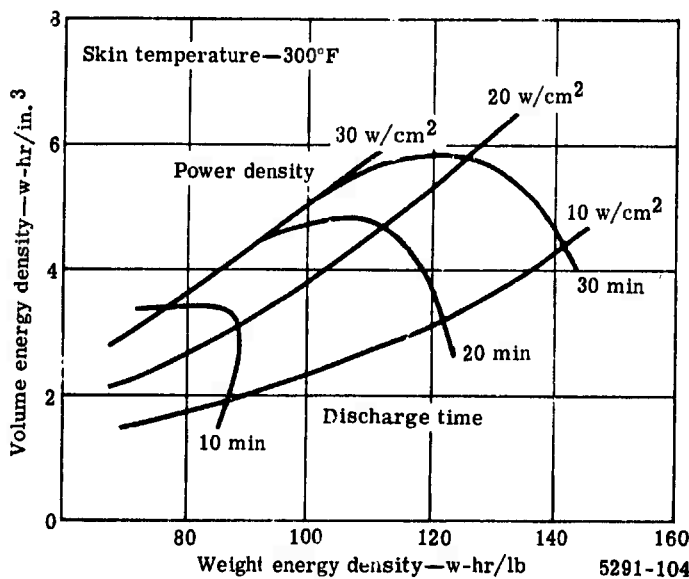
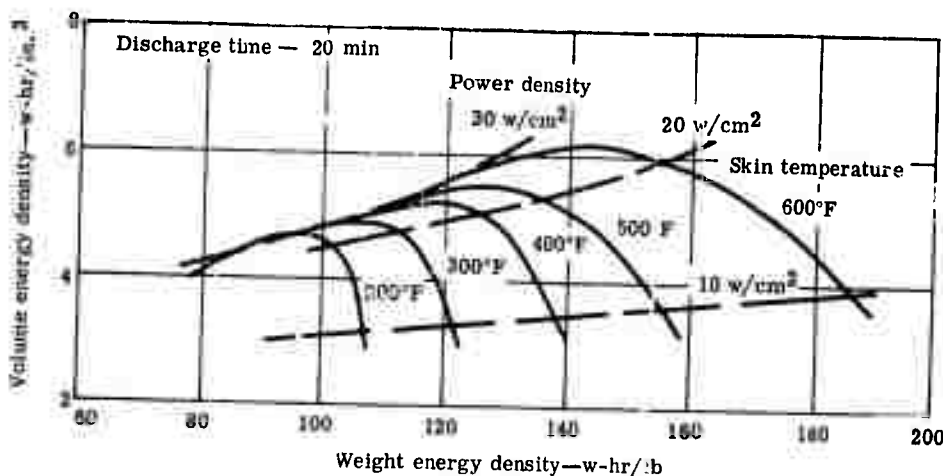
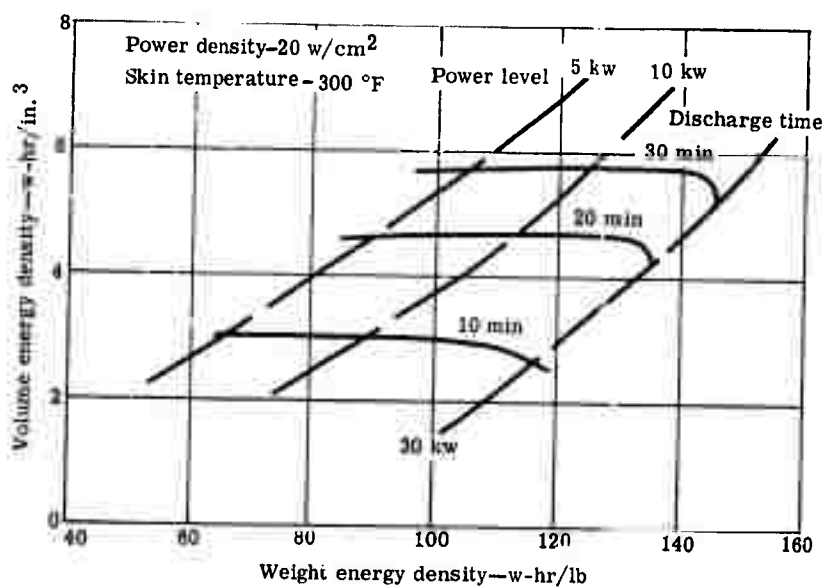


Figure 104. Volume energy density versus weight energy density for the 10-kw_e B-2 battery design.



5291-105

Figure 105. Volume energy density versus weight energy density for the 10-kw B-2 battery design.



5291-106

Figure 106. Power level effect on the B-2 energy densities.

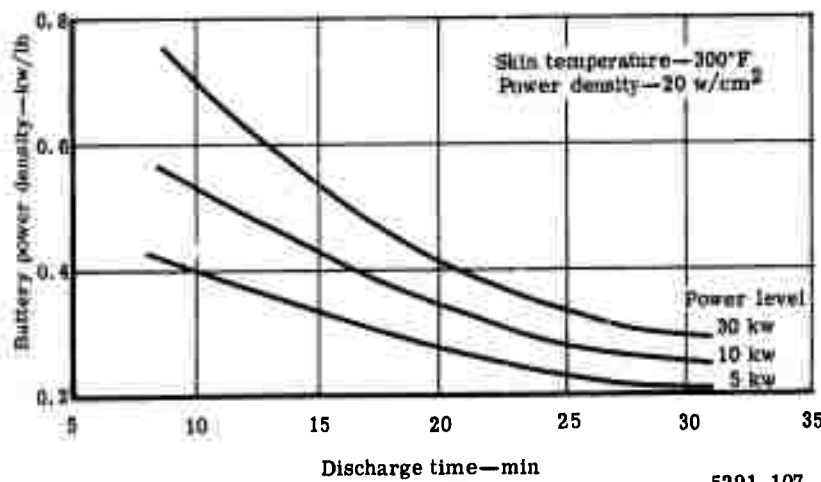


Figure 107. Battery power density for the B-1 battery design.

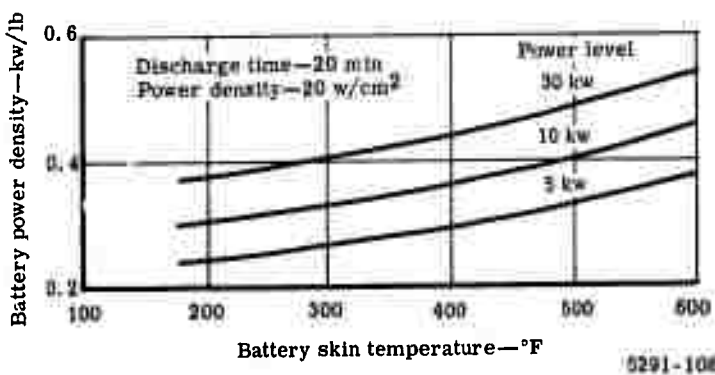


Figure 108. Battery power density versus skin temperature for the B-2 battery design.

Design of 10-hr Battery

The design concept for the 10-hr battery was an extension of that used for the preceding designs with matrix storage of lithium and the entire cell stack operating at cell operating temperature. However, two changes were incorporated because of the extended discharge time and lower power level.

Unlike the earlier design, this cell does not store all of the LiCl generated during discharge within the cell but stores it in a LiCl reservoir common to all cells. The second change was the use of a cylindrical cathode instead of the flat electrodes used previously. The feasibility of using cylindrical electrodes for such configurations was proven in the laboratory cells described in Section IV of this report. The cathode thickness and electrode spacing was the same as used previously, permitting the use of the same electrode performance values. A cutaway view of the cell configuration is shown in Figure 109.

During discharge, LiCl back fills the Li matrix and the excess is vented to the center of the cell where it drips to the LiCl storage compartment at the bottom of the battery shown in Figure 110. The same central tube also provides the Cl₂ feed to each cell.

Chlorine is stored as a liquid and the feed pressure is regulated by an electrical heater controlled by a pressure switch sensing the Cl₂ pressure level. System pressure was nominally set at 10 atm. The cell stack pressure vessel was insulated to control the heat loss from the surface with the outer battery temperature limited to 100°F.

The energy densities (weight and volume) for this concept are shown in Figure 111 for the cell power densities studied.

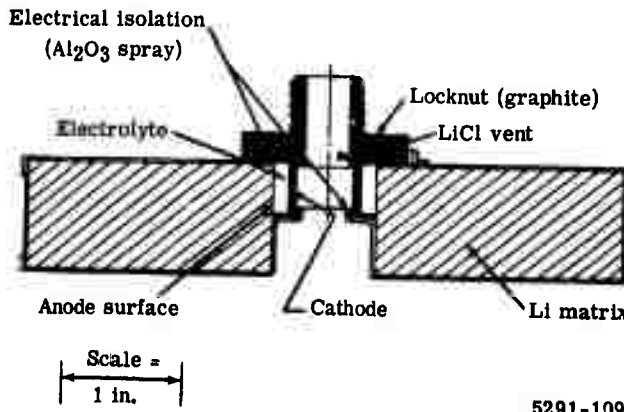


Figure 109. Section view of cell for 10-hr battery.

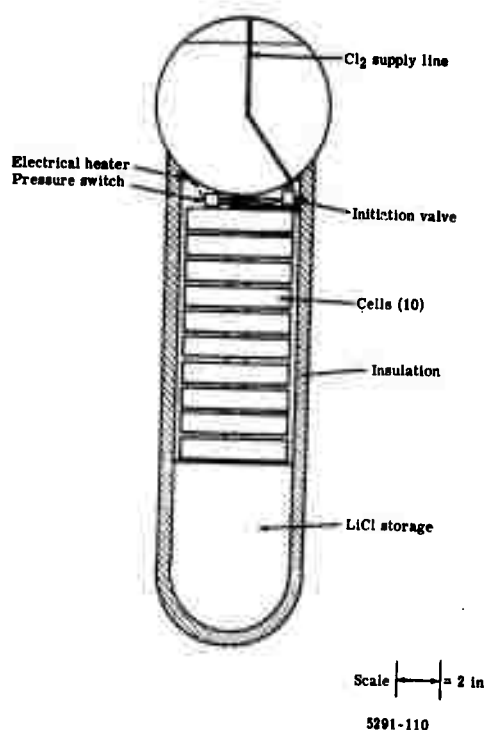


Figure 110. Section view of 10-hr Li-Cl₂ primary battery.

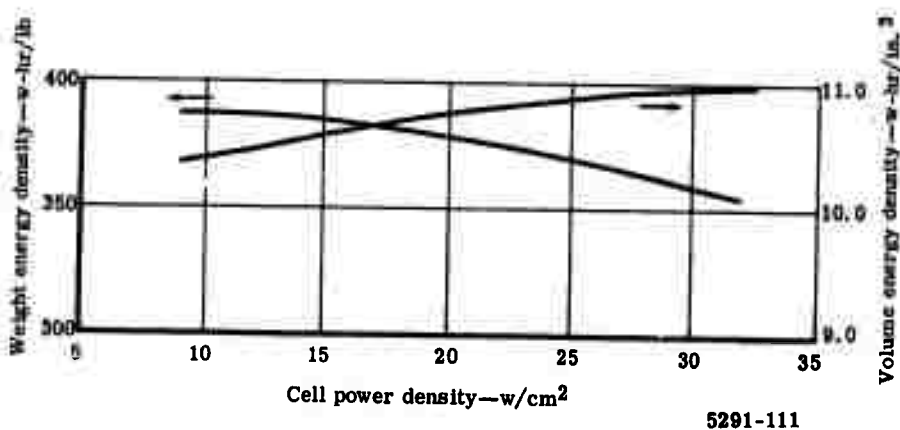


Figure 111. Energy density of 1-kw Li-Cl₂ 10-hr battery.

Design of 100-hr Battery

The second long duration battery is to generate 1 kw for 100 hr in a gravity environment (along battery centerline). The volume of this system has increased to the point where it no longer is feasible to maintain the entire battery volume at cell operating temperature due to the large heat rejection surface. Therefore, the battery is separated into regions of varying temperatures to minimize insulation requirements, while maintaining each component or subsystem at its necessary temperature. The cells are maintained at $\approx 1250^{\circ}\text{F}$, while the Li is in a 600 to 800°F temperature region and the LiCl is allowed to solidify in a reservoir isolated from the Li. This requires an inert cover gas to pressure balance the Li reservoir and eliminates the need of matrix storage of the Li.

The general battery arrangement is shown in Figure 112. The Cl_2 storage and feed system is similar to the other gravity systems (i.e., liquid storage operating at ≈ 10 atm with a pressure regulated electrical heater on the tank). The cells are located at the center of the battery in a region operating about 1250°F . Heat transfer from the cells maintains the adjacent Li storage reservoirs between 600 and 800°F . The battery is insulated to maintain a skin temperature of 100°F . Each cell is fed from individual Li storage tanks which are electrically isolated from each other with a ceramic spray coating. The Li storage tanks are pie shaped from a top view.

Each Li tank is pressure balanced from the Ar manifold slaved to the Cl_2 feed pressure. A battery operating for this duration will require a venting system to reduce the buildup of electroinactive impurities in the Cl_2 . Details of this venting system have not been defined; however, laboratory tests have indicated that the magnitude of Cl_2 required to be vented will be between 3 and 5% of the total Cl_2 consumed.

The details of the cell design for the 100-hr battery are shown in Figure 113. Graphite is used extensively in the design to withstand the high temperature Cl_2 environment. The external metal parts are ceramic coated and the metal gage increased to 0.020 in. Excess LiCl is vented to the center tube running along the centerline of the cell and flows into the LiCl storage chamber below the cell assembly. The characteristics of the 100-hr battery are illustrated in Figure 114.

Power source—Li-Cl₂
Maximum power—1000 w
Operating time—100 hr

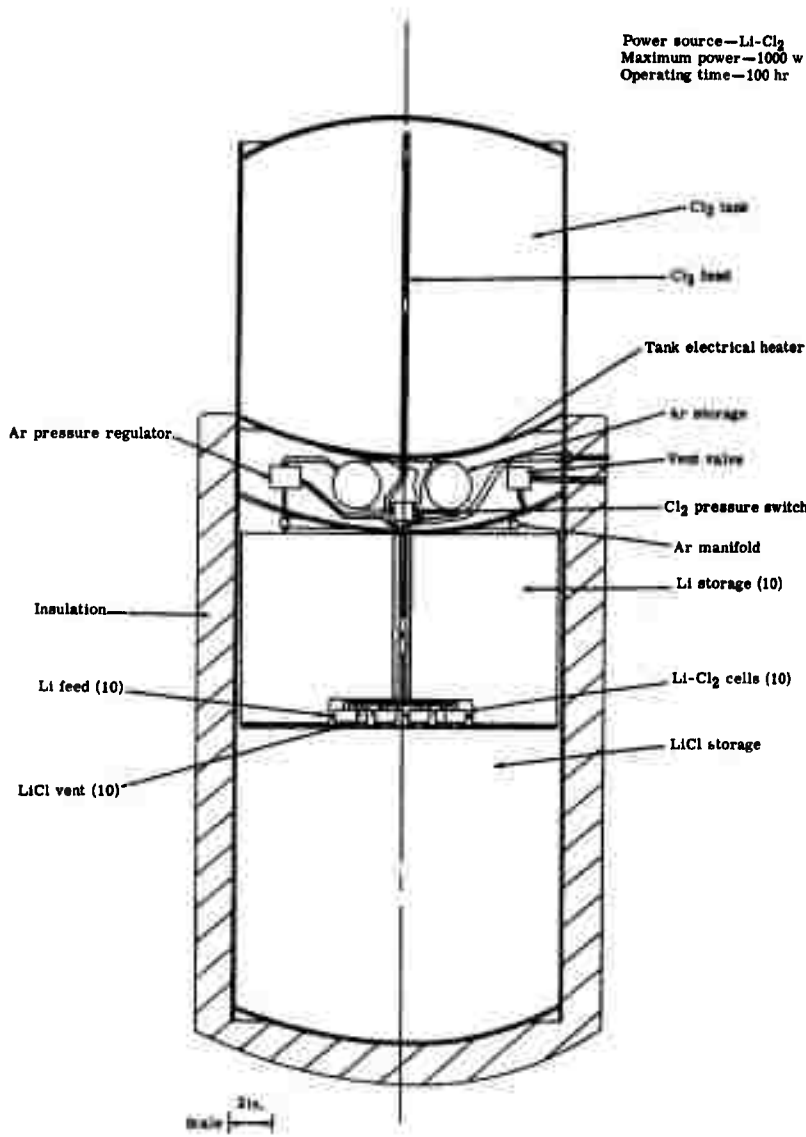


Figure 112. Sketch of the 100-hr Li-Cl₂ battery system.

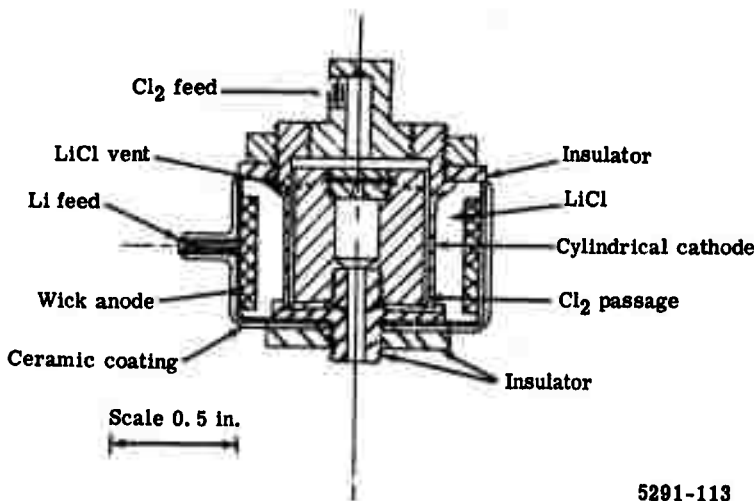


Figure 113. Cell details for the 100-hr battery design.

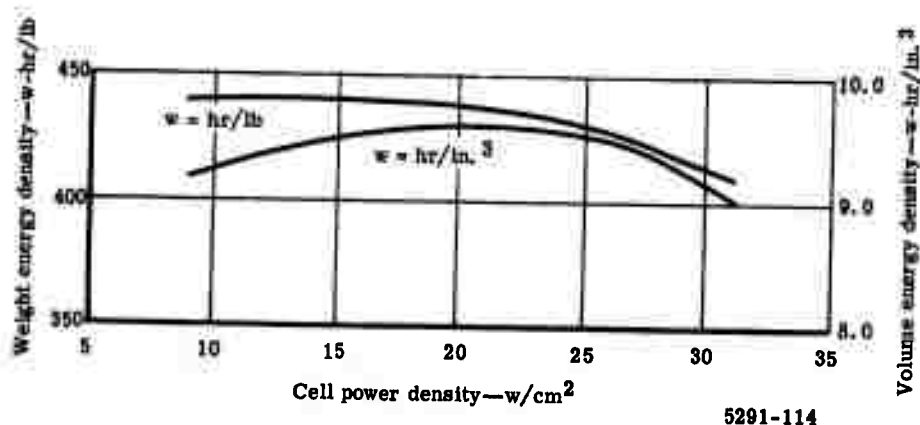


Figure 114. Energy density of 1-kw Li-Cl₂ 100-hr battery.

Unclassified

Security Classification

DOCUMENT CONTROL DATA : RA

(Security classification of title, body of abstract and indexing annotation must be entered when the overall report is classified)

DD FORM 1 JAN 64 1473

Unclassified

Security Classification

Unclassified

Security Classification

14. KEY WORDS	LINK A		LINK B		LINK C	
	ROLE	WT	ROLE	WT	ROLE	WT
Primary battery systems						
Lithium						
Chlorine						
Molten salts						
Chlorine electrodes						
Battery						

INSTRUCTIONS

1. ORIGINATING ACTIVITY: Enter the name and address of the contractor, subcontractor, grantees, Department of Defense activity or other organization (corporate author) issuing the report.

2a. REPORT SECURITY CLASSIFICATION: Enter the overall security classification of the report. Indicate whether "Restricted Data" is included. Marking is to be in accordance with appropriate security regulations.

2b. GROUP: Automatic downgrading is specified in DoD Directive 5200.10 and Armed Forces Industrial Manual. Enter the group number. Also, when applicable, show that optional markings have been used for Group 3 and Group 4 as authorized.

3. REPORT TITLE: Enter the complete report title in all capital letters. Titles in all cases should be unclassified. If a meaningful title cannot be selected without classification, show title classification in all capitals in parenthesis immediately following the title.

4. DESCRIPTIVE NOTES: If appropriate, enter the type of report, e.g., interim, progress, summary, annual, or final. Give the inclusive dates when a specific reporting period is covered.

5. AUTHOR(S): Enter the name(s) of author(s) as shown on or in the report. Enter last name, first name, middle initial. If military, show rank and branch of service. The name of the principal author is an absolute minimum requirement.

6. REPORT DATE: Enter the date of the report as day, month, year, or month, year. If more than one date appears on the report, use date of publication.

7a. TOTAL NUMBER OF PAGES: The total page count should follow normal pagination procedures, i.e., enter the number of pages containing information.

7b. NUMBER OF REFERENCES: Enter the total number of references cited in the report.

8a. CONTRACT OR GRANT NUMBER: If appropriate, enter the applicable number of the contract or grant under which the report was written.

8b, 8c, & 8d. PROJECT NUMBER: Enter the appropriate military department identification, such as project number, subproject number, system numbers, task number, etc.

9a. ORIGINATOR'S REPORT NUMBER(S): Enter the official report number by which the document will be identified and controlled by the originating activity. This number must be unique to this report.

9b. OTHER REPORT NUMBER(S): If the report has been assigned any other report numbers (either by the originator or by the sponsor), also enter this number(s).

10. AVAILABILITY/LIMITATION NOTICES: Enter any limitations on further dissemination of the report, other than those

imposed by security classification, using standard statements such as:

- (1) "Qualified requesters may obtain copies of this report from DDC."
- (2) "Foreign announcement and dissemination of this report by DDC is not authorized."
- (3) "U. S. Government agencies may obtain copies of this report directly from DDC. Other qualified DDC users shall request through _____."
- (4) "U. S. military agencies may obtain copies of this report directly from DDC. Other qualified users shall request through _____."
- (5) "All distribution of this report is controlled. Qualified DDC users shall request through _____."

If the report has been furnished to the Office of Technical Services, Department of Commerce, for sale to the public, indicate this fact and enter the price, if known.

11. SUPPLEMENTARY NOTES: Use for additional explanatory notes.

12. SPONSORING MILITARY ACTIVITY: Enter the name of the departmental project office or laboratory sponsoring (paying for) the research and development. Include address.

13. ABSTRACT: Enter an abstract giving a brief and factual summary of the document indicative of the report, even though it may also appear elsewhere in the body of the technical report. If additional space is required, a continuation sheet shall be attached.

It is highly desirable that the abstract of classified reports be unclassified. Each paragraph of the abstract shall end with an indication of the military security classification of the information in the paragraph, represented as (TS), (S), (C), or (U).

There is no limitation on the length of the abstract. However, the suggested length is from 150 to 225 words.

14. KEY WORDS: Key words are technically meaningful terms or short phrases that characterize a report and may be used as index entries for cataloging the report. Key words must be selected so that no security classification is required. Identifiers, such as equipment model designation, trade name, military project code name, geographic location, may be used as key words but will be followed by an indication of technical context. The assignment of links, rules, and weights is optional.

Unclassified

Security Classification